ALMA MATER STUDIORUM
UNIVERSITÀ DI BOLOGNA

DOTTORATO DI RICERCA IN

INGEGNERIA ELETTRONICA, TELECOMUNICAZIONI E TECNOLOGIE DELL'INFORMAZIONE

Ciclo 38

Settore Concorsuale: 09/F1 - CAMPI ELETTROMAGNETICI

Settore Scientifico Disciplinare: ING-INF/02 - CAMPI ELETTROMAGNETICI

DESIGN OF CONFORMAL, LOW-COST, MINIATURIZED, BATTERY-FREE SYSTEMS FOR NEAR- AND FAR-FIELD SENSING AND ACTUATION IN HEALTHCARE APPLICATIONS

Presentata da: Giulia Battistini

Coordinatore Dottorato

Davide Dardari

Supervisore

Diego Masotti

Co-supervisore

Alessandra Costanzo

Esame finale anno 2026

Contents

Abstract

The growing demand for wearable and implantable technologies is accelerating the development of miniaturized, lightweight, and energy-autonomous systems seamlessly integrated with the human body. This Thesis addresses the multidisciplinary challenges of realizing such platforms—combining electromagnetic (EM) design, materials science, and advanced fabrication techniques—to enable efficient wireless power and data transfer for next-generation biomedical and Internet of Things (IoT) applications. Specifically, this work introduces a unified framework for the design, fabrication, and experimental validation of conformal, flexible, and battery-free devices, emphasizing their mechanical compliance, biocompatibility, and electromagnetic performance. The research focuses on overcoming key limitations of existing wearable and implantable systems—namely power autonomy, wireless communication efficiency, and material constraints—through integrated near-field (NF) and far-field (FF) wireless power transfer (WPT), additive manufacturing (AM), and antenna co-design strategies.

In Chapter 1, a conformal, fully wireless, battery-free optogenetic platform based on inductive WPT at 13.56 MHz is developed and in-vivo validated for hypoglossal nerve stimulation to treat obstructive sleep apnea in small animal models, demonstrating reliable neuromodulation independently of the animal's position and orientation inside the experimental chamber, thus, preserving its natural behavior.

Chapter 2 explores the potential of AM and three-dimensional (3D) printing to engineer non-conventional, cost-effective, plastic 3D-printable materials to be used as dielectric substrates for low-cost, energy-autonomous wearable devices. As a proof of concept, a dual-port, cross-polarized 3D-printed rectenna is designed on the proposed 3D-printed engineered-PLA substrate and experimentally validated, achieving simultaneous energy harvesting and backscatter communication for indoor localization.

Building on these concepts, Chapter 3 introduces a hybrid NF/FF Simultaneous Wireless Information and Power Transfer architecture that integrates a 13.56 MHz resonant coil with a 2.4 GHz antenna. This dual-frequency system enables concurrent power and data transfer through a single RF link, reducing complexity and improving efficiency in wearable radiofrequency identification (RFID) and body area network applications.

Finally, Chapter 4 re-evaluates antenna topologies for wearable RFID systems implemented on flexible, lossy substrates such as textiles and 3D-printable polymers. Although microstrip patch antennas represent the conventional and widely adopted choice, the combined analytical and experimental analysis carried out in this chapter reveals its strong sensitivity to substrate height, permittivity, and conductivity. These findings call for a reconsideration of its suitability in such contexts and motivate the development of design guidelines and alternative topologies—such as shielded meandered dipoles—to improve robustness, radiation efficiency, and miniaturization.

Overall, this Thesis advances the state of the art in energy-autonomous wearable and implantable systems by bridging EM engineering, AM, and soft material technologies. The proposed methodologies and validated prototypes lay the foundation for reliable, low-cost, and body-integrated platforms capable of long-term autonomous operation, supporting future developments in personalized healthcare, wireless sensing, and distributed IoT ecosystems.

List of Abbreviations and Acronyms

EM	Electromagnetic
IoT	Internet of Things
NF	Near-Field
FF	Far-Field
WPT	Wireless Power Transfer
AM	Additive Manufacturing
3D	Three-Dimensional
SWIPT	Simultaneous Wireless Information and Power Transfer
RF	Radiofrequency
RFID	Radiofrequency Identification
UWB	Ultrawideband
NFC	Near-Field Communication
EH	Energy Harvesting
HF	High Frequency
UHF	Ultra-High Frequency
TX	Transmitting/Transmitter
RX	Receiving/Receiver
SAR	Specific Absorption Rate
PTE	Power Transfer Efficiency

PCE	Power Conversion Efficiency
PMU	Power Management Unit
MCU	Microcontroller Unit
LDO	Low Dropout
DC	Direct Current
OSA	Obstructive Sleep Apnea
μ-LED	Micro Light-Emitting Diode
PLA	Polylactic Acid
WBAN	Wireless Body Area Network
REM	Rapid Eye Movement
CPAP	Continuous Positive Airway Pressure
MPPT	Maximum Power Point Tracking
FDM	Fused Deposition Modeling
VNA	Vector Network Analyzer
GCPW	Grounded Coplanar Waveguide
Quasi-TEM	Quasi-Transverse Electromagnetic
IM	Intermodulation
AR	Axial Ratio
HB	Harmonic Balance
MN	Matching Network
PAPR	Peak Average Power Ratio
EIRP	Effective Isotropic Radiated Power
WIT	Wireless Information Transfer

S-parameter	Scattering Parameters
PEC	Perfect Electric Conductor
FoM	Figure of Merit

List of Symbols

$\mathbf{E}$	Electric field intensity
$\mathbf{H}$	Magnetic field intensity
η_0	Free-space impedance
λ	Wavelength
f	Operating frequency
ω	Angular frequency ($2\pi f$)
η_{rad}	Radiation Efficiency
G	Antenna Gain
S_{ij}	Scattering Parameters (Transmission Coefficient)
S_{ii}	Scattering Parameters (Reflection Coefficient)
Z_0	Characteristic Impedance
Z_{in}	Input Impedance
V	Voltage
I	Current
L	Inductance
C	Capacitance
R	Resistance

$\boldsymbol{Q}$	Quality Factor
$\boldsymbol{k}$	Coupling Coefficient
$\boldsymbol{P_{RF,TX}}$	Transmitted RF Power
$\boldsymbol{P_{DC}}$	Output DC power
$\boldsymbol{\eta_{RF\text{-}RF}}$	RF-to-RF Efficiency
$\boldsymbol{\eta_{RF\text{-}DC}}$	RF-to-DC Efficiency
$\boldsymbol{\varepsilon_r}$	Relative Dielectric Permittivity
$\boldsymbol{\varepsilon_0}$	Vacuum Permittivity
$\boldsymbol{\mu_0}$	Vacuum Permeability
$\boldsymbol{\varepsilon_c}$	Complex Dielectric Permittivity
$\boldsymbol{\sigma}$	Dielectric Conductivity
$\boldsymbol{tan(\delta)}$	Loss Tangent
$\boldsymbol{h}$	Substrate Thickness

Introduction

The rapid expansion of wearable technologies and the Internet of things (IoT) is driving an unprecedented demand for miniaturized, lightweight, and energy-efficient devices. As these technologies evolve, modern sensors are expected to move beyond basic performance requirements—such as sensitivity and real-time responsiveness—toward greater autonomy, reduced power consumption, and seamless integration with the human body [1].

This trend is particularly relevant in the healthcare sector, where the growing prevalence of chronic diseases and the aging global population are placing increasing pressure on medical infrastructures. The COVID-19 pandemic further highlighted these challenges, exposing limitations of conventional centralized care, particularly when continuous patient monitoring is required [2]. Such limitations are also evident in the long-term management of chronic conditions such as cardiovascular diseases, diabetes, neurodegenerative disorders, and post-surgical recovery, where conventional approaches often fail to provide continuous, real-time care. Smart wearable and implantable devices offer a solution, enabling continuous acquisition of physiological and behavioral data, early detection of health issues, and personalized interventions.

The development of next-generation wearable and implantable sensing systems is closely linked to advancements in several emerging technologies, including biocompatible materials, flexible electronics, optical and electrochemical sensing platforms, wireless power transfer (WPT) in both near-field (NF) and far-field (FF) regimes, energy harvesting (EH) strategies, and big data and cloud computing frameworks [3]. Within this multidisciplinary landscape, illustrated in Fig. I(a), microwave technologies play three key enabling roles—power autonomy, efficient communication, and advanced sensing—which are fundamental to achieve truly autonomous and multifunctional devices. Addressing power limitations through diversified energy sources, low-power communication strategies, and integrated radiofrequency (RF) sensing is therefore crucial for the reliable and long-term operation of these systems [4].

The research presented in this Thesis combines electromagnetic (EM) and circuit co-design with innovative material engineering and fabrication techniques to address these challenges. The resulting conformal, miniaturized, and battery-free wearable and implantable devices—experimentally realized and validated—demonstrate efficient wireless power and data transfer, with particular emphasis on fully autonomous operation for biomedical applications. Achieving this goal requires simultaneously addressing multiple, often conflicting requirements, as summarized in Fig. I(b), including: (i) maintaining high power transfer efficiency and data integrity under size, alignment, and environmental constraints; (ii) integrating flexible and biocompatible materials with high EM performance; (iii) optimizing device architectures to balance mechanical compliance, user comfort, safety and long-term reliability; and (iv) developing rapid and cost-effective fabrication strategies suitable for complex, heterogeneous structures.

Balancing these factors requires an integrated design strategy, spanning from material and process selection to the co-optimization of circuit, antenna, and power management architectures. In particular, wireless performance determines the efficiency of power and data transfer, autonomy depends on the effectiveness of EH and low-power operation, while reliability and safety are essential to ensure stable long-term operation and biocompatibility in contact with or within the human body. Furthermore, aspects such as comfort and aesthetic integration are crucial for user acceptance in wearable systems, whereas cost plays a key role in scalability and clinical translation. As illustrated in the diagram, the design process culminates in the development of high-performance and low-cost wearable systems, enabled through stochastic framework–based co-optimization and validation under realistic operating conditions.

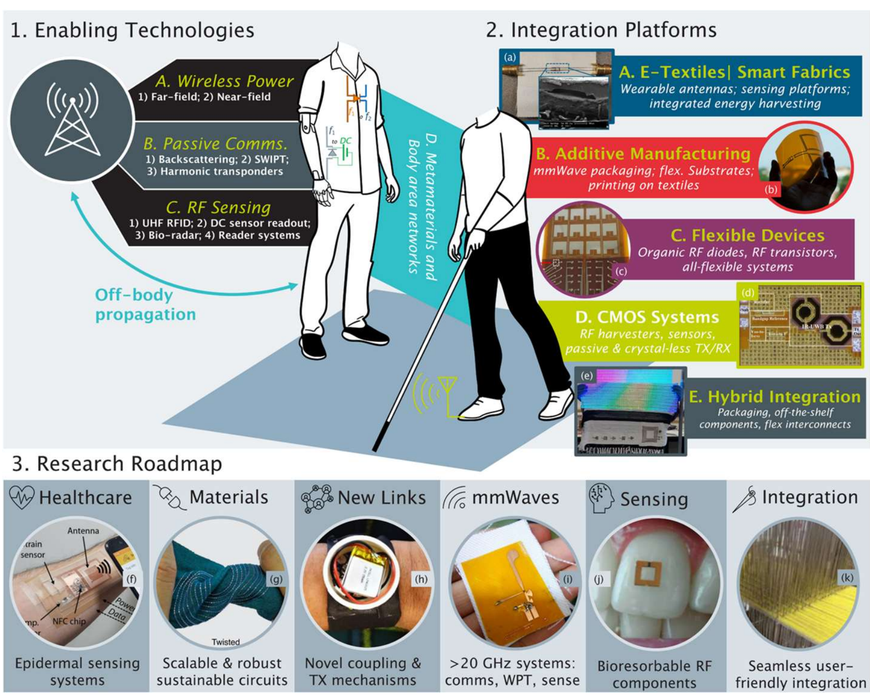

(a)

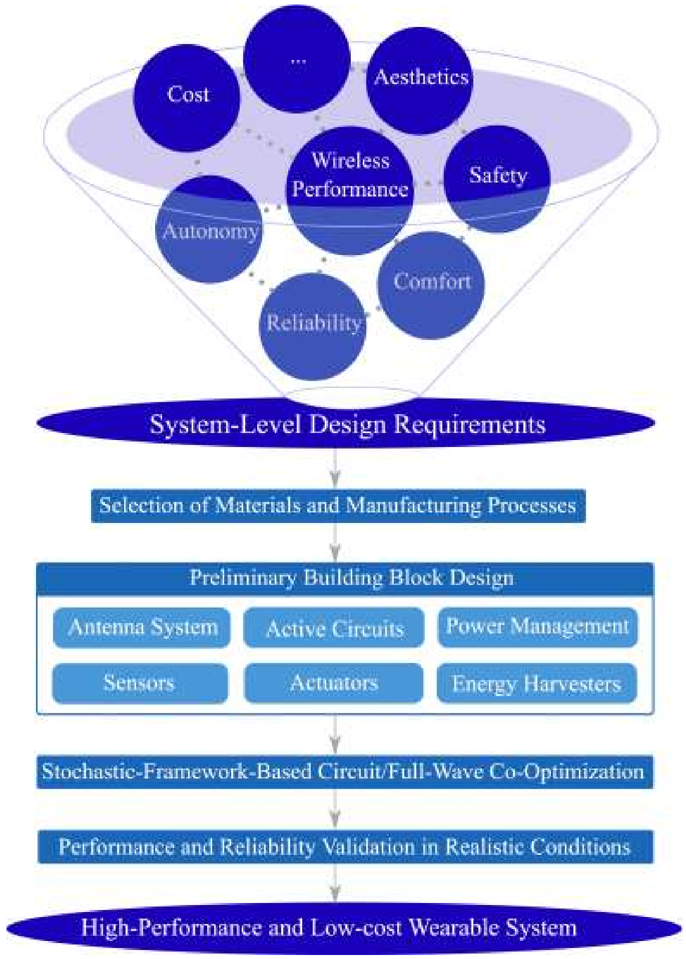

(b)

Figure I. (a) Representative examples of next-generation wearable systems integrating RF and microwave functionalities into wearable platforms: millimeter-wave (mmWave) textile-based transmission lines; inkjet-printed wearable rectenna for wireless EH; fully printed phased array for beamforming applications; wearable CMOS RF-powered ultra-wideband (UWB) system-on-chip; multifunctional textile platform integrating sensing and communication; NFC-enabled smart bandage for wireless monitoring; embroidered liquid-metal RF textiles; body-coupled communication electrodes for low-power data transmission; mmWave textile-based rectenna; RF-enabled tooth-mounted monitoring system; integration of flexible electronic circuits into woven textiles. (b) Schematic illustration of the transition from a complex set of design requirements to the development of reliable, high-performance, and cost-effective wearable platforms through a stochastic framework–based methodology. [4] ©2023 IEEE.

To sustain device functionality over extended periods without frequent maintenance or battery replacement, efficient power supply strategies are essential. In this regard, biomechanical, biochemical, thermal, and environmental energy sources naturally available from the human body and its surroundings represent valuable opportunities for EH. By converting these energy forms into usable electrical power, wearable and implantable systems can reduce or even eliminate their dependence on conventional batteries, enabling self-sustaining platforms that support continuous health monitoring while improving patient comfort and quality of life [5]. However, while harvesting energy from the body and its surroundings offers valuable opportunities for achieving self-sustainability, the inherently limited and intermittent nature of these sources often constrains the overall system performance. Therefore, the integration of external power delivery mechanisms becomes essential to guarantee stable, reliable and continuous device operation without requiring direct contact with the body—an essential feature for long-term monitoring and fully implantable systems. Typical power levels from these sources range from sub-milliwatt outputs for ultrasonic and photovoltaic systems to several milliwatts for near- and mid-field magnetic coupling, whereas biological energy harvesters—such as biofuel cells or triboelectric generators—typically provide only microwatt-level power, often insufficient to sustain continuous microcontroller operation.

Due to their higher and more stable power delivery, EM radiation and NF coupling have emerged as the most practical and scalable strategies for operating bio-integrated, battery-free sensors, wearable and implantable devices, and radiofrequency identification (RFID) systems. This is further supported by the widespread presence of ambient RF energy in urban environments, generated by dense networks of Wi-Fi and cellular transmitters [6].

Within this context, FF WPT enables long-range energy transmission at high frequencies (HF) (hundreds of MHz to several GHz), suitable for powering distributed wearable or implantable devices with compact receivers. However, its efficiency is strongly affected by the relative orientation between transmitting (TX) and receiving (RX) antennas and by environmental obstructions, which introduce significant free-space losses. High antenna gains are typically required to compensate for these effects, but this comes at the cost of a narrow angular acceptance. Moreover, FF transmission is constrained by safety regulations related to EM exposure, since high power levels can increase the specific absorption rate (SAR) and potentially induce tissue heating.

In contrast, NF WPT relies on non-radiative EM coupling—either inductive (magnetic) or capacitive (electric)—between resonant elements located within approximately one wavelength divided by 2π (theoretical limit of the reactive near-field region). Although power transfer efficiency (PTE) in the NF regime rapidly decreases with distance, misalignment, and miniaturization of the coils or electrodes, these systems offer notable advantages. Inductive resonant coupling at low frequencies (~100 kHz–200 MHz) is relatively insensitive to dielectric variations and line-of-sight constraints, enabling stable power delivery even in complex or obstructed environments. Additionally, reduced tissue absorption at low frequencies allows for deeper penetration with minimal biological impact, making NF WPT particularly well suited for implantable medical applications.

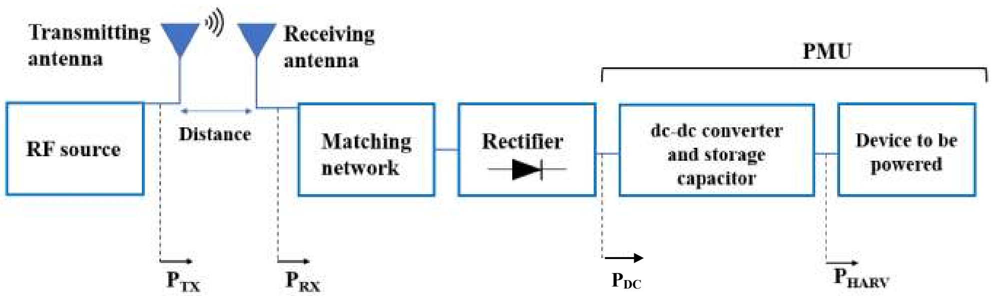

Figure II. Schematic block diagram describing an RF EH system. An RF source generates RF power, transmitted via the TX antenna and received by the RX antenna as RF power (P_{RX}). A matching network maximizes transfer to the rectifier, which converts the RF signal to DC power (P_{DC}). The DC power is processed by a DC-to-DC converter and stored in a capacitor within the power management unit (PMU). Finally, the harvested power (P_{HARV}) powers the device, illustrating the conversion of radiated RF energy into usable electrical energy for battery-free or autonomous devices. [7]. ©2014 IEEE

In both NF and FF WPT systems, the received EM energy is typically captured and converted into direct current (DC) power through a rectifying antenna, or rectenna. This component, as illustrated in Fig. II, integrates an antenna, responsible for harvesting the incident RF energy, with a rectifier circuit that converts the alternating signal into usable DC power [7]. In NF configurations, rectennas are often implemented as inductive resonant coils optimized for efficient magnetic coupling, whereas in FF systems they generally consist of compact antennas designed to operate efficiently at higher frequencies, where energy transfer occurs via propagating EM waves. Maximizing the transmission and reception efficiency is essential to ensure that the input power to the rectifier exceeds the diode threshold voltage, enabling effective RF-to-DC conversion. The rectification stage must be optimized to achieve the highest possible power conversion efficiency (PCE), taking into account the chosen circuit topology and the characteristics of the load.

While system-level and EM design strategies are essential, the physical realization of wearable and implantable systems critically depends on materials and fabrication technologies employed. While circuit and antenna co-design ensure efficient wireless operation, it is the mechanical and structural compliance of these systems that enables true bio-integration. Achieving intimate and stable contact with soft, dynamic biological tissues requires materials that combine biocompatibility, flexibility, and robustness, together with fabrication techniques capable of producing conformal and miniaturized architectures. Representative state-of-the-art examples of wearable and implantable, miniaturized, skin- and tissue-conformal RF battery-free electronics that embody these characteristics are shown in Figs. III. The figure includes: an NFC-enabled pulse oximeter device mounted on a thumbnail, which exemplifies a NF WPT and communication system for sensing blood oxygenation [8]; a tattoo-like epidermal antenna formed by serpentine conductive traces, representing a FF WPT platform for physiological measurements, and other wearable applications [9]; and a fully implantable, stretchable, and tissue-conformal soft optoelectronic system implementing FF WPT for optogenetic neurostimulation of the sciatic nerve and spinal cord [10].

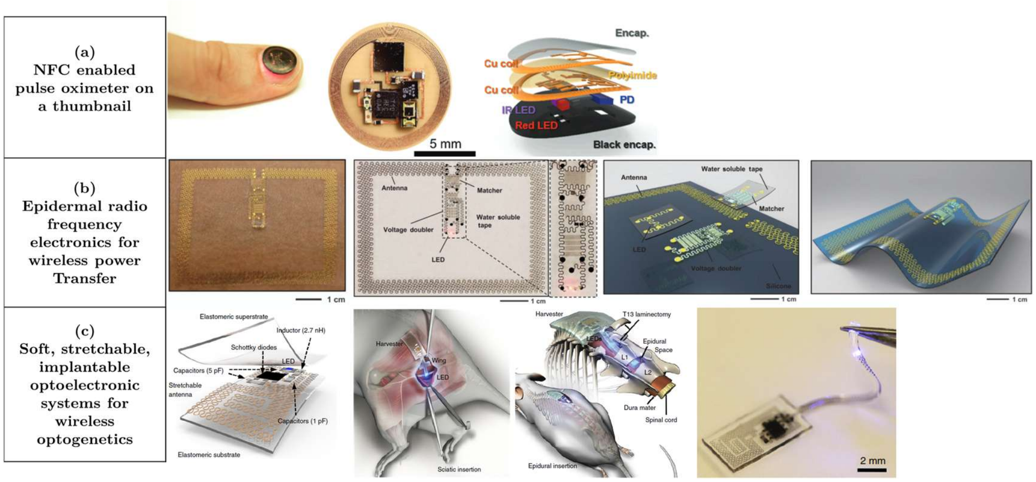

Figure III. Representative examples of wearable/implantable, miniaturized, skin- and tissue-conformal RF battery-free electronics for health monitoring, and optogenetics: (a) NFC enabled pulse oximeter device mounted on a thumbnail, [8]; (b) schematic illustration and implementation of a modularized epidermal RF system for wireless power transfer: epidermal skin-conformal loop antenna formed by serpentine conductive traces receiving RF power by a remote RF source for operating an integrated LED, [9]; (c) miniaturized, fully implantable, soft optoelectronic systems for wireless optogenetics: schematic exploded view of the energy harvester component of the system, with an integrated LED to illustrate operation, and the anatomy and location of the peripheral and epidural devices relative to the sciatic nerve and spinal cord. [10]. ©2015 Nature America

The variety of NF and FF WPT implementations illustrated above underscores how recent advances in flexible and conformal electronics pave the way for clinically relevant, body-integrated platforms.

Consequently, platforms such as wearable straps, patches, wristbands, and skin-conformal electronic tattoos [11] can offer enhanced patient comfort and reduced intrusiveness, while enabling continuous and long-term monitoring or therapeutic interventions. This, in turn, supports early diagnosis and timely treatment, ultimately improving clinical outcomes and contributing to the long-term reduction of healthcare costs [12].

Building on this concept, the same principles of conformal, flexible, and wireless operation can be extended to more advanced biomedical systems. Leveraging the outcomes of prior investigations published in [13], [14], [15], **Chapter 1** of this Thesis focuses on the design, development, and validation of a conformal, fully wireless, battery-free optogenetic system realized through an inductive WPT link at 13.56 MHz, aimed at preclinical studies in small mice models. The platform is specifically developed for applications in hypoglossal nerve stimulation as a potential treatment for obstructive sleep apnea (OSA), offering a minimally invasive alternative to conventional tethered systems. Unlike existing systems with rigid, skull-mounted receivers prone to misalignment and behavioral interference, the platform features a flexible, conformal inductive WPT system operating at 13.56 MHz. On the transmitting side, a series-connected multi-coil array provides an omnidirectional, uniform magnetic field, while maintaining effective power transfer within safe limits—significantly improving over conventional single-coil designs, which require higher transmitted power and are highly sensitive to misalignment. On the receiving side, a saddle-like implant on the back of the mouse maximizes the harvesting area, enhances tolerance to positional and angular misalignment, and eliminates cranial bulk. This configuration ensures reliable energy transfer and continuous micro light-emitting diode (μ-LED) operation, improving operational robustness, animal comfort, and experimental reproducibility. In-vivo validation, including full EM characterization and RF-to-RF/RF-to-DC efficiency measurements, demonstrates efficient, untethered wireless optogenetic stimulation even with low levels of radiant power.

While the Kapton-based system presented in Chapter 1 demonstrates notable flexibility and biocompatibility for implantable applications, advances in additive manufacturing (AM) and nanotechnology [16] open the door to soft materials whose mechanical properties more closely match those of biological tissues. These materials offer enhanced stretchability, ultra-thin profiles, and lightweight structures, enabling superior conformal contact with complex surfaces such as the brain, heart, and skin, while supporting high-quality signal acquisition, real-time feedback, and long-term in-vivo biocompatibility.

Any material with sufficiently small thickness inherently exhibits flexibility, as bending strain decreases linearly with reduced thickness. For example, while bulk silicon wafers are typically brittle and rigid, when silicon is structured into nanoscale ribbons, wires, or membranes, it becomes mechanically compliant [17]. Building on this principle, electronic metals and semiconductors can be engineered into micro- and nanostructured configurations—such as carbon-based nanomaterials, buckled nanoribbons, serpentine nanowires, or wavy mesh architectures—and seamlessly integrated with soft, elastomeric substrates and encapsulants like polydimethylsiloxane (PDMS), polyimide (PI), or parylene. This approach allows the resulting systems to bend, stretch, and compress while maintaining uniform stress distribution and minimizing localized strain.

To realize such mechanically compliant electronic systems, an equally important aspect concerns the patterning and fabrication of nanocomposite structures. A wide range of printing and lithographic techniques have been developed to achieve precise control over geometry, resolution, and material distribution. Among these, inkjet printing and extrusion-based three-dimensional (3D) printing stand out for their versatility, cost-effectiveness, and compatibility with a broad selection of functional inks and substrates. These AM methods enable rapid prototyping and scalable production of complex patterns having bespoke dielectric properties, without the need for masks or subtractive steps, thus easier, cheaper and faster than conventional micromachining techniques. In parallel, soft lithography techniques, such as mold casting, transfer printing, and stencil printing, provide excellent control over micro- and nanoscale features while maintaining compatibility with flexible and stretchable substrates. By leveraging these complementary fabrication strategies, it is possible to tailor the electrical, mechanical, and structural properties of flexible electronic systems to meet the demanding requirements of next-generation wearable and implantable devices [16].

Addressing the requirements of flexible and deformable communication systems, particularly for wearable, robotic, and biomedical applications, necessitates antenna designs capable of maintaining EM performance under mechanical stress, thereby enabling adaptability in dynamically changing environments. Stretchable antennas, such as those illustrated in Fig. IV, based on patterned conductive films on elastomeric substrates, have been widely explored using open-mesh or serpentine layouts [18], [19], [20], [21].

As an example, paper [18] defines key design principles for soft, stretchable electronics, showing how pattern geometry and substrate thickness can be optimized to balance stretchability, mechanical robustness, and antenna performance for seamless wearable integration.

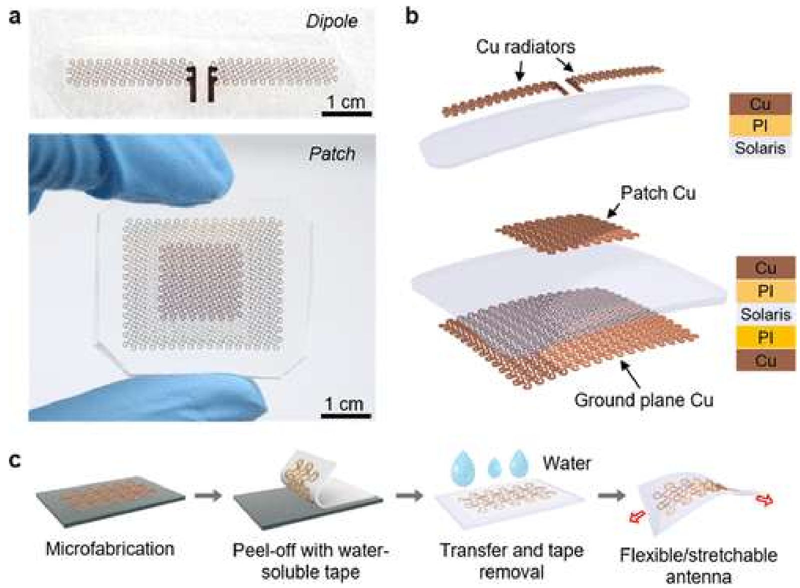

Figure IV. Fabrication process of stretchable antennas with a serpentine layout. (a) Photographs of a dipole antenna (top) and a patch antenna (bottom) realized on elastic materials. (b) Illustration of the multilayer structures for the two antenna types, with box diagrams on the right showing their cross sections. (c) Key fabrication steps: microfabrication, material transfer using water-soluble tape, and elastomer encapsulation. [18]. ©2020*ACS Appl. Mater. Interfaces*

However, despite the promising experimental results, converting rigid planar microwave systems into stretchable designs using serpentine mesh layouts still requires further investigation to identify the optimal balance between mechanical stretchability and microwave power dissipation, which can arise from impedance variations along the mesh due to changes in the curvature and geometry of the serpentine traces [22].

While significant progress has been achieved in developing stretchable and flexible electronic systems for wearable and implantable biomedical devices, their cost-effective and rapid realization still poses challenges. In this regard, AM and 3D printing provide a versatile route for customizing common bioplastic substrates for battery-free wearables, enabling fast, low-cost prototyping and fabrication, as well as the creation of complex geometries and heterogeneous flexible, soft materials tailored to specific biomedical needs [23]. Traditionally, low-cost, biocompatible, and biodegradable thermoplastics, such as nylon, acrylonitrile butadiene styrene (ABS), polylactic acid (PLA), polyethylene terephthalate (PET), and polyetherimide (PEI), have not been considered suitable as RF substrates due to their rigidity, high thickness, and poor EM properties (i.e., low dielectric permittivity (ε_r) stability and high loss tangent ($tan(\delta)$)), which limit their performance compared to specialized RF materials. However, by leveraging AM, their internal geometry and structural parameters can be precisely engineered to tailor effective dielectric properties, such as ε_r and $tan(\delta)$, to the target operating frequency and application, thus transforming these common thermoplastics into viable, low-cost alternatives for antennas and RF circuits in wearable and biomedical systems.

When developing 3D-printed dielectric materials for RF and antenna applications, a fundamental step is the accurate characterization of their EM properties. The dielectric characteristics of the 3D printed medium can vary significantly with the printing parameters—such as nozzle temperature and width, extrusion speed, sample thickness, and infill percentage—which directly influence both the frequency-dependent ε_r and $tan(\delta)$. For this reason, various EM characterization techniques are employed in the literature to extract the dielectric parameters of different printed samples across the frequency range relevant to the target application.

Building upon this understanding, the same controllable printing parameters can then be exploited to engineer materials with tailored EM performance. In recent years, numerous studies have demonstrated the advantages of 3D-engineered materials and architectures in antenna fabrication, offering a versatile and cost-effective alternative to conventional subtractive manufacturing techniques such as etching and machining. These innovations have led to lightweight, efficient, and low-cost 3D-printable devices suitable for energy-autonomous wearable health-monitoring systems. In this sense, the almost unlimited degrees of freedom offered by AM material synthesis allow for the creation of intricate internal structures of the RF substrates tailored for specific dielectric properties, namely, the variation of ε_r across two or even three axes, and the reduction of $tan(\delta)$ responsible for the intrinsic losses, affecting EM propagation and radiation. As an example, [24] demonstrates how 3D-printed substrate-integrated waveguides (SIWs) based on lossy PLA filaments can exploit AM to create non-uniform internal architectures—such as honeycomb lattices, illustrated in Fig. V—to locally control the dielectric constant and reduce loss tangent, thereby minimizing insertion loss and enhancing EM performance.

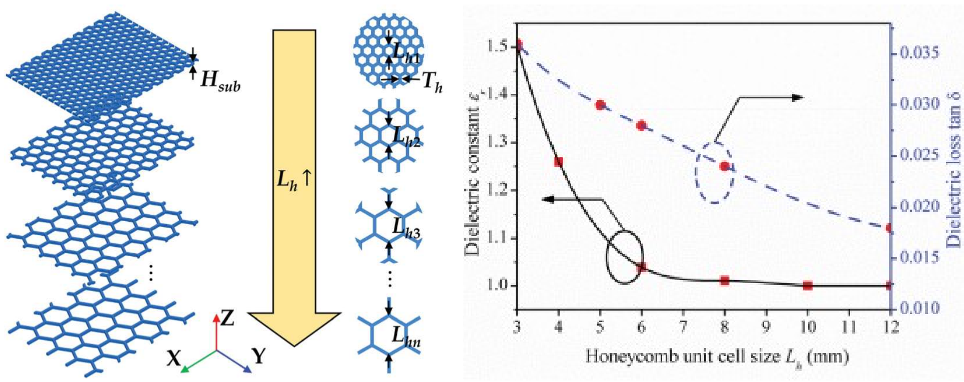

(a) (b)

Figure V. Schematic of the PLA honeycomb substrate with differently sized unit cells (L_h= unit cell size, T_h= unit cell thickness, H_{sub}= substrate height); (b) electrical properties of honeycomb substrate with respect to the length of the unit cell L_h. [24]. ©2020 IEEE

This level of material engineering, combining tailored internal structures and patterned infill, inspired by contemporary manufacturing practices and natural architectures—such as sandwich structures with honeycombs, trusses, and foam-like cores observed in living organisms—provide lightweight, robust, and mechanically resilient 3D-printed RF substrates having effective EM performance [25].

Expanding upon these concepts, based on previous studies published in [26], [27], [28], [29], [30], **Chapter 2** of this Thesis proposes innovative engineering and fabrication strategies to identify the optimal trade-off between low-cost, rapid manufacturability, high EM performance, and mechanical robustness suitable for localization and energy-autonomous wearable applications. Reference [26], which constitutes one of the main contributions of this Thesis, specifically focuses on the design, characterization, and implementation of a compact 3D-printed rectenna system fully fabricated on a low-cost engineered PLA substrate. The system integrates a dual-port, cross-polarized patch antenna with a ground plane providing electrical decoupling from the body, enabling simultaneous EH at ultra-high frequency (UHF) and passive backscattering of a quasi-ultrawideband (UWB) signal generated by the nonlinear rectifier operation. The 3D structure of the PLA substrate is carefully optimized to achieve antenna performance comparable to that of specialized RF materials, demonstrating the feasibility of low-cost 3D printing for wearable RF systems. Experimental characterization confirms that the quasi-UWB signal backscattered by the passive tag carries sufficient power for reliable reception and, when appropriately modulated, can transmit information from a passive accelerometer, powered by the DC EH through the rectification of the tag, for performing localization. This demonstrates the feasibility of a completely passive localization system integrating both EH and wireless information transfer (WIT).

The dual-port cross-polarized architecture introduced in the previous Chapter therefore already represents a first example of Simultaneous Wireless Information and Power Transfer (SWIPT), as it combines EH and passive data transmission within a single framework [31]. While WPT focuses on delivering energy efficiently over a wireless medium, and WIT maximizes data transmission capacity [32], SWIPT enables their concurrent operation through the same RF channel. This dual functionality reduces hardware complexity, minimizes device size, and enhances overall system integration. The paradigm is particularly appealing for wireless body area networks (WBANs) and IoT applications, where large-scale deployments of wirelessly connected devices are becoming increasingly common. In such scenarios, maintenance is a critical challenge due to the dense network layout, the often inaccessible placement of nodes, and the dynamic conditions in which these devices operate.

Another representative example of SWIPT implementation in wearable healthcare applications is presented in [33], where a 5.8 GHz wireless system for real-time breathing monitoring is developed. The fully wearable device provides sufficient energy to enable wireless data transmission of the measured vital signals through a low-power IoT node, effectively merging EH and communication functionalities within the same RF FF link.

Despite these advances, most existing SWIPT implementations rely on a single power transfer mechanism—either NF or FF—which can limit adaptability and efficiency in dynamic or heterogeneous environments [34]. To overcome this limitation, **Chapter 3** of this Thesis, based on the work published in papers [35], [36], introduces an innovative hybrid SWIPT architecture that integrates both NF and FF WPT mechanisms within a unified, compact, and wearable RFID-based platform. The design combines a 13.56 MHz resonant coil for efficient NF EH with a 2.4 GHz cross-polarized antenna for FF power transfer and data communication. Electromagnetic simulations and experimental measurements demonstrate the effectiveness of the system, making it suitable for low-power IoT devices, RFID, and wireless sensor networks by enabling simultaneous EH and WIT.

In most RFID implementations, such those abovementioned and presented in Chapter 2 and 3 of this Thesis, the microstrip patch antenna is the preferred RX antenna topology, mainly due to its higher radiation efficiency and inherent advantages in wearable contexts [4]. The presence of a ground plane ensures effective body decoupling, reducing detuning effects and limiting the SAR, while its planar and low-profile geometry enables straightforward integration onto flexible substrates. However, despite these advantages, the use of patch antennas on low-cost, high-loss dielectric substrates—such as common textiles or 3D-printable polymers—introduces significant performance limitations. As discussed in Chapter 2, the radiation characteristics of patch antennas are highly sensitive to substrate thickness and electromagnetic properties. Since common textiles and printable plastics are typically not optimized for RF applications and exhibit poor dielectric performance, severe degradation of antenna efficiency and radiation behavior may occur.

To address this issue, **Chapter 4**, based on the analysis and results published in [37], critically re-examines the suitability of microstrip patch antennas for wearable RFID tags on thin, low-cost, lossy dielectric substrates, such as those of common garments, within the context of EH for WBANs, to highlight their extreme sensitivity to substrate characteristics, compared to other antenna topologies. Through both EM simulations and equivalent circuit modelling, the analysis shows that antennas implemented on these substrates suffer not only from resistive losses, which reduce efficiency, but also from reactive perturbations of the input impedance. These effects are induced by the non-negligible dielectric conductivity (σ) of the substrate, causing part of the EM energy to remain confined within the material rather than being radiated. Interestingly, from this analysis, some patch antenna design guidelines are deducted, concluding that, contrary to conventional antenna design principles, among dielectrics with comparable conductivity, the detrimental effect of higher permittivity can be mitigated by slightly increasing the substrate thickness—thus achieving both satisfactory radiation efficiency and size reduction. Moreover, to overcome the inherent limitations of the patch antenna in this context, a shielded meandered dipole is introduced and experimentally validated as an alternative RX topology for wearable rectennas, providing excellent wearability, comparable radiation efficiency, robustness against substrate losses, and a reduced footprint. These findings offer clear strategies for the informed selection of dielectric materials and antenna topologies in wearable RFID applications constrained by flexible, lossy environments.

To summarize, this Thesis presents a unified framework for the design, fabrication, and experimental validation of miniaturized, flexible, and energy-autonomous wearable and implantable systems—particularly tailored for biomedical applications—introducing a series of innovations that collectively advance the state of the art in WPT and wireless communication technologies. Each Chapter addresses specific technological gaps identified in the literature, proposing original design strategies, fabrication techniques, materials, and architectures to enhance system efficiency, adaptability, and integration.

In detail, the main achievements are the following:

In **Chapter 1**, the proposed fully wireless, battery-free optogenetic platform for OSA treatment in small animal models ensures efficient, misalignment-tolerant energy transfer—independent of the animal's movements—overcoming the rigidity and positional sensitivity of conventional skull-mounted receivers present in the literature.

Chapter 2 extends this analysis to wearable applications by leveraging advances in AM for engineering 3D-printable polymer substrates. The resulting custom-designed PLA substrate enables the fabrication of the first 3D-printed dual-port wearable rectenna, which integrates EH and quasi-UWB signal backscattering for localization within a completely passive tag.

Building on this first demonstration of FF SWIPT, **Chapter 3** further advances the concept by introducing one of the few examples in the literature of a hybrid NF/FF SWIPT system for wearable applications. The proposed architecture enables simultaneous NF and FF EH together with FF data transmission, providing a more flexible and efficient framework for next-generation wearable devices.

Finally, based on the analysis of the previous chapters on 3D-printable and lossy textile materials for garments integration of wearable RFIDs, **Chapter 4** presents innovative design guidelines to mitigate losses, improve robustness, and maintain compact form factors in patch antenna design, while also proposing alternative configurations, such as shielded meandered dipoles, as miniaturized, robust and insensitive antenna topology.

Throughout this structured approach, the Thesis demonstrates how advanced EM design, flexible and conformal architectures, and energy-efficient strategies can be synergistically combined to develop reliable, high-performance, and low-cost wearable and implantable systems. Collectively, these results provide a foundation for next-generation, body-integrated devices capable of long-term autonomous operation, bridging materials science, additive manufacturing, and wireless communication technologies.

Chapter 1. Wireless Power Transfer-Enabled Optogenetic Stimulation of Hypoglossal Motoneurons Using a Miniaturized Battery-Free Implant for Functional Studies in Obstructive Sleep Apnea

This Chapter is based on the following articles:

[38] G. Paolini *et al.*, “Wireless power transfer-enabled optogenetic stimulation of hypoglossal motoneurons in mice for functional studies in obstructive sleep apnea,” in *IEEE Journal of Microwaves*, 2025.

[13] E. Augello, G. Battistini, G. Paolini, S. Bastianini, G. Zoccoli and A. Costanzo, "A Conformal Wireless Power System for Battery-Free Implantable Optogenetic Treatment of Obstructive Sleep Apnea," 2023 IEEE MTT-S International Microwave Biomedical Conference (IMBioC), Leuven, Belgium, 2023, pp. 166-168.

[14] G. Battistini, E. Augello, G. Paolini, S. Bastianini, G. Zoccoli and A. Costanzo, "Soft, Implantable, Battery-Free, and Wirelessly Controlled Optoelectronic System for Obstructive Sleep Apnea Treatment," 2024 IEEE MTT-S International Microwave Biomedical Conference (IMBioC), Montreal, Canada, June 2024.

[15] G. Battistini, E. Augello, G. Paolini, D. Masotti, and A. Costanzo, "Advancing Obstructive Sleep Apnea Therapy: a Miniaturized Wireless Implant for Battery-Free Optogenetic Neurostimulation in Mice," in *2025 IEEE Wireless Power Technology Conference and Expo (WPTCE)*, 2025, pp. 1–4.

This Chapter is developed within the framework of PRIN (Project of Relevant National Interest) 2022 NRRP project "ESTROSA: Energy-autonomous System for Treatment of Obstructive Sleep Apnea" (CUP: J53D23014050001), funded by the European Union (NextGenerationEU) under the Italian National Recovery and Resilience Plan (NRRP). This study was carried out also within the Spoke 13 of the MOST (Sustainable Mobility National Research Center) and received funding from the European Union under the NextGenerationEU programme (National Recovery and Resilience Plan (NRRP) – Mission 4 Component 2, Investment 1.4 – D.D. 1033 17/06/2022, CN00000023).

1.1 Introduction

This Chapter introduces a novel conformal, fully wireless, and battery-free optogenetic platform for preclinical studies in small animal models, specifically targeting hypoglossal nerve stimulation for the treatment of OSA. Unlike existing rigid, skull-mounted systems limited by alignment sensitivity and behavioral interference, the proposed platform leverages a 13.56 MHz inductive WPT link featuring a flexible, multi-coil transmitter that generates a uniform omnidirectional magnetic field within safe exposure limits. On the RX side, a miniaturized, saddle-shaped implant smartly positioned on the back of the mouse ensures enhanced comfort, and continuous μ-LED operation maintaining alignment tolerance regardless of movement or posture. This architecture marks a significant advancement in energy-efficient, untethered optogenetic neuromodulation, combining mechanical flexibility, robust coupling, and minimal invasiveness to improve both experimental reproducibility and animal welfare.

Obstructive sleep apnea is a prevalent chronic sleep-related breathing disorder characterized by recurrent episodes of partial or complete collapse of the upper airway during sleep (Fig. 1.1(a)), causing intermittent reductions or cessations of airflow [39], primarily due to an excessive reduction of lingual muscle tone, particularly during rapid eye movement (REM) sleep, which promotes upper airway obstruction [40]. The repeated obstructive events trigger a cascade of physiological consequences, including oxygen desaturation, frequent arousals, and disruption of normal sleep architecture. As a result, patients often experience excessive daytime sleepiness and a markedly reduced quality of life. In addition to these immediate effects, OSA is strongly associated with several serious related health conditions, such as cardiovascular diseases, hypertension, arrhythmias, stroke, metabolic dysfunction, and neurocognitive impairment [41].

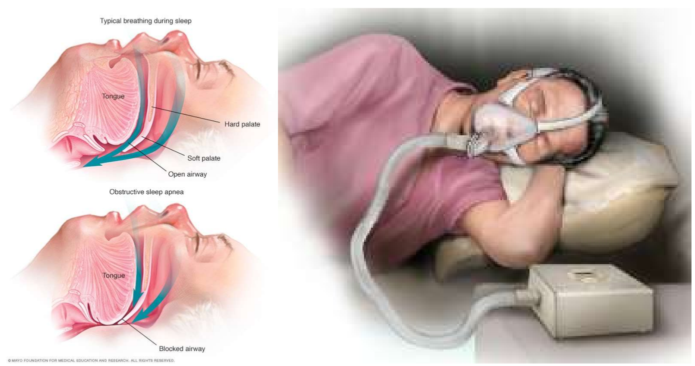

(a) (b)

Figure 1.1. (a) Schematic illustration of normal breathing during sleep (top) and upper airway obstruction in OSA (bottom), caused by the collapse of the soft tissues of the upper airway. [43]. (b) CPAP therapy, which maintains airway patency by delivering pressurized air through a nasal or oronasal mask during sleep. [44].

The current gold-standard treatment for OSA is continuous positive airway pressure (CPAP), which maintains airway patency through a constant flow of pressurized air delivered via nasal or oronasal masks (Fig. 1.1(b)). While CPAP is highly effective in preventing airway collapse, its long-term use is often limited by poor adherence. Compliance rates vary widely (40–85%) and are negatively impacted by factors such as discomfort, noise, air leakage, and the perceived invasiveness of the device in patients' nightly routines [42]. These limitations highlight the urgent need to develop alternative therapeutic strategies that are both effective and better tolerated.

An established alternative to CPAP is hypoglossal nerve stimulation, which improves airway patency by electrically activating the genioglossus muscle. This stimulation promotes tongue protrusion, thereby reducing the likelihood of airway obstruction during sleep [45]. Although clinically approved devices have demonstrated promising results, they typically require the surgical implantation of a pulse generator connected via leads to electrodes positioned around the hypoglossal nerve [46]. This configuration, while effective, is invasive and costly, and it carries risks of infection, nerve injury, and other device-related complications [47]. Moreover, currently approved implants are suitable only for selected patient populations and usually target unilateral or anterior tongue activation [48].

In recent years, optogenetic neurostimulation has emerged as a powerful tool to modulate neuronal activity with high spatial and temporal precision. This technique involves the expression of light-sensitive ion channels, such as channelrhodopsin-2 (ChR2) or halorhodopsin (NpHR), in specific neuronal populations. Targeted optical stimulation then allows precise activation or inhibition of these neurons, as illustrated in Fig. 1.2(a). Applying this approach to hypoglossal motoneurons represents a promising strategy to counteract upper airway collapse in OSA, offering functional selectivity with potentially lower invasiveness compared to conventional electrical stimulation [49].

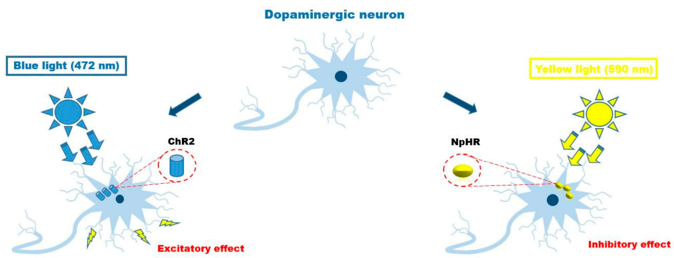

(a)

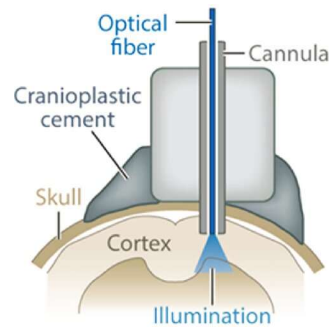

(b)

Figure 1.2. (a) Optogenetic neuromodulation: blue light excites neurons via ChR2, yellow light inhibits neurons via NpHR [50]. © 2020 *Appl. Sci.*; (b) An optical fiber implanted into the brain for light delivery [51]. © 2017 Journal of Medical Signals & Sensors

However, despite its potential therapeutic value, optogenetic stimulation for OSA remains at the preclinical stage and requires extensive validation in suitable animal models. Since the sequencing of its genome in 2002, the mouse has become the preferred species for biomedical research, including studies on sleep and breathing disorders [52]. Its small size (20–25 g body weight, skull dimensions ~2 × 1 cm) makes it particularly advantageous for controlled experimental studies but also imposes strict constraints on the miniaturization and intrusiveness of implanted devices. Therefore, for accurate and physiologically relevant experiments, wireless systems are especially valuable, as they overcome the drawbacks of tethered optical fibers—such as movement restriction, behavioral interference, and tissue damage—thereby enabling long-term, naturalistic investigations.
Conventional optogenetic platforms based on tethered fibers (Fig. 1.2(b)) or head-mounted LEDs [53] significantly limit animal mobility, can induce tissue

strain and inflammation, and are affected by optical losses in deeper brain regions. These drawbacks hinder chronic studies in freely moving animals, motivating the development of fully wireless and miniaturized implantable systems for precise optogenetic stimulation [54]. Early wireless optogenetic devices relied on head-mounted platforms with onboard batteries to eliminate tethers, but the added bulk and weight on the skull often altered natural behavior [54], [55].

Recent advances have thus focused on battery-free, fully implantable systems powered through WPT. These systems typically operate in the HF band (3–30 MHz) using inductive coupling, a technique widely adopted in consumer electronics for contactless energy transfer. Energy is transmitted from a coil integrated into the experimental cage and received by a subdermal coil implanted in the animal. The harvested RF energy is then rectified to DC and used to drive microscale light-emitting diodes (μ-LEDs) positioned at the target site. Despite these advancements, existing battery-free wireless optogenetic platforms [56], [57], [58], [59] still face several limitations, including sensitivity to positional and angular misalignment, mechanical strain from skull-mounted receivers, and potential interference with natural behaviors.

To address these challenges, this Chapter presents the design and testing of a flexible, conformal WPT system operating at 13.56 MHz, specifically developed for battery-free optogenetic stimulation of hypoglossal motoneurons in small-size laboratory mice (20–25 g body weight, body dimensions ~8–10 cm, skull dimensions ~2 × 1 cm). The system aims to prevent upper airway collapse by modulating the lingual muscle tone in-vivo.

It consists of a transmitting multi-coil array that ensures uniform omnidirectional power coverage within the experimental cage, and a pair of compact receiving coils implanted dorsally in a saddle-like configuration, as shown in Fig. 1.3(a). This strategic placement significantly improves tolerance to positional and angular misalignment compared to conventional skull-mounted receivers [56], [57], [58], [59], which are limited by small surface area and higher mobility. By relocating the receiver to the back, the design maximizes EH, reduces mechanical load on the skull, and preserves the animal's natural movements. The implant integrates a rectification circuit powering a μ-LED positioned subdermally over the hypoglossal nuclei, ensuring consistent light emission regardless of animal orientation. Most importantly, the use of wireless power transfer eliminates the need for fiber-optic tethers or wired connections, enabling unobstructed, naturalistic behavior during long-term in-vivo experiments.

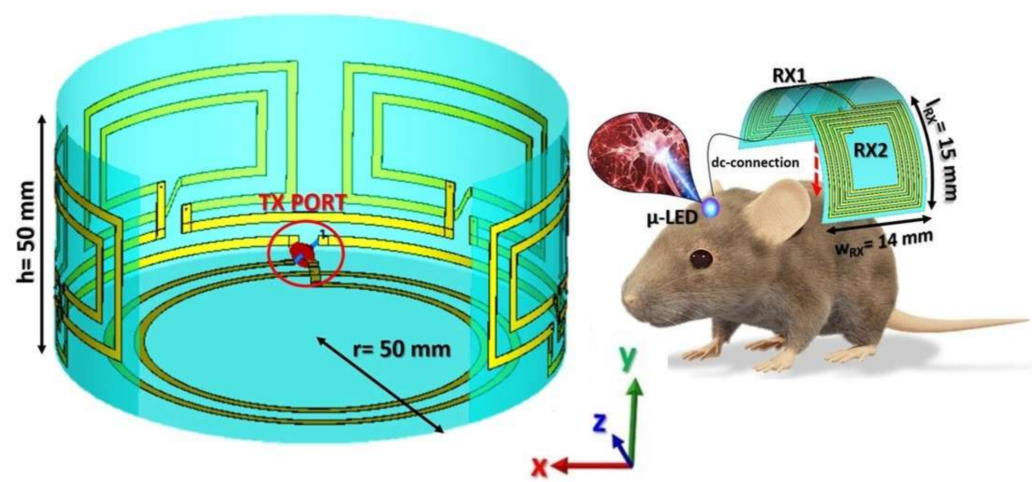

(a)

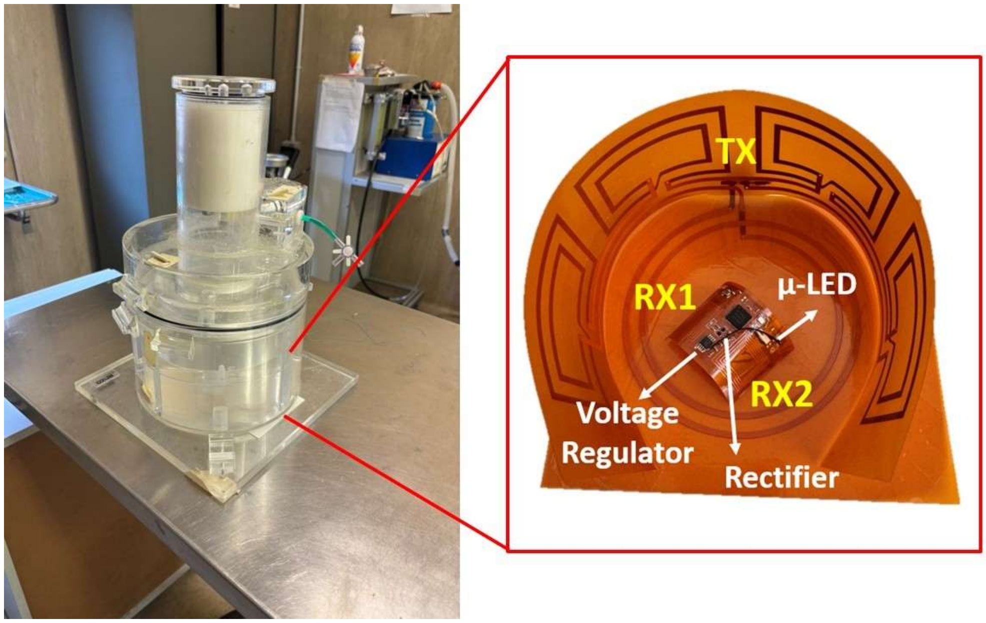

(b)

Figure 1.3. (a) Wireless power transfer system schematic overview: transmitting multi-coil array (left) and saddle-like receiving device implantable on the mouse's back (right), and (b) photo of the plethysmograph setup with a callout highlighting the fabricated prototype and a detailed view of the receiving system, including two receiving coils, rectifier, voltage regulator, and LED. [15]. © 2025 IEEE

The work presented in this Chapter is part of the broader 2022 NRRP project "ESTROSA" aimed at developing a closed-loop system for the preclinical treatment of OSA on laboratory mice. Within this framework, my contribution was focused on the design and optimization of the implantable receiving device of the WPT inductive link.

As illustrated in Fig. 1.4, the overall envisioned closed-loop system integrates the WPT system described, which is responsible for wirelessly energizing and controlling not only a μ-LED for optogenetic neurostimulation, but also a pulse oximeter that continuously monitors blood oxygen saturation. When this parameter drops below 90% (Normal oxygen saturation sleeping or awake: 96-97%, a drop below 90% is mildly abnormal, 80% to 89% is considered moderately abnormal, a drop below 80% is considered severely abnormal [60]), an OSA event is detected and a trigger signal activates the µ-LED to deliver targeted optogenetic stimulation. This stimulation consists of pulsed light signals directed to the hypoglossal nuclei, eliciting tongue contraction to reopen the upper airway and thereby reduces the number of apnea events during sleep. All experiments are conducted in preclinical studies using small laboratory mice.

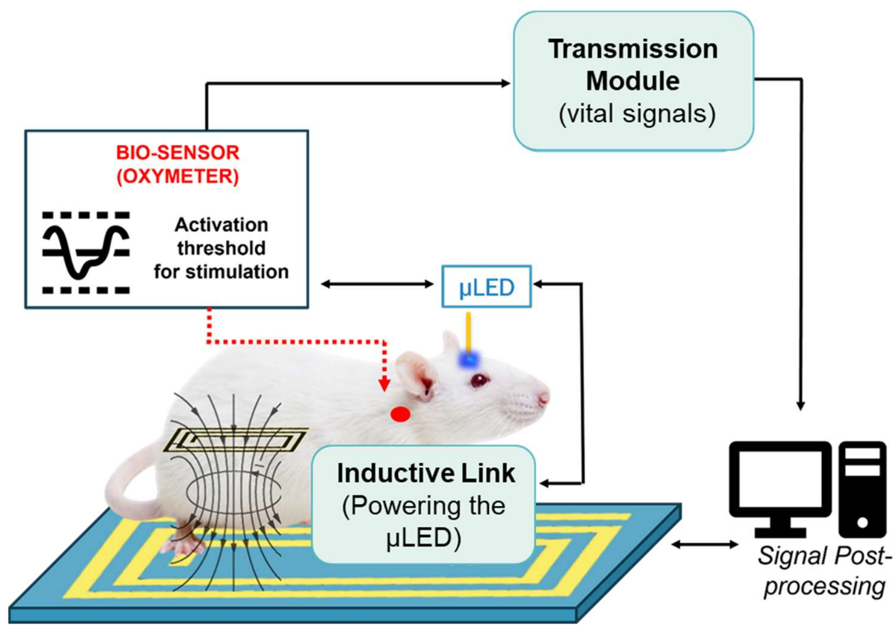

Figure 1.4. Conceptual diagram of the experimental closed loop system for wireless optogenetic stimulation and in-vivo physiological monitoring. The implanted receiver is wirelessly powered through inductive coupling at 13.56 MHz, enabling the activation of a µ-LED positioned near the hypoglossal nuclei. A biosensor (oximeter) records vital parameters and transmits the data to a relay module, which forwards the acquired signals to an external unit in real time.

1.2 Near-Field WPT System Design

This paragraph focuses on the EM design of a WPT platform that meets stringent requirements for compactness, EH efficiency and stability, and minimal interference with the natural behavior of small murine models. To fulfill these design objectives, we introduce a soft, flexible, and conformal WPT system specifically engineered to enable the battery-free operation of a miniaturized implantable device for optogenetic stimulation in small-size laboratory mice with OSA.

The proposed system, initially conceived in [13], is illustrated in Figs. 1.3, and it relies on an inductive resonant link operating at 13.56 MHz. A conformal TX array of series-connected coils powers a pair of miniaturized RX coils implanted on the mouse's back in a saddle-like configuration. Coverage of the RX coils with a polymeric material could provide protection and biocompatibility, and an alternative approach could avoid subcutaneous implantation entirely by designing the receiver as an external conformal fixture. Both strategies could be explored to assess feasibility and tolerability in freely moving animals. On the same RX module, the power rectification circuit is integrated and DC-connected to a μ-LED aligned with the hypoglossal nuclei, where the motoneurons innervating the tongue are located.

The novel TX coil configuration enables uniform, omnidirectional power coverage within the quasi-cylindrical experimental chamber (50 mm in height and 50 mm in radius), which is housed inside a whole-body plethysmograph for simultaneous monitoring of the animal's vital parameters during experiments, as pictured in Fig. 1.3(b). A dedicated aperture on the curved wall allows for continuous access to food and water throughout the procedure. Moreover, the strategic saddle-like RX placement not only increases the effective harvesting area but also improves tolerance to positional and angular misalignment, since the degrees of freedom of the back's movements and rotations are more limited compared to those of the head, while also avoiding additional bulk and dimension constraints on the small cranial region. As a result, the system ensures reliable energy transfer and continuous light delivery regardless of the mouse movements and positions, thereby enhancing operational robustness, animal comfort, and experimental reproducibility.

1.2.1 EM Design of the Transmitting Multi-Coil Array

The TX multi-coil array, shown on the left side of Fig. 1.3(a), consists of five series-connected coils, four rectangular ones distributed along the lateral wall, and a circular one placed on the cage floor. Their dimensions have been EM-optimized in CST Microwave Studio to ensure uniform, omnidirectional, and 3D magnetic field coverage of the entire region occupied by the mouse [13]. The predicted 3D field distribution is illustrated in Figs. 2 for two representative cross-sectional planes of the cylindrical chamber. Fig. 1.5(a) shows a vertical axial plane passing through the central axis of the structure (xy-plane, z = 0, see Fig. 1.3(a)), which cuts the cylinder into two symmetric halves and allows visualization of the field distribution along the cage height and diameter. Fig. 1.5(b) shows a horizontal transverse plane intersecting the chamber at y = 25 mm, corresponding to the maximum elevation reached by the mouse within the chamber and to the expected location of the implanted RX. In the axial plane, the series connection of the coils produces a constructive superposition of the magnetic field going from the bottom coil to the lateral ones, enhancing coverage in the center of the cage. In the transversal plane, the four lateral coils collectively provide coverage across multiple orientations, ensuring effective power delivery throughout the experimental volume.

The flexible substrate selected for the TX array enables the coils to conform and to adhere along the cylindrical chamber walls, markedly differing from the conventional approach of using a single transmitting coil, which typically cannot provide a uniform field distribution, thus requiring higher transmitted power—often 8–10 W in state-of-the-art systems [57] —to ensure the receiver always harvests sufficient power regardless of the animal's position. In contrast, our flexible multi-coil design, with series-connected smaller coils, achieves a uniform magnetic field distribution while maintaining effective power transfer within safety limits for implantable applications. The simulated equivalent inductance and loss resistance associated with this TX multi-coil configuration are namely $L_{TX,eq} = 1.69$ μH and $R_{TX,eq} = 0.8$ Ω.

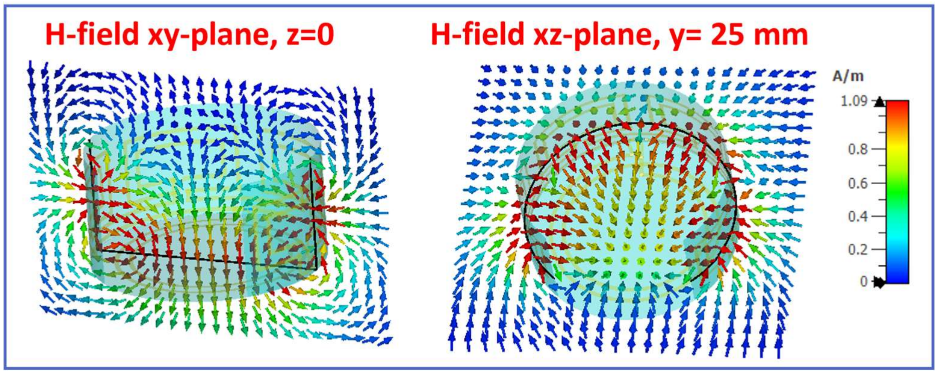

(a) (b)

Figure 1.5. Simulated magnetic field (H-field) distribution obtained by cutting the semi-cylindrical chamber in half: (b) vertical section along the axial (xy-plane) and (c) horizontal section along the transverse (xz-plane). ©2025 IEEE

1.2.2 Electromagnetic-Circuital Co-Design And Optimization Of The Receiving Implantable Device

The implantable RX device, depicted on the right-hand side of Fig. 1.3(a) and in more detail in Fig. 1.6, comprises two small identical rectangular coils with five turns each, spaced by 0.9 mm with 35-μm-thick and 0.41-mm-wide copper lines in rectangular shape, measuring $w_{RX} = 14$

mm and l_{RX} = 15 mm. Its geometry and positioning have been carefully designed and optimized from an EM standpoint to maximize EH, independent of the mouse's movements or orientation, thereby ensuring continuous operation of the μ-LED. Each RX coil exhibits a simulated inductance of $L_{RX,i=1,2}$ = 0.43 μH and a loss resistance of $R_{RX,i=1,2}$ = 0.38 Ω [14].

To assess the biological tissue impact on the EM performance, simulations were performed by modeling the receiver encapsulated between two 100-μm polyimide layers and embedded within a 3.5-cm-diameter tissue cylinder, represented as the union of four concentric cylindrical layers (skin, fat, muscle, blood) with realistic dielectric properties at 13.56 MHz (skin, 0.29-mm-radius: ε_r = 295, σ = 0.23 S/m; fat, 2.87-mm-radius: ε_r = 26, σ = 0.05 S/m; muscle, 7.17-mm-radius: ε_r = 142, σ = 0.6 S/m; blood, 7.17-mm-radius: ε_r = 219, σ = 1.1 S/m) [61]. The polyimide encapsulation was introduced not only for mechanical protection and biocompatibility but also to improve the EM compatibility of the RX resonator. Acting as a low-loss dielectric spacer, it partially decouples the resonator from the highly conductive tissue environment, mitigating conductivity-induced reactive loading and helping preserve stable coupling conditions. The simulation results demonstrated that the TX–RX link, in terms of inductive coupling, remains essentially unchanged when the receiver is embedded in biological tissue and moved across different positions and orientations within the cage. These findings indicate that, under the considered scenarios, biological tissues do not significantly influence the inductive coupling between the TX and RX coils and were therefore considered sufficient to reliably represent realistic in vivo operating scenarios.

Although real in vivo experimental conditions can involve additional sources of variability, the system was deliberately designed to operate in the lower HF band at 13.56 MHz, where magnetic near-field coupling is dominant and tissue absorption of the magnetic field is intrinsically limited. Thus, this design choice minimizes biological loading effects and ensures robust operation under realistic experimental conditions.

In addition, a preliminary EM safety assessment was carried out by evaluating the specific absorption rate (SAR) within the multilayer tissue model. Full-wave simulations were performed by applying the maximum transmitted power (1.5 W) used in the in vivo experiments. The obtained SAR distributions were analyzed in terms of localized and averaged values, confirming that tissue absorption remains within conservative safety margins for the considered exposure conditions.

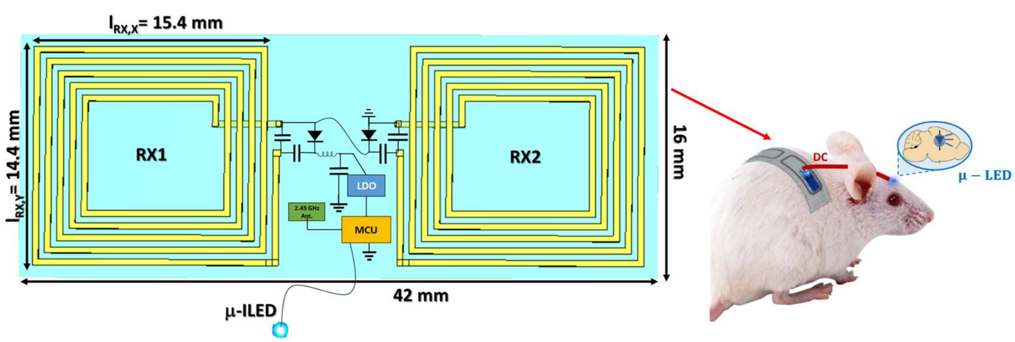

Figure 1.6. Close-up view of the RX module and its dorsal implantation strategy, designed as a “saddle” on the mouse’s back. The receiver includes two coils, each with a dedicated rectifier, along with the low drop-out (LDO) linear voltage regulator and microcontroller unit (MCU) circuitry. A DC connection links the electronics to the μ-LED, located at the hypoglossal nucleus where stimulation is delivered.

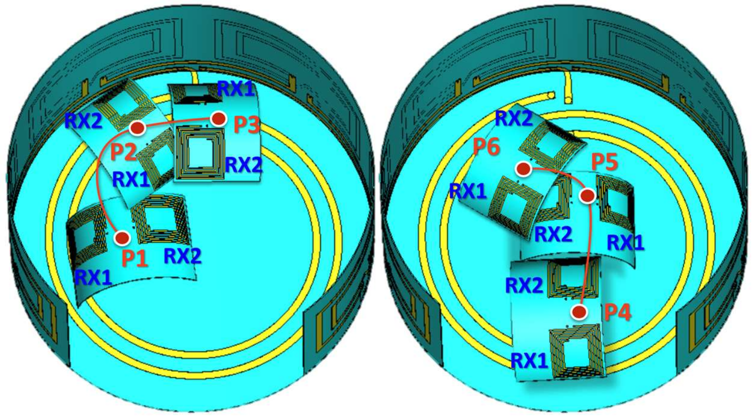

Figure 1.7. Simulated RX positions (Pi=1,…,6) within the TX multi-coil array arrangement inside the semi-cylindrical experimental chamber. [15]. © 2025 IEEE

The complete system, comprising both TX and RX coils, was first evaluated through EM simulations considering six representative RX positions within the chamber, denoted as Pi (i = 1,…,6) and illustrated in Fig. 1.7. Each position accounts for different RX–TX misalignment scenarios on the chamber's lateral wall and floor, replicating the possible angular orientations of the mouse during operation. The goal of this analysis was to optimize the power transfer efficiency (PTE) of the inductive link, ensuring consistent performance despite the animal's movements during in vivo experiments.

Subsequently, the EM-simulated impedance matrix of the resulting three-port network was imported into an electromagnetic circuit simulator, where a non-linear EM/circuit co-design was performed to fine-tune the WPT system. The corresponding circuit-equivalent model is presented in Fig. 1.8.

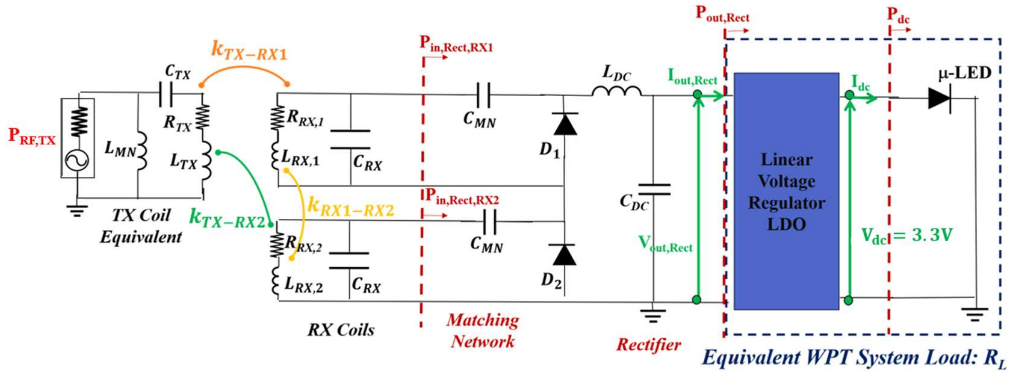

Figure 1.8. Overview of the complete WPT circuit: equivalent TX system and detailed RX device including resonating coils, rectifiers, voltage regulator, and μ-LED [15]. ©2025 IEEE

On the TX side, the series-connected multi-coil array is modeled by an equivalent inductance $L_{TX,eq}$ and resistance $R_{TX,eq,}$, both derived from EM simulations, and driven by a power source delivering $P_{RF,TX} = 31.78$ dBm ($\approx$ 1.5 W). On the RX side, the two identical receiving coils are represented by inductances $L_{RX,i=1,2}$, in series with their corresponding loss resistances $R_{RX,i=1,2}$.

To maximize the RF-to-RF PTE, a capacitor $C_{TX} = 68$ pF is connected in series with $L_{TX,eq}$, while two capacitors $C_{RX,i=1,2} = 270$ pF are connected in parallel with $L_{RX,i=1,2}$, forming a series–parallel resonant link at 13.56 MHz. The TX coil adopts a series-resonant configuration, which minimizes impedance at resonance, rendering it predominantly resistive and well matched to the 50-Ω output impedance of the RF source, thereby enabling maximum power delivery. Conversely, the RX coils use a parallel-resonant configuration, which increases the input impedance of the RX stage, improving matching with the rectifier input under the given frequency and power conditions. This complementary matching approach enhances overall PTE and ensures stable performance under variable loading.

Fine impedance matching is further achieved by inserting an additional inductance $L_{MN} = 100$ nH at the TX side and coupling each RX resonant coil to its single-stage rectifier through a matching capacitance $C_{MN} = 47$ pF. The rectifier employs Skyworks SMS-3923 RF Schottky diodes (46 V breakdown), cascaded and followed by a low-pass filter—comprising $L_{DC} = 22$ μH and $C_{DC} = 47$ nF —to supply a pure DC voltage to an Analog Devices LT1962 low-dropout (LDO) regulator. The regulator provides a stable output of $V_{DC} = 2.8$ V to drive a 465-nm Cree TR2227 blue μ-LED (270 × 220 × 50 μm^3).

All circuit parameters were derived through the previously described EM/circuit co-design using a nonlinear harmonic balance simulator. The LED power consumption was set to guarantee a radiant power of at least 5 mW—identified through physiological measurements as the minimum optical threshold required to activate the hypoglossal nuclei and elicit muscle contraction. According to the device datasheet, biasing the μ-LED at 2.8 V achieves a 5 mW optical output with a total power consumption of approximately 10 mW. The overall optimization process accounted for the voltage regulator's constraints: the rectifier output voltage must remain within the acceptable input range of the regulator, which requires at least 2.85 V to ensure a stable 2.8 V output, given its 50 mV dropout voltage. Consequently, the design was tuned to maintain the rectifier output between 2.85 V and 20 V across all possible positions of the freely moving animal, while still supplying the minimum 10 mW power required by the μ-LED at the lowest operating voltage.

Figure 1.8 reports the simulated maximum power point tracking (MPPT) performance for the six representative RX positions shown in Fig. 1.7. The left axis shows the rectifier output voltage $V_{out,rect}$, and the right axis the corresponding DC output power $P_{out,rect}$, both plotted against the output current $I_{out,rect}$. The results indicate that, in all simulated cases, the DC power at the minimum rectifier voltage (2.85 V) comfortably exceeds the optical stimulation threshold. This ensures that, even when a microcontroller unit (MCU) is introduced between the regulator and the μ-LED to generate pulsed stimulation, the rectifier can still deliver sufficient power to drive both the MCU and the μ-LED. Moreover, the rectifier voltage never approaches the 20 V upper limit, guaranteeing safe regulator operation. At maximum rectifier voltage, the corresponding input current remains above the minimum required for proper regulation, confirming stable and reliable performance across all operating conditions.

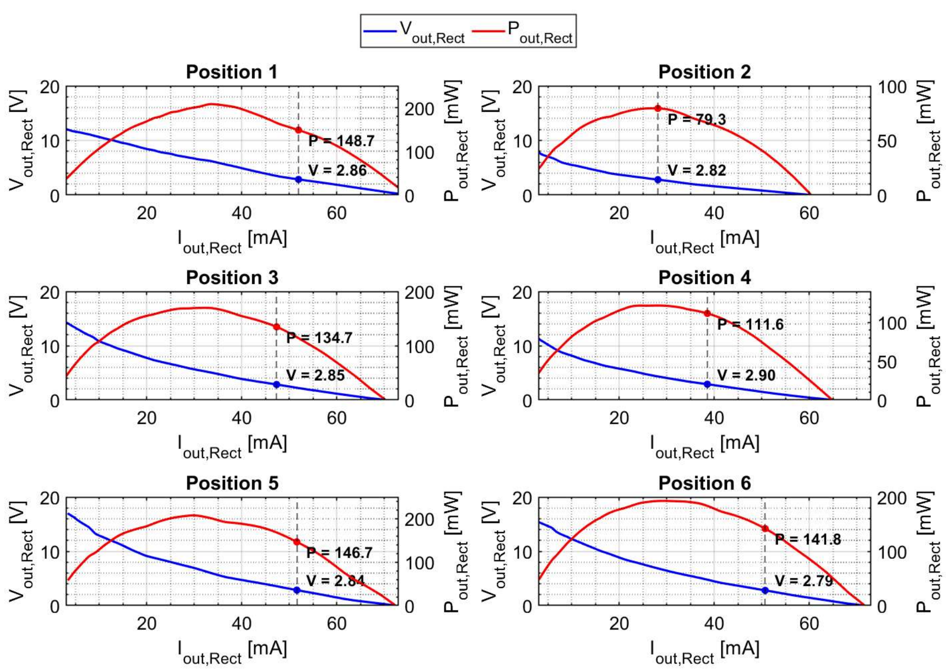

Figure 1.9. MPPT performance of the simulated circuit at each position Pi=1,..,6: left y-axis: rectifier output voltage $V_{out,Rect}$; right y-axis: rectifier DC output power $P_{out,Rect}$. All graphs are plotted as a function of the rectifier output current $I_{out,Rect}$.

1.3 Wireless Power Transfer Efficiency: RF-to-RF Modeling and End-to-End Measurements

To achieve a conformal and flexible design, the system prototype was fabricated on a 25-µm-thick Kapton substrate ($\varepsilon_r = 3.4$, $tan(\delta) = 0.01$) with 35-µm-thick copper metallization (Fig. 1.3(b)). The inherent flexibility of Kapton allows the TX to conform seamlessly to the chamber's curved structure and the RX to fit comfortably to the mouse's back. The weight of the receiver prototype intended for subcutaneous implantation on the mouse's back was measured and found to be 0.6 g. Considering an average mouse body weight of 22.5 g, the device corresponds to approximately 2.7% of the total body weight. This low relative weight indicates that the implant is unlikely to affect the animal's natural movements, posture, or overall body load, thereby minimizing mechanical interference and ensuring a non-invasive implantation.

The following paragraphs present the experimental validation of the proposed platform, including the characterization of the RF-to-RF link, the assessment of the overall WPT system performance, and in-vivo testing on mice to evaluate the device's capability to wirelessly drive tongue muscle stimulation, thereby demonstrating the effectiveness of the fully wireless optogenetic system.

1.3.1 RF-to-RF Measured Efficiency Estimation

The impedance values of the fabricated TX and RX prototypes in Fig. 1.3(b) were first extracted employing the Keysight N9952A FieldFox VNA, leading to measured inductances and loss resistances mostly consistent with the simulated ones: $L_{TX,eq}$ = 1.92 μH and $R_{TX,eq}$ = 1.5 Ω for the TX and $L_{RXi=1,2}$ = 0.44 μH and $R_{RXi=1,2}$ = 0.76 Ω for the RX coils.
Given the measured impedances of the three different coils, their quality factors (Q) were calculated as:

$$Q_{TX} = \omega \frac{L_{TX}}{R_{TX}}, \tag{1.1}$$

$$Q_{RXi=1,2} = \omega \frac{L_{RXi=1,2}}{R_{RXi=1,2}}, \tag{1.2}$$

resulting in Q_{TX} = 104 and $Q_{RX,i=1,2}$ = 53, with f = 13.56 MHz and $\omega = 2\pi f$.

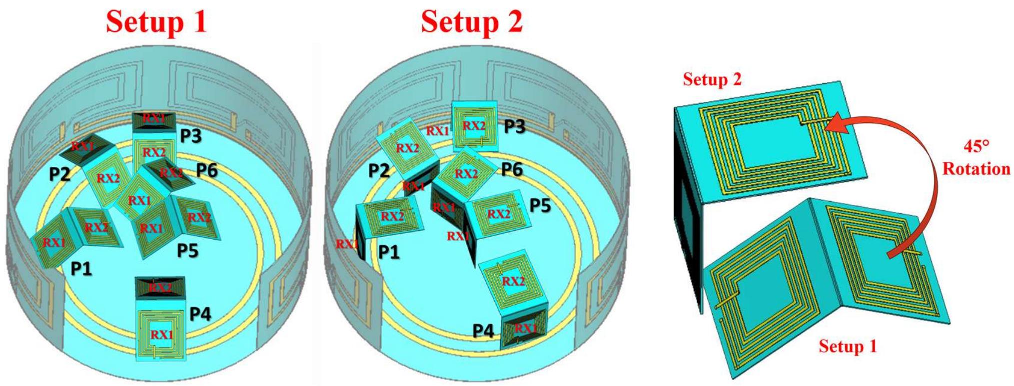

(a) (b)

Figure 1.10. (a) Measured RX positions (Pi=1,...,6), and orientations, Setup 1 and 2 (b), within the TX multi-coil array arrangement inside the semi-cylindrical experimental chamber. [14]. ©2024 IEEE

The RX coils were placed at six representative spatial locations within the chamber, as illustrated in Fig. 1.10(a), to capture a variety of coupling scenarios. For each position, two distinct configurations—Setup 1 and Setup 2—were analyzed (see Fig. 1.10(b)). Setup 1 corresponds to the awake mouse condition, where the RX coils are mounted dorsally in a saddle-like arrangement. Setup 2 replicates a potential sleeping posture, with the RX coils rotated by 45° to mimic the mouse lying on its side. These configurations were chosen to reflect the range of orientations and positions that may occur during in-vivo experiments, enabling a thorough evaluation of the system's robustness.

Importantly, compared to previous studies [58], our system exhibits improved stability under similar misalignment conditions. This is primarily because the RX coils positioned on the mouse's back undergo more restricted movements than those placed on the skull, thereby reducing sensitivity to positional variations. The objective of this analysis was to maximize the RF-to-RF PTE, ensuring consistent performance across all expected RX positions and orientations.

First, the coupling coefficients between the TX and one RX only are derived from measurements for the two setups of Fig. 1.10 and for the respective six locations: as expected, the results shown in Fig. 1.11 demonstrate that using a single RX leads to significant coupling degradation for certain mouse positions, thereby confirming the effectiveness and necessity of the dual-receiver configuration proposed in this work.

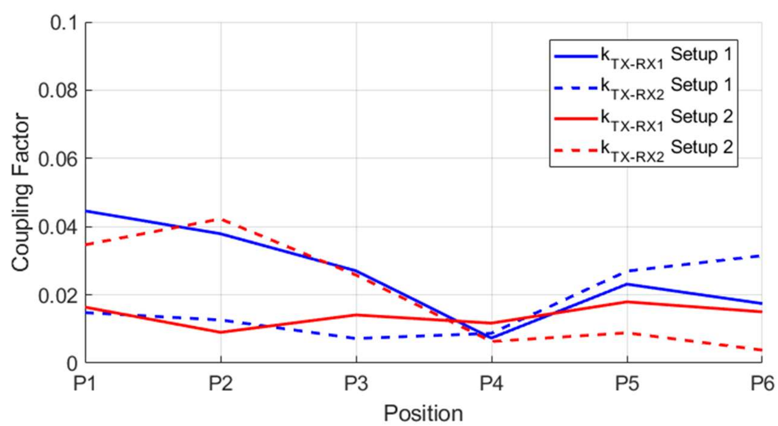

Figure 1.11. Coupling factor between TX and RX1 ($k_{TX\text{-}RX1}$), and between TX and RX2 ($k_{TX\text{-}RX2}$) placed in the six spatial positions P1,..,6 for Setup 1 and Setup 2. [38].

Indeed, a total effective coupling factor k_{tot} must be considered for the present implementation, which can be calculated as follows [62]:

$$k_{tot} = \frac{\sqrt{2}}{2}\frac{(k_{TX-RX1} + k_{TX-RX2})}{\sqrt{1 + k_{RX1-RX2}}} \tag{1.3}$$

which accounts for the overall link when multiple receivers are present and represents the effect of the combined coupling between the transmitting coil and each receiving coil, as well as the coupling between the two RXs simultaneously [62]. The results derived by measurements are shown in Fig. 1.12 for the two setups, showing the advantage of the proposed combined two-RX solution. The coupling factor between RX1 and RX2 ($k_{RX1\text{-}RX2}$) has also been measured, and it results to be equal to –0.017. Indeed, as shown in Fig. 1.12, k_{TOT} is slightly lower than the superposition of the individual coupling factors, probably due to the small coupling between the two receivers.

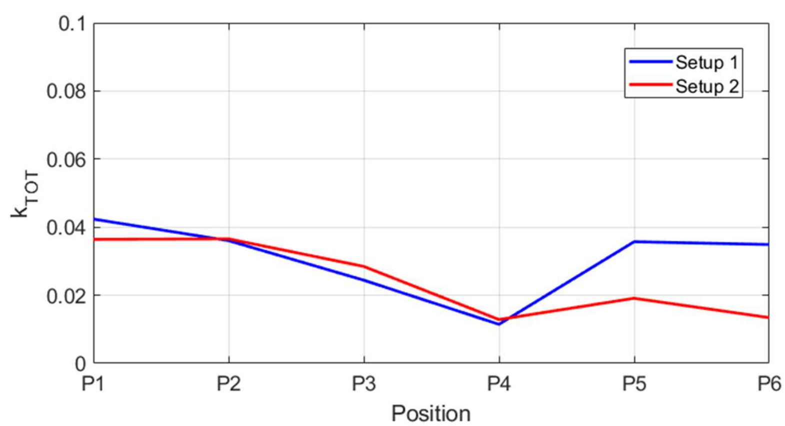

Figure 1.12. Total effective coupling factor k_{TOT} for the two-receiver setups; measurements with both setups and six different positions Pi (i=1,..,6) have been evaluated. [38].

Based on these measurements, the RF-to-RF efficiency of the inductive link was estimated for each receiver using the multiport network approximation [63], [64]. The efficiency of the TX-RX1 link is given by:

$$\eta_{RF-to-RF,TX-RX1} = \frac{(k_{TX-RX}^2 \cdot Q_{TX} \cdot Q_{RX})}{1 + k_{TX-RX}^2 \cdot Q_{TX} \cdot Q_{RX} + k_{TX-RX}^2 \cdot Q_{TX} \cdot Q_{RX} + k_{RX1-RX2}^2 \cdot Q_{RX} \cdot Q_{RX}} \tag{1.4}$$

Similarly, the efficiency of TX-RX2 link is defined as follows:

$$\eta_{RF-to-RF,TX-RX2} = \frac{(k_{TX-RX2}^2 \cdot Q_{TX} \cdot Q_{RX2})}{1 + k_{TX-RX}^2 \cdot Q_{TX} \cdot Q_{RX2} + k_{TX-RX2}^2 \cdot Q_{TX} \cdot Q_{RX} + k_{RX1-R}^2 \cdot Q_{RX1} \cdot Q_{RX}} \tag{1.5}$$

The efficiency values reported in this paragraph were estimated using an analytical model derived for magnetically coupled resonant systems. The expression is valid under the assumption of resonant operation, where all coils are tuned to the same frequency, and weak to moderate coupling conditions, typically when the term $k^2_{TX\text{-}RXi} \cdot Q_{TX} \cdot Q_{RX} < 1$. In this regime, the energy transfer between coils can be accurately approximated by the product of the coupling coefficient and the quality factors of the resonators. Furthermore, the model assumes perfect impedance matching at both the TX and RX sides, so that no additional losses are introduced by mismatch or parasitic elements. Under these conditions, the simplified analytical formulation provides a reliable estimation of the RF-to-RF efficiency and allows meaningful comparison between different coil configurations and receiver placements.

As shown in Fig. 1.13, the estimated RF-to-RF efficiency exhibits clear dependence on the positioning of the receivers. While peak efficiencies approach 60–65% for the best spatial configurations, mutual loading effects reduce the efficiency in the less favorable cases (i.e., P4 for Setup 1 and P2 for Setup 2).

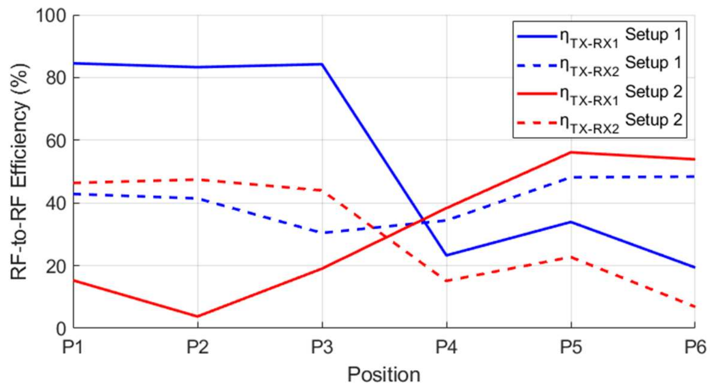

Figure 1.13. Estimated RF-to-RF efficiencies between TX and RX1 ($\eta_{TX\text{-}RX1}$), and between TX and RX2 ($\eta_{TX\text{-}RX2}$) placed in the six spatial positions P1,..,6 for Setup 1 and Setup 2. [38].

1.3.2 RF-to-DC Measured Efficiency

To evaluate the overall practical performance of the proposed system, RF-to-DC conversion measurements were carried out at the rectifier output (as described in the previous Section) using the optimal load for the RX module. The DC output voltage ($V_{out,DC}$) and power ($P_{out,DC}$) were characterized across the six representative positions and for both setups, with a transmitted power of $P_{TX} = 31.78$ dBm (approximately 1.5 W) supplied by the RF signal generator (Keysight N5183B MXG X-Series) to the TX unit. Fig. 1.14 reports the measured DC voltage and power at the rectifier output under optimal load conditions. As expected, these results are strongly correlated with the coupling factors measured earlier: the higher the coupling factors, the higher the DC output voltage and power.

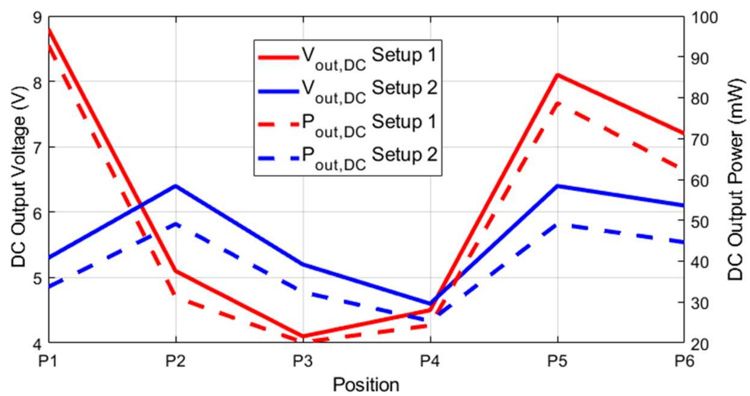

Figure 1.14. Measured rectifier output DC voltage ($V_{out,DC}$) and power ($P_{out,DC}$) at optimal load. The measurements have been performed in the six spatial positions P1,..,6 for setup 1 and setup 2. [38].

Finally, Fig. 1.15 summarizes the overall RF-to-DC efficiency of the complete WPT system, from RF power delivered to the transmitter to DC power available at the rectifier output, calculated as follows:

$$\eta_{RF,TX-DC} = \frac{P_{out,DC}}{P_{RF,TX}}, \tag{1.6}$$

Although the RF-to-RF efficiency of the inductive link can reach relatively high values, the measured end-to-end efficiency exceeds 6% for the best position (i.e., P1 for Setup 1). Nevertheless, these values are remarkable when considering the large size mismatch between the transmitting and receiving coils, which represents a particularly challenging condition for efficient WPT.

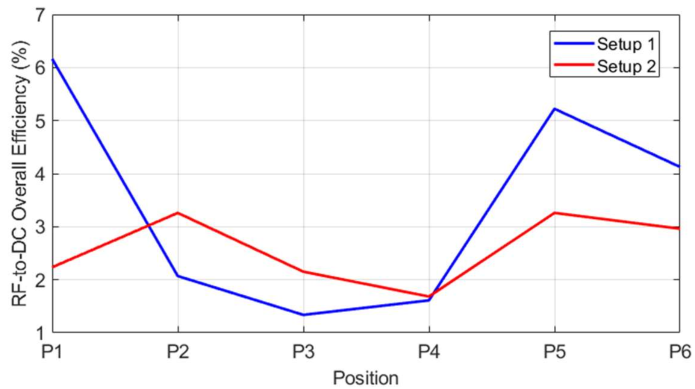

Figure 1.15. Measured overall $\eta_{RF,TX\text{-}DC}$ WPT system percentage efficiency considering (6). [38].

The experimental results show that RF-to-RF efficiency depends on spatial positioning and coil alignment, with peak efficiency at positions of highest coupling. However, despite alignment variations, the system maintains a robust link across the entire mouse plethysmograph surface. In multi-receiver configurations, power is delivered simultaneously to both receivers, increasing total transferred power compared to a single-receiver setup, demonstrating the link's reliability and suitability for multiple devices. Considering the measured coupling factors, RF-to-RF efficiencies, and rectifier outputs, the end-to-end efficiency is consistently confirmed. Even at the most misaligned configuration (Setup 1, position P3), the delivered DC power reached 20 mW—well above the 10 mW required to drive the µ-LED and achieve the minimum 5 mW optical output for effective neurostimulation.

1.4 In-Vivo Measurements of Optogenetic Stimulation

1.4.1 Animals and Viral Injections

The in-vivo tests of the wireless, battery-free device were performed on an adult male mouse (wild-type, C57BL/6J background) maintained at 23 °C under a 12:12 h light–dark cycle (lights on at 9 am, Zeitgeber Time 0, ZT0) with free access to food (4RF21 diet, Mucedola, Italy) and water. For system validation, a prototype device was implanted in an anesthetized mouse (20–25 g, skull 2 × 1 cm) to modulate tongue contractions via optogenetic stimulation of the hypoglossal nucleus. The animal, selectively expressing light-sensitive receptors in this region, was anesthetized with 2% isoflurane in O_2 and implanted with two PFA-coated stainless steel wires (cat. no. 793500, A-M Systems, USA) in the tongue to record contractions. A commercial LED was then inserted into the brain and programmed to deliver light pulses at 5 Hz and subsequently at 1 Hz while tongue contractions were continuously monitored, as described in detail in the following paragraph.

To achieve precise anatomical localization and expression of light-sensitive ChR2 employed an adeno-associated viral (AAV) vector carrying the plasmid hSyn-hChR2(H134R)-EYFP has been used. This viral vector ensured the selective expression of ChR2 in neurons (due to the presence of the hSyn promoter) and the possibility of fluorescence detection of transfected cells (due to the presence of the EYFP fluorescent gene report). The AAV was injected into the rostral portion of the hypoglossal nucleus (total volume: 400 nL, injection speed: 10 nL/s, titer: 1 x 10^{11} vg per ml) which contains motoneurons innervating intrinsic and extrinsic tongue muscles, including the genioglossus muscle [65]. The mouse was anaesthetized (2% isoflurane in O_2) and placed in a stereotaxic frame (71000 Automated Stereotaxic Instrument, RWD Life Science Co., China). The skull was exposed, and a small burr hole was made to position a pre-pulled glass micropipette connected to a microsyringe injector pump. Stereotaxic coordinates relative to bregma were anteroposterior –7.20 mm, mediolateral 0.0 mm, dorsoventral –4.8 mm, based on [66]. After the injection, the mouse skin was sutured and analgesic (Carprofen 0.1 mg, Pfizer, Italy) and antibiotic (Veterinary Rubrocillin, Intervet, Italy) were administered.

Five weeks later, the mouse underwent surgery to implant electrodes to record genioglossus (GG) muscle activity and the optogenetic device into the rostral portion of the hypoglossal nucleus. This interval was necessary to achieve stable and high-level expression of ChR2 in the targeted motoneurons.

1.4.2 In-Vivo Experimental Measurements Results for Optogenetic Stimulation and Tongue Muscle Recording

Under general anesthesia (2% isoflurane in O_2), the mouse was placed in the supine position, and a small midline incision was performed in the submental region (see Fig. 1.16). For the acute differential GG electromyographic (ggEMG) signal detection, two multi-stranded PFA-coated stainless steel wires were inserted in the targeted GG muscle from the base of the tongue using a 27 G needle [67]. The ggEMG signal was amplified, filtered between 300 and 500 Hz using Model 1700 Differential AC Amplifier (A-M Systems, USA) and digitized at a sampling rate of 500 Hz.

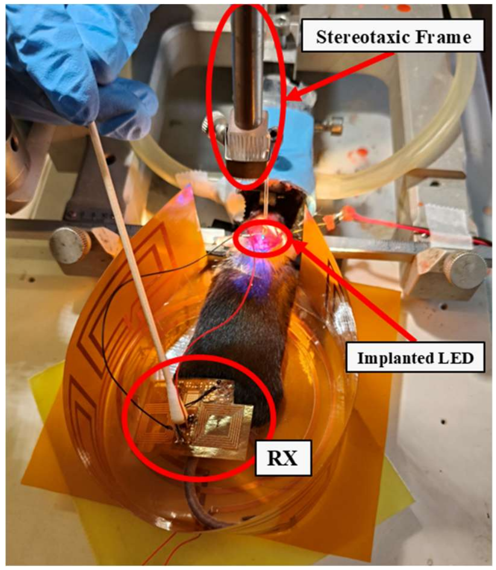

Figure 1.16. In-vivo measurement setup with TX and RX devices (the RX is just positioned on top of the mouse but still subdermally implanted) and the mouse under general anesthesia in a stereotaxic frame for LED implantation in the brain. [38].

After obtaining a stable ggEMG signal, the mouse was secured in a stereotaxic frame with its snout positioned in an anesthetic mask. Prior to device implantation, the radiant power output of the selected 470 nm blue commercial LED (1×0.5 mm^2) was quantified using a power meter (PM100D, Thorlabs, USA) coupled with a photodiode sensor (S120C, Thorlabs, USA). The LED delivered a measured radiant flux of 2.4 mW at its tip. Subsequently, the LED was mounted at the tip of a 25 G needle fixed to the stereotaxic holder and inserted into the brain along the midline (mediolateral coordinate: 0 mm), at –7.20 mm posterior and –4.7 mm dorsoventral to bregma, positioned just above the viral injection site [68]. Functional activation of the tongue muscles was then assessed at two stimulation frequencies: 5 Hz (100 ms pulse and inter-pulse duration) and 1

Hz (500 ms pulse and inter-pulse duration). Figure 1.15 illustrates the in-vivo experimental setup, where the TX and RX units are arranged to enable wireless power transfer while the anesthetized mouse is stabilized in the stereotaxic frame. This configuration allows precise LED implantation and stable conditions for subsequent optogenetic stimulation experiments.

Figures. 1.17–1.19 illustrate the natural tongue ggEMG activity and the corresponding responses to optogenetic light stimulation at two different frequencies (1 Hz and 5 Hz). The measurements were carried out over a total interval of 212 seconds. Within this window, periods with no stimulation (natural activity) and periods with stimulation at the two frequencies were analyzed and are represented in the following figures.

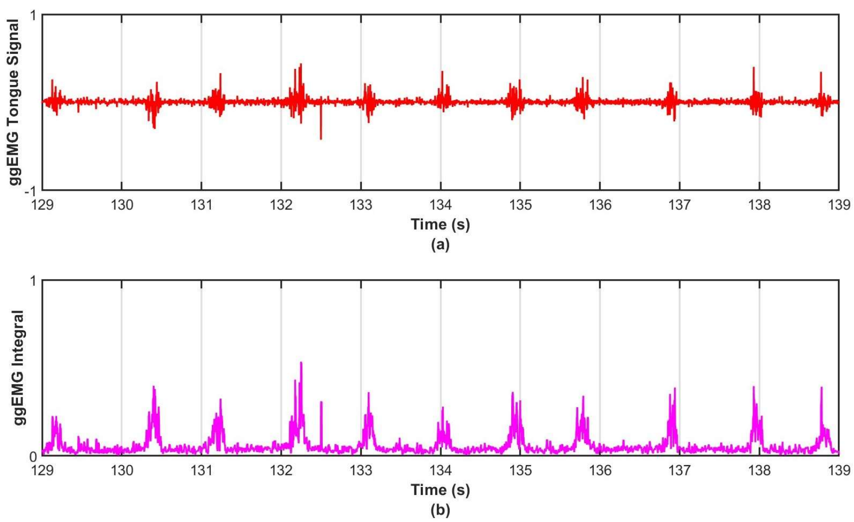

Figure 1.17. Tongue ggEMG activity in the absence of light stimulation: (a) raw ggEMG signal, (b) short-term integral of the ggEMG signal. [38].

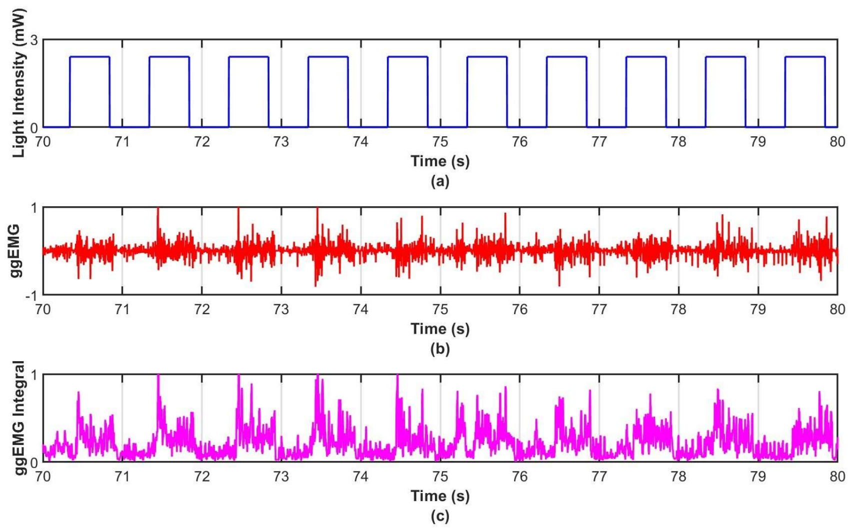

Figure 1.18. Light stimulation at 1 Hz and corresponding tongue ggEMG response: (a) light intensity, (b) normalized ggEMG signal, (c) short-term ggEMG integral. [38].

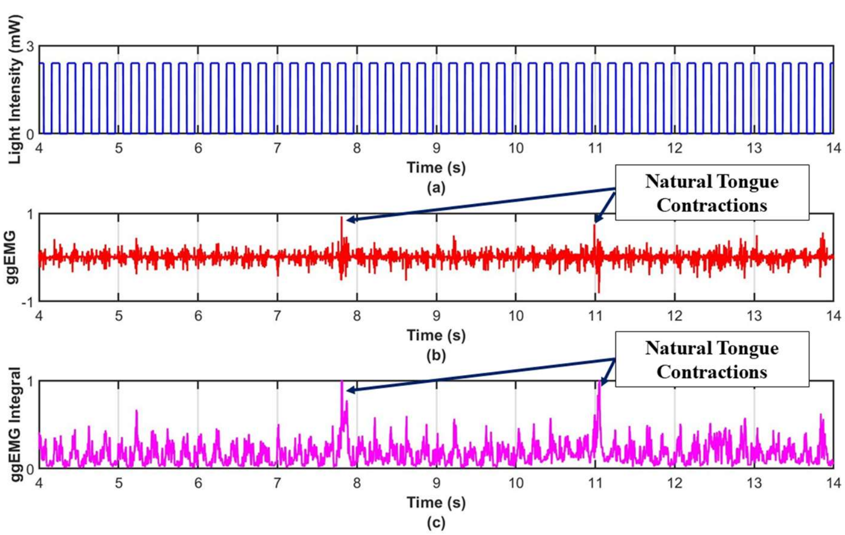

Figure 1.19. Light stimulation at 5 Hz and corresponding tongue ggEMG response: (a) light intensity, (b) normalized ggEMG signal, (c) short-term ggEMG integral. The superposition of a natural contraction and a light-induced response is also highlighted at 7.8 and 11 seconds. [38].

Figure 1.17 illustrates a representative ggEMG recording segment acquired in the absence of optical stimulation, depicting the spontaneous tongue muscle activity (panel a) and its short-term integral (panel b). Figures 1.18 and 1.19 correspond to trials performed with optical stimulation at 1 Hz and 5 Hz, respectively. In these figures, panel (a) displays the square-wave light intensity profile delivered to the tissue (mW), panel (b) shows the normalized ggEMG signal, and panel (c) presents its short-term integral. The time axis indicates absolute time relative to stimulation onset (defined as time zero), enabling precise temporal alignment between the optical stimulus and the evoked physiological response.

The short-term ggEMG integral was calculated as the cumulative sum of the absolute ggEMG amplitude within a 0.01 s moving window, matching the 500 Hz acquisition rate. This processing emphasizes the instantaneous muscle activity and highlights the cumulative response associated with each light pulse. Both the ggEMG traces and their integrals were normalized to the maximum value recorded during the entire 212 seconds session, allowing direct comparison between stimulated and unstimulated periods and facilitating the interpretation of relative changes in activity. Under this normalization, the response amplitudes evoked by optical stimulation clearly exceed those of the baseline, spontaneous tongue activity.

Additionally, in Fig. 1.19, a superposition between a spontaneous contraction and a light-evoked response can be observed at approximately 7.8 and 11 seconds.

These representations quantitatively illustrate the frequency-dependent modulation of tongue muscle activity and demonstrate the capability of the short-term integral to capture the cumulative post-stimulus response within each analysis window.

1.5 Conclusion

This chapter presents a fully wireless, battery-free optogenetic platform for the targeted stimulation of hypoglossal motoneurons in small murine models of OSA, enabled by a conformal near-field WPT system operating at 13.56 MHz. The platform has been specifically engineered for use in small rodents commonly employed in preclinical research, with the implant miniaturized to comply with the anatomical and experimental constraints of these models. The system demonstrates robust energy delivery independent of animal orientation or positioning, and in-vivo validation confirmed its capability to evoke tongue muscle contractions with sufficient optical power while maintaining minimal invasiveness. These findings establish the feasibility of employing lightweight, wireless, battery-free optoelectronic implants as an alternative to conventional fiber-based systems, thereby facilitating more naturalistic and reproducible behavioral studies.

Chapter 2. Innovative 3D Printing Techniques for the Design of a Dual-Port Wearable Rectenna Enabling Energy Harvesting and UWB Backscattering

This Chapter is based on the following articles:

[29] G. Battistini, G. Paolini, D. Masotti, and A. Costanzo, "Innovative 3-D Printing Processing Techniques for Flexible and Wearable Planar Rectennas," in *2022 Wireless Power Week (WPW)*, 2022, pp. 294–297.

[28] G. Battistini, G. Paolini, D. Masotti, and A. Costanzo, "Wearable Coplanar-Fed 2.45 GHz-Rectenna on a Flexible 3D-Printable Low-Cost Substrate," in *2022 52nd European Microwave Conference (EuMC)*, 2022, pp. 72–75.

[30] G. Battistini, G. Paolini, D. Masotti, and A. Costanzo, "3-D Etching Techniques for Low-Cost Wearable Microwave Devices in Grounded Coplanar

Waveguide," in *2022 IEEE MTT-S International Microwave Biomedical Conference (IMBioC)*, 2022, pp. 63–65.

[26] G. Battistini, G. Paolini, A. Costanzo, and D. Masotti, "A Novel 3-D Printed Dual-Port Rectenna for Simultaneous Energy Harvesting and Backscattering of a Passively Generated UWB Pulse," *IEEE Trans Microw Theory Tech*, vol. 72, no. 1, pp. 812–821, 2024.

[27] G. Battistini, G. Paolini, A. Costanzo, and D. Masotti, "3D-Printable Rectenna for Passive Tag Localization Exploiting Multi-Sine Intermodulation," in *2023 IEEE/MTT-S International Microwave Symposium - IMS 2023*, 2023, pp. 1077–1080.

This works were supported in part by the Italian Ministry of Education, University and Research (MIUR) within the framework of the PRIN 2017-WPT4WID ("Wireless Power Transfer for Wearable and Implantable Devices") project under Grant 2017YJE9XK and in part by the European Union through the Italian National Recovery and Resilience Plan (NRRP) of Next Generation EU, partnership on "Telecommunications of the Future" (Program "RESTART") under Grant PE00000001.
The paper [26] is an expanded version from the IEEE MTT-S International Microwave Symposium (IMS 2023), San Diego, CA, USA, June 11–16, 2023.

2.1 Introduction

Within this Chapter, it is demonstrated how, thanks to the AM process, 3D printing enables the development of innovative design strategies for realizing efficient antenna substrates, even when employing low-cost, 3D-printable plastic or resin materials. By leveraging AM and 3D printing, both the geometrical and EM characteristics of the substrate can be precisely tailored, providing unprecedented design flexibility together with a fast, straightforward, and cost-effective fabrication process, offering clear advantages over conventional micromachining techniques typically used for rigid RF substrates and microwave components [69], [70]. Such freedom in design opens new possibilities for realizing flexible, stretchable, and conformal devices that can adapt to soft, curvilinear body surfaces—an essential requirement for wearable systems [71].

The materials most commonly used in AM such as acrylonitrile butadiene styrene (ABS) and polylactic acid (PLA), are typically optimized for mechanical properties (elasticity, robustness, temperature resistance) rather than EM performance, since these polymers exhibit relatively high dielectric losses ($\varepsilon_r \approx 2.7$, $tan(\delta) \approx 0.01$ at 1 MHz), which can degrade propagation and radiation efficiency in RF applications.

To mitigate their EM limitations, 3D printing can be leveraged to tailor substrate mechanical and EM properties—through controlled infill ratios and material structuring and engineering—to improve their dielectric characteristics and, thus, performance.

Unlike traditional costly and time-consuming subtractive fabrication methods—e.g., micromachining or etching—which produce only two-dimensional (2D) layouts but do not provide access to the internal structure [72], [73], AM enables the creation of fully volumetric, customized materials. Consequently, it becomes essential to accurately determine the dielectric properties of multiple test-printed samples prior to undertaking RF design, as variations in printer settings (resolution, speed, and infill factor) and process tolerances (e.g., shrinkage, filament flow, voids) play a crucial role in achieving high-accuracy prototypes with well-defined dielectric parameters, namely relative dielectric permittivity and loss tangent. An uncertainty margin must be considered for samples printed via fused deposition modeling (FDM), due to material shrinkage during cooling or uncontrolled filament flow, which can generate small air gaps between adjacent printed lines. Such porosity, typically around 15% even at full infill, can impact RF performance when the wavelength becomes comparable to the air gaps, potentially leading to structural and EM anisotropy [74].

Despite these challenges, AM allows the co-optimization of mechanical and EM properties for specific applications. For instance, the infill factor can be deliberately adjusted to tune the dielectric response, as shown in [69] for 3D-printed dielectric lenses. Furthermore, low infill percentages with a high empty/full ratios can be used to enhance radiation efficiency, particularly valuable in radiating elements, whereas higher infill densities are preferred for miniaturized or mechanically robust structures and circuit platforms.

Among the various material characterization approaches reported in the literature, this Thesis focuses on resonant-based techniques [75]. In particular, the microstrip T-resonator topology is considered [76],[77], which provides a simple yet effective configuration for broadband dielectric extraction. It consists of a T-shaped microstrip with an open-ended quarter-wavelength stub and feed lines, exhibiting resonances at odd multiples of its fundamental frequency. By comparing measured S-parameters (via a Vector Network Analyzer (VNA)) with full-wave simulations performed in CST Microwave Studio (MS), across varying ε_r and σ, the dielectric properties can be extracted with good accuracy.

This approach has been widely employed in the literature for characterizing unconventional fabric or 3D-printable materials used as substrates of wearable rectennas. Examples include pile tissue ($\varepsilon_r = 1.23$, $tan(\delta) = 0.0019$) [76]; the most common materials used in fused filament fabrication (FFF) materials, ABS and PLA with $\varepsilon_r \sim 2.45$ and $tan(\delta) \sim 0.005$ in the frequency range 2–60 GHz for ABS, and $\varepsilon_r \sim 2.65$ and $tan(\delta) \sim 0.03$ up to 10 GHz for PLA [26], [78]; and flexible 3D-printable resins like Flexible 80A, characterized up to 6 GHz with $\varepsilon_r = 2.67$, $tan(\delta) = 0.086$, and electrical conductivity σ of 5.36×10^{-3} S/m [29].

Like Flexible 80A, ABS, and PLA, many other 3D-printable plastics and resins exhibit significant dielectric losses when used as substrates for antennas and RF devices. To overcome these limitations, various innovative design and fabrication techniques have been explored in this Thesis to reduce the impact of losses and to enhance both wave propagation and radiation performance [70]. As demonstrated in [29], grounded coplanar waveguides

(GCPWs)— which also provide additional shielding for ensuring wearability and safe operation of the RF prototype on human body—–outperform microstrip transmission lines in lossy materials since their quasi-transverse electromagnetic (quasi-TEM) field is partly confined in air rather than within the dielectric. Leveraging the enhanced design flexibility of 3D printing, in this work the substrate was selectively removed in the gaps between the signal and ground conductors to form rectangular-shaped cavities, as shown in Fig. 2.1(a,b). Different types of dielectric etchings have been investigated with the twofold goal of minimizing the electric field interaction with the lossy material, while maintaining mechanical stability of the structure. This approach led to significantly reduced propagation losses and improved transmission efficiency, especially at higher frequencies, as proved by the results in Fig. 2.1(c).

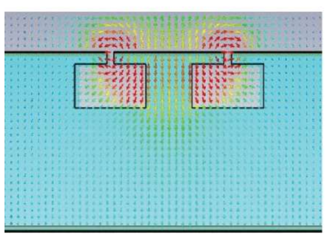

(a)

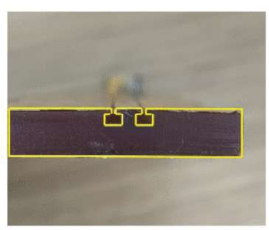

(b)

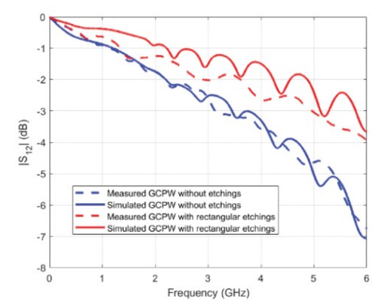

(c)

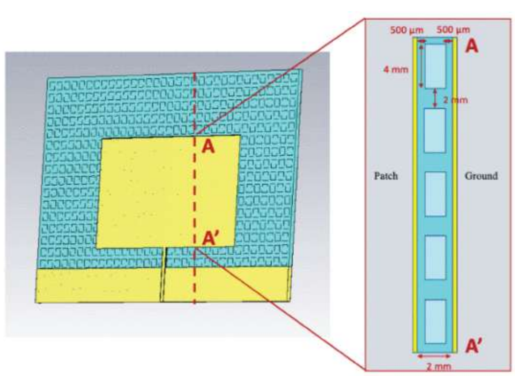

(d)

(e)

Figure 2.1. (a) CST MS layout and (b) prototype of the GCPW realized with rectangular etchings on a 2-mm-thick Flexible 80A; (c) comparison between $|S_{12}|$ curves of a measured microstrip line and a GCPW realized with copper tape on a sample of Flexible 80A substrate; (d) layout of the designed coplanar patch antenna, with a callout on the weft of the transversal section of the 3D printed engineered substrate, and (e) picture of the fabricated rectenna prototype. [29]. © 2022 IEEE

Building upon these findings, a wearable 2.45-GHz rectenna on Flexible80A was realized, as pictured in Figs. 2.1(d,e). By adopting the design/engineering techniques described in [24], [79], selectively removing 4 mm × 4 mm × 0.5 mm cavities within the substrate while preserving 500 µm outer layers to support the metal films, the antenna achieved a twofold improvement in radiation efficiency compared to the unetched version.

Subsequently, this concept was extended in [28] to maximize radiation performance by almost completely hollowing out the substrate below the patch metallization resulting in a quasi-air-filled solution, leaving only small support pillars [Fig. 2.2(a)]. This configuration yielded a dramatic efficiency increase (from 6% to 57%), although at the cost of mechanical robustness, as external deformation could lead to unpredictable frequency shifts and performance degradation.

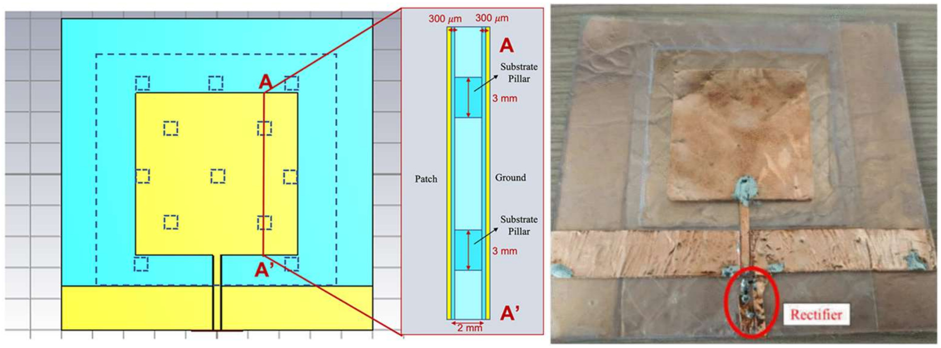

(a) (b)

Figure 2.2. (a) Layout of the designed 2.45 GHz coplanar-fed patch antenna, with a callout on the weft of the transversal section of the substrate, and (b) fabricated prototype on a 3D-printed sample of Flexible 80A with adhesive copper. [28]. ©2022 IEEE

Hence, building upon the conclusion that the design freedom offered by AM must be carefully balanced between EM performance and structural integrity, this Chapter investigates the design and realization of a 3D-printed rectenna system fabricated entirely using PLA, a cost-effective and moderately lossy dielectric material suitable for AM processes. The proposed system, schematically shown in Figs. 2.3, consists of two seamlessly integrated subsystems: a radiating section printed on a thick (2 mm) engineered-PLA substrate with high porosity, and a rectifying circuit section printed on a thinner (0.5 mm) PLA solid substrate. This architecture enables both energy autonomy and accurate localization functionalities through the passive generation of a quasi–UWB pulse [80], [81], [82], [83]. UWB localization, and in particular impulse-radio UWB (IR-UWB), is known to provide sub-meter accuracy and robustness against multipath and interference [84], [85], [86].

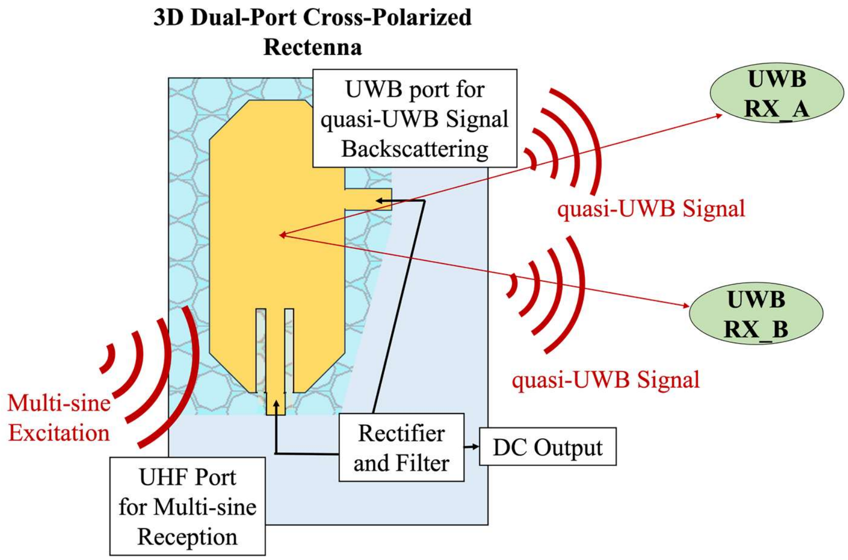

(a)

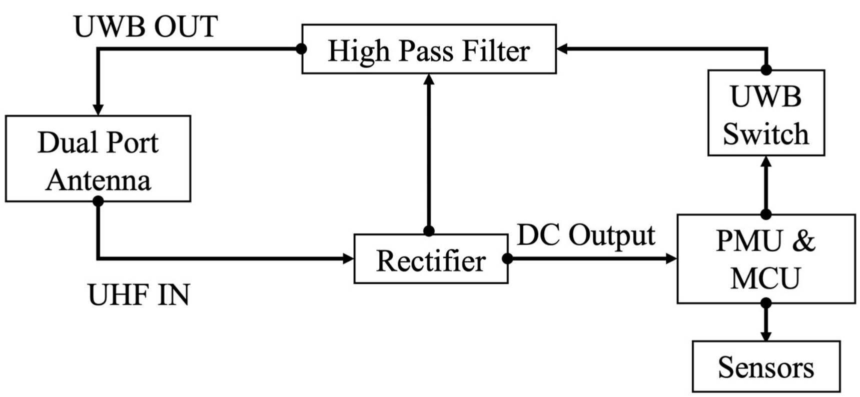

(b)

Figure 2.3. (a) Schematic representation of the proposed 3D printed dual-port rectenna: the UHF port receives a multi-sine RF power; the nonlinear rectifier converts it into DC and into higher harmonic and IM products that are then radiated through the UWB port. (b) Block diagram of the system integrated with low-power control electronics for energy-autonomous UWB communication and sensing. [26]. ©2024 IEEE

A preliminary version of this system was introduced in [27], inspired by natural structural architectures such as honeycomb geometries, which combine lightweight characteristics with high mechanical resilience [24], [87], [88], [89], [90]. In the present work, a novel non-planar 3D-printed PLA structure is proposed, in which the internal etching pattern and infill ratio are specifically optimized as a function of the operating frequency and the desired EM performance. This engineered material platform is then exploited to co-design an advanced dual-function microwave system capable of performing both EH and quasi-UWB backscattering for indoor localization. Several previous two-port rectennas operating at both single frequency [91] and multi-band [92] have been presented for narrow-band SWIPT [93]. In [94], a combined UHF–UWB antenna is presented but it is not suitable for wearable applications because of its ungrounded nature and UHF and UWB are not cross-polarized.

The proposed solution overcomes these limitations by employing a thick, grounded, 3D-printed substrate that ensures high decoupling from the human body, while maintaining broadband radiation characteristics. To the best of the author's knowledge, this is the first demonstration of a 3D-printed dual-port cross-polarized wearable antenna capable of operating across both the UHF and UWB bands. In particular, the dual-port patch-like architecture features one port dedicated to receiving a multi-sine UHF signal for EH [95], while the second port backscatters a quasi-UWB signal passively generated from the intermodulation (IM) products of the multi-sine excitation [96]. This dual-function operation, which combines FF EH and passive information transfer within a single platform, represents a fully passive implementation of FF SWIPT for wearable applications.

The nonlinear rectifying and backscattering behaviors of the complete system are modeled through a combination of circuit-level and full-wave simulations, allowing the inclusion of all IM products within the UWB band without excessive computational cost [96]. The fabricated prototype was experimentally validated through a dedicated measurement campaign, confirming that the engineered PLA structure enables the realization of a compact and energy-autonomous platform capable of generating strong quasi-UWB signals for localization purposes.

An extended version of the system is schematically depicted in Fig. 2.3(b), illustrating the integration of the dual-mode rectenna with low-power control electronics, powered solely by the harvested energy, to support autonomous UWB communication and sensing.

2.2 PLA Characterization and Engineering

Among low-cost 3D-printable polymers, PLA represents a common bioplastic choice, characterized by $\varepsilon_r \approx 2.65$ and $tan(\delta) \approx 0.01$ at 1 MHz, with its frequency-dependent behavior reported up to 60 GHz [97]. In this

Thesis, PLA samples were fabricated using an Ultimaker 3 Extended 3D printer (minimum layer thickness: 20 μm, XY accuracy: 12.5 μm).

To verify the consistency of the material's EM properties under specific printing conditions and to compare them with literature data, the dielectric parameters of PLA were experimentally extracted using the T-resonator method, see Figs. 2.4. Two substrate thicknesses (0.5 mm and 2 mm) were investigated to ensure that the retrieved dielectric constant values remained consistent across different layer configurations.

The T-resonator approach allows the estimation of the dielectric constant (ε_r) and electrical conductivity (σ) by fabricating a resonator tuned for a target frequency and an initial guess of the effective dielectric constant (ε_{eff}). The resonator length L_{stub} = 31 mm, resulting in a first resonance at 1.5 GHz, is defined according to the closed form expression [77]:

$$L_{stub} = \frac{n \cdot c}{4 \cdot f_n \cdot \sqrt{\varepsilon_{eff}}}, \tag{2.1}$$

where, $n = 1$ is the resonance order, c the speed of light, f_n = 1.5 GHz (expressed in Hz in the formula) is the selected first order resonance frequency, and $\varepsilon_{eff} = 2.6$ is the initial estimate of the PLA effective dielectric constant (neglecting losses).

Each resonator consisted of a 50-Ω microstrip line with a quarter-wavelength open stub, manually realized using 35-μm adhesive copper. The S-parameters were measured with the Keysight N9952A FieldFox VNA and subsequently compared with full-wave CST MS simulations. The dielectric properties (ε_r, σ) were iteratively adjusted in simulation to achieve broadband agreement with the experimental S-parameter response.

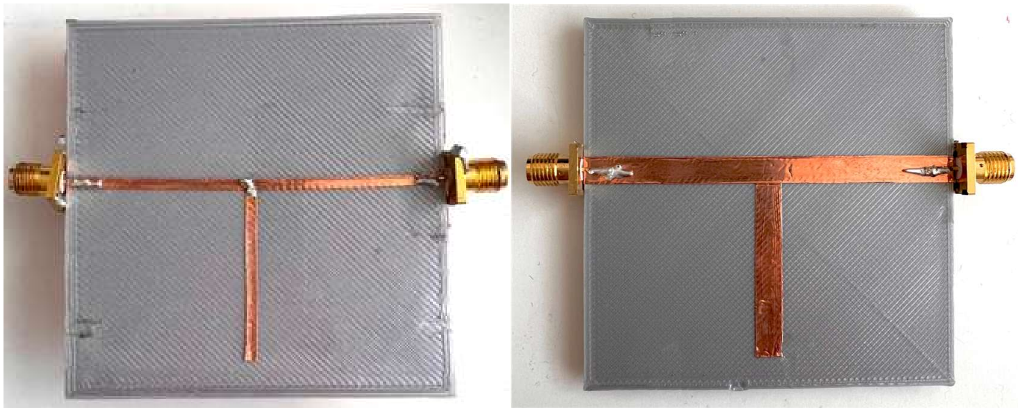

(a) (b)

Figure 2.4. Photographs of the fabricated T-resonators with adhesive copper on (a) 0.5 mm and (b) 2-mm-thick PLA samples. [26]. ©2024 IEEE

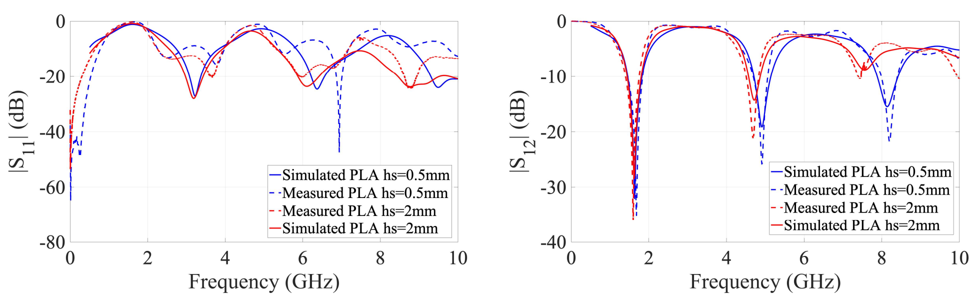

(a) (b)

Figure 2.5. Measured and simulated (a) reflection and (b) transmission coefficient magnitudes of the T-resonators of Figs. 2.4 on 2-mm-thick (red curves) and 0.5-mm-thick PLA (blue curves). [26]. ©2024 IEEE

The characterization procedure results are reported in Fig. 2.5(a) and (b), for the samples of Figs. 2.3. Table 2.1 reports the resulting dielectric properties derived for several frequencies: they are almost independent from the thickness, as confirmed in [97]. However, they show the dispersive behavior of the 3D printed PLA, and the loss tangent is excessive for exploiting PLA for high-performance RF circuits design.

TABLE 2.1

PLA EM CHARACTERIZATION RESULTS

Freq. (GHz)	ε'		ε''		$tan(\delta)$	
	0.5 mm	2 mm	0.5 mm	2 mm	0.5 mm	2 mm
2	2.65	2.64	0.05	0.05	0.019	0.019
5	2.64	2.66	0.08	0.08	0.03	0.03
7	2.65	2.7	0.095	0.13	0.036	0.048
10	2.68	2.76	0.13	0.13	0.048	0.047

To mitigate these limitations, several strategies have been proposed in the literature, as described in the previous paragraph [28], [29], [79]. Such approaches involve structural or topological optimization, such as embedding engineered air cavities or printing composite lattice structures, effectively reducing both the effective permittivity and dielectric losses. These composite or porous materials can improve antenna efficiency and bandwidth while maintaining the advantages of 3D printability and low cost. Nevertheless, such configurations introduce additional trade-offs: the reduced mechanical stability may cause deformation under bending or compression, resulting in detuning effects and unpredictable shifts of the resonant frequency.

Thus, to achieve a carefully balance between EM performance and structural integrity, in [27] original hybrid “sandwich-like” substrate architectures inspired by aerospace and automotive engineering have been proposed, featuring a patterned lightweight core (e.g., honeycomb, truss, or gyroid) enclosed between thin outer layers. These structures preserve high empty/fill ratios while maintaining flexural strength and minimizing dielectric loss.

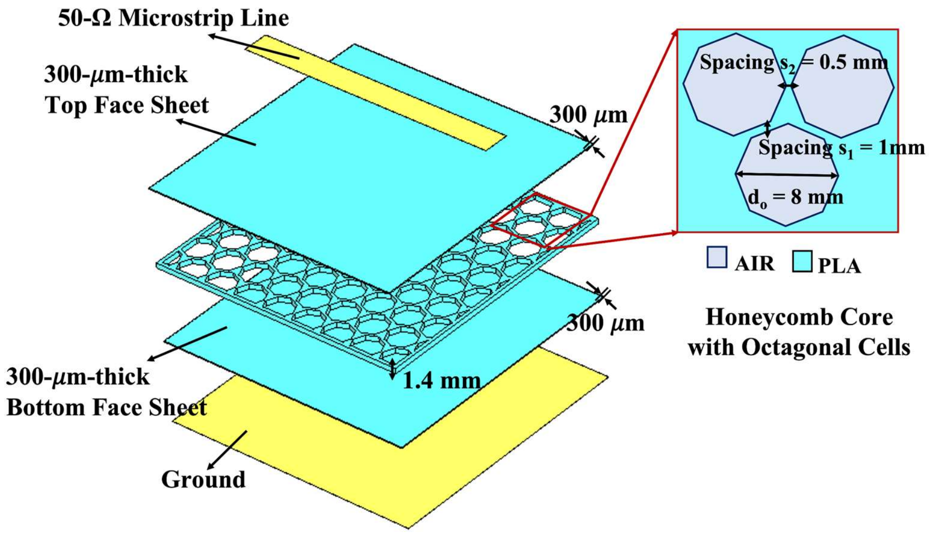

Figure 2.6. Exploded view of a microstrip transmission line realized on a PLA substrate engineered as a sandwich-like structure with a honeycomb core with octagonal cells. [26]. ©2024 IEEE

Such sandwich-like structure, illustrated in Fig. 2.6, where two 300-μm-thick PLA layers encapsulate a 1.4-mm-thick central honeycomb-like core composed of octagonal air-filled cells, is thoroughly analyzed from the EM point of view in this Paragraph.

The geometry of these cavities—specifically, the cell radius, wall thickness, and spacing—has been optimized to maximize the air-to-material ratio while maintaining mechanical strength and high EM (radiation) performance. For operation at 2.45 GHz, octagonal cells with 4-mm radius were found to provide an optimal compromise, yielding an air/PLA ratio of 52%/48%.

This mixture of air-PLA must be represented using effective EM parameters that account for the field propagating in both materials and the associated boundary conditions due to the material pattern. The effective dielectric properties of this composite medium were estimated using the homogenization theory of the Maxwell–Garnett mixing model. From [98], the constituent media and their volume fractions are used to predict an effective dielectric permittivity as follows:

$$\varepsilon_{eff} = \varepsilon_h + 3V_i\varepsilon_h\left(\frac{\varepsilon_i-\varepsilon_h}{\varepsilon_i+\varepsilon_h-2V_i(\varepsilon_i-\varepsilon_h)}\right), \qquad (2.2)$$

where ε_h and ε_i are the host and inclusion dielectric permittivities (with reference to Table 2.1: $\varepsilon_i = \varepsilon'$, $\varepsilon_h = 1$), respectively, and V_i is the inclusions' volume fraction. Obviously, when V_i tends to 0%, $\varepsilon_{eff} \simeq \varepsilon_h$, and when V_i tends to 100%, $\varepsilon_{eff} \simeq \varepsilon_i$. The higher the operating frequency, the higher the accuracy required in selecting the PLA inclusions' dimensions, which may cause anisotropy. For this reason, the approximate model of ε_{eff} retrieved through (2.2) is valid only in the long-wavelength limit, where the static and quasi-static conditions are satisfied. Thus, inclusions' size lower than the smallest wavelength must be selected: as a rule of thumb, it must not exceed one tenth of the wavelength in the effective medium. In this way, (2.2) may offer a useful initial guess of the effective dielectric constant of the medium with inclusions; indeed, from (2.2) an equivalent effective medium with $\varepsilon_{eff} = 1.62$ is derived for an average spacing $[(s_1 + s_2)/2] = 0.75$ mm (see Fig. 2.6) among adjacent octagons. This has been obtained using the PLA relative dielectric permittivity $\varepsilon_i = 2.65$ evaluated at the nominal frequency of 2.45 GHz as shown in Table 2.1, and $\varepsilon_h = 1$, dielectric permittivity of the air.

This result is in good agreement with full-wave simulations of the reference T-resonators, with the actual inclusions' shapes accounted for, resulting in a complex effective permittivity of $\varepsilon'_{eff} \approx 1.8$, $\varepsilon''_{eff} \approx 0.035$ at the nominal frequency of 2.45 GHz.

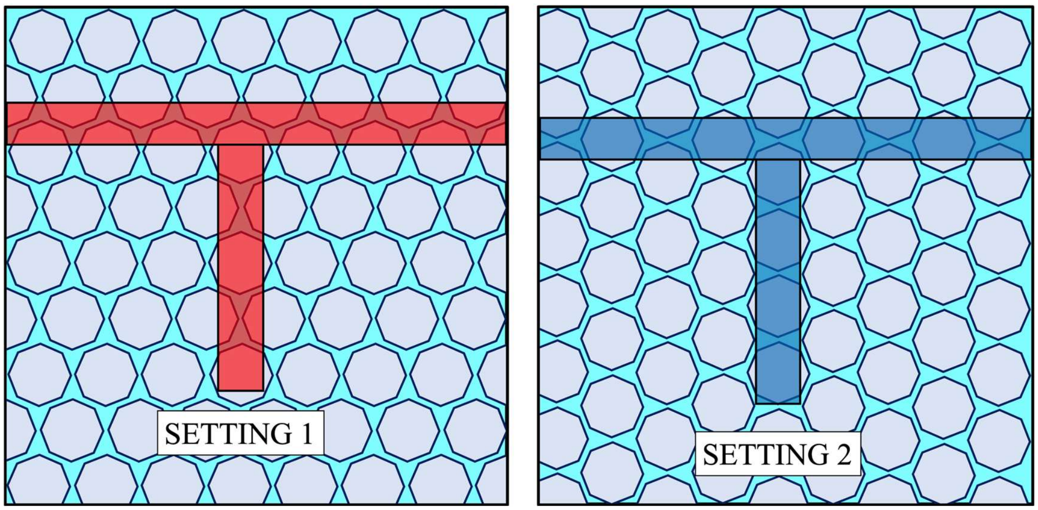

(a)

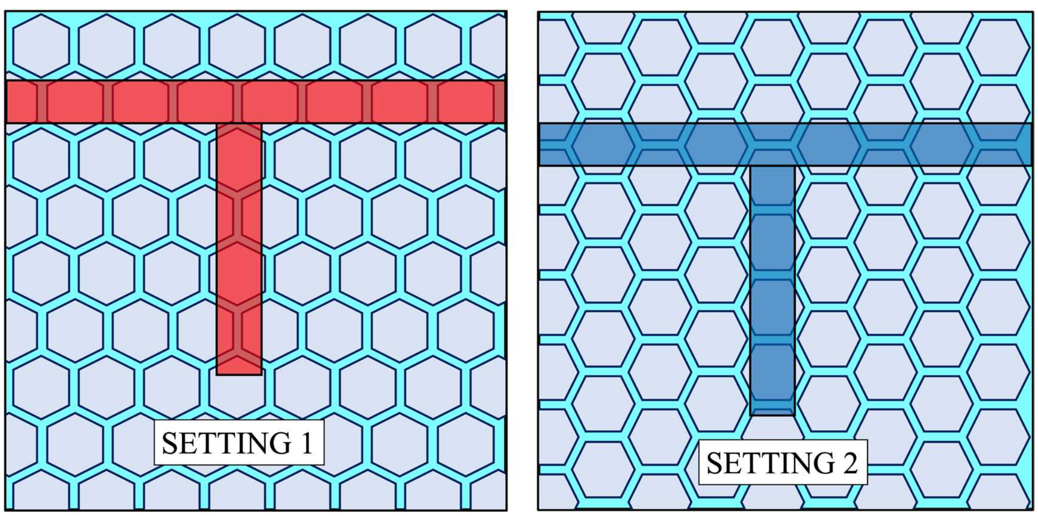

(b)

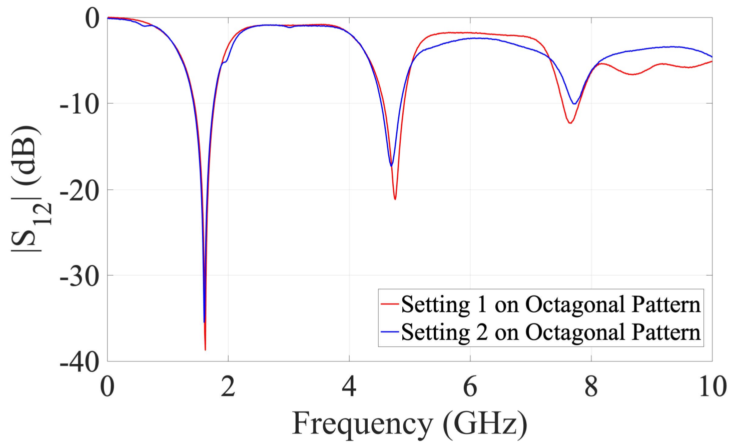

(c)

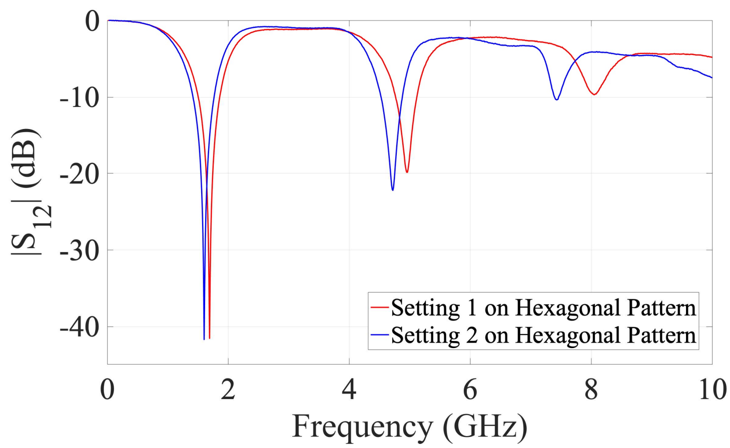

(d)

Figure 2.7. Resonator's layout positioning on top of the core with (a) octagonal and (b) hexagonal cells patterns; magnitude of the measured transmission coefficients with (c) octagonal and (d) hexagonal cells patterns. [26]. ©2024 IEEE

Interestingly, the adoption of octagonal rather than hexagonal patterns improves the effective isotropy of the substrate. Experimental verification using T-resonators differently placed over both geometries (having the same empty/full ratio, hence the same ε_{eff}), as represented in Figs. 2.7(a) and (b), demonstrated that octagonal lattices preserve stable resonance frequencies across different orientations, whereas hexagonal ones exhibit notable frequency shifts depending on the T-resonator placement, especially at higher harmonics, as reported by the corresponding measured transmission coefficients in Figs. 2.7(c) and (d). Similar results have been obtained for other orientations of the microstrip lines, confirming the superior "effective" uniformity of the octagonal pattern.

2.3 Circuit-Level EM Nonlinear Co-Design of the UHF-UWB Tag

2.3.1 Dual-Port Antenna Design

The previously described 3D-printed engineered-PLA sandwich structure was adopted as the substrate for the design of a dual-port antenna, illustrated in Fig. 2.8.

The antenna integrates two ports: the input port (P1), positioned along the lower edge and vertically oriented, is dedicated to the reception of the multi-sine vertically-polarized excitation signal at UHF frequencies; the output port (P2), located on the right-hand side and horizontally oriented, is responsible for the backscattering of the passively generated horizontally-polarized quasi-UWB pulse. The positions and orientations of P1 and P2 were carefully optimized to simultaneously ensure cross-polarization and decoupling between the UHF and UWB ports.

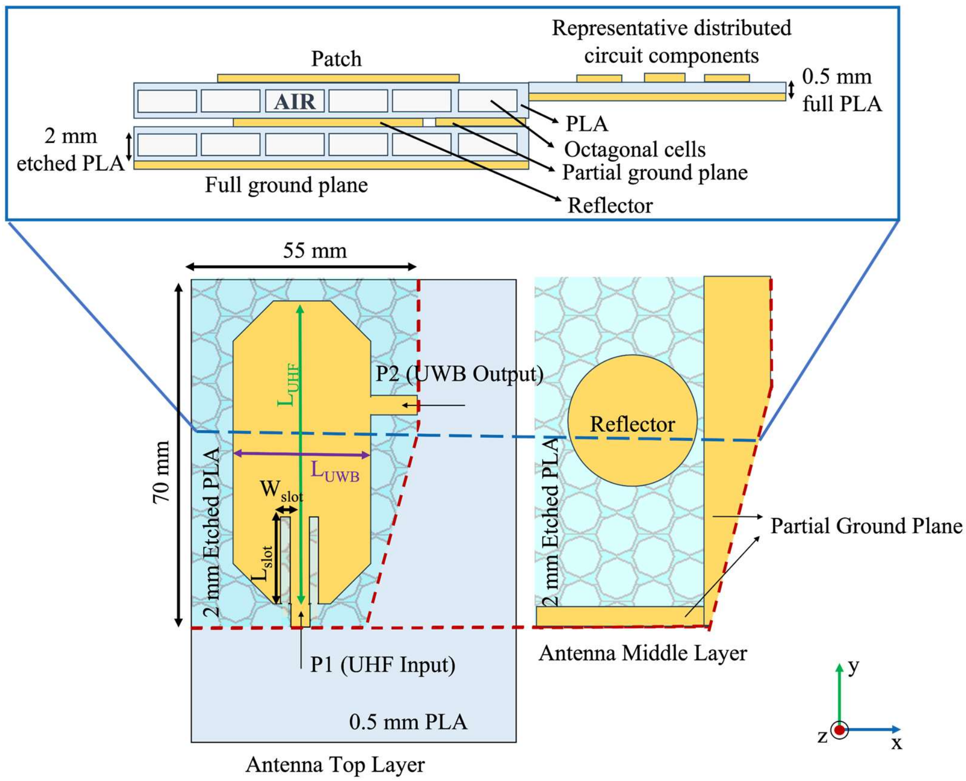

Figure 2.8. Dual-port antenna layout: cross-section, showing the multilayer structure (top), and front views of the top and middle layers (bottom). [26]. ©2024 IEEE

Compared with the dual-antenna configuration proposed in [27], this unified two-port layout achieves a significant footprint reduction and enhanced overall system performance.

Leveraging the flexibility of AM, the antenna was realized on a multilayer structure composed of two PLA layers engineered as described in the previous paragraph (each 2-mm-thick and 70 × 55 mm^2 in size), which are sandwiched together. The bottom-right corner of the substrate is trimmed to accommodate the rectifier circuitry, implemented on a 0.5-mm-thick full PLA extension of the upper layer.

As depicted in Fig. 2.8 (top), the multilayer configuration serves a dual purpose: it ensures wideband behavior for the UWB port, while also improving mechanical robustness and wearability thanks to the bottom ground plane, which effectively isolates the antenna from the surrounding environment [99]. The upper layer hosts the patch metallization, designed with a stretched octagonal shape to achieve broadband performance. The vertical length of the patch, $L_{UHF} = 52$ mm, corresponds to approximately half a wavelength within the effective 3D-printed medium at 2.45 GHz, thus ensuring efficient RF power reception at UHF. Two inset slots (length $L_{slot} =$ 15 mm, width $W_{slot} = 1.5$ mm) were included to match the input impedance of the antenna to the 50-Ω feeding line.

The shorter horizontal dimension, $L_{UWB} = 25$ mm, was optimized for operation in the UWB band. Wideband performance is further enhanced by a circular reflector (radius = 10 mm) integrated in the layer beneath the patch, whose geometry and placement extend the bandwidth up to the fourth harmonic of the highest fundamental UHF tone (2.47 GHz), enabling effective backscattering of the quasi-UWB signal through port P2 [96], as will be detailed in Paragraph 2.3.3.

To maintain compact feeding line widths (5 mm), partial ground planes were introduced in the intermediate layer, both vertically and horizontally. Finally, a full ground plane was incorporated at the bottom of the second honeycomb layer, making the tag completely wearable and electromagnetically decoupled from any additional underlying materials.

Further improvement in port isolation was obtained by shifting port P2 slightly upward toward the top edge of the patch.

2.3.2 Numerical and Experimental Characterization of the Antenna

The performance of the proposed dual-port antenna was evaluated through full-wave EM simulations carried out in CST MS over an extended frequency range up to 10 GHz. To validate the simulated results, a prototype of the antenna was fabricated on the 3D-printed 2-mm-thick PLA sandwich substrate described earlier (see Fig. 2.8), and experimentally characterized. The comparison between simulated and measured reflection coefficients at the UHF and UWB ports is presented in Figs. 2.9(a) and 2.9(b), respectively. As shown, the reflection coefficient at the UWB port exhibits slight resonance shifts in the lower-frequency region, which, however, does not affect system performance since this portion of the spectrum is not exploited for backscattering and is filtered out. In the higher-frequency range, corresponding to the harmonics used for the quasi-UWB pulse generation, a close agreement between simulations and measurements is achieved. A similar level of consistency is observed in the measured and simulated transmission coefficients between the two ports, reported in Fig. 2.9(c).

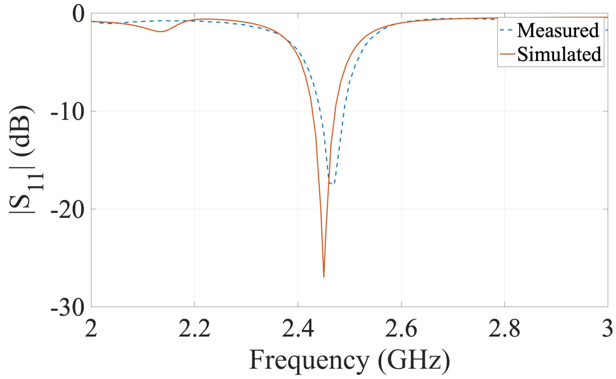

(a)

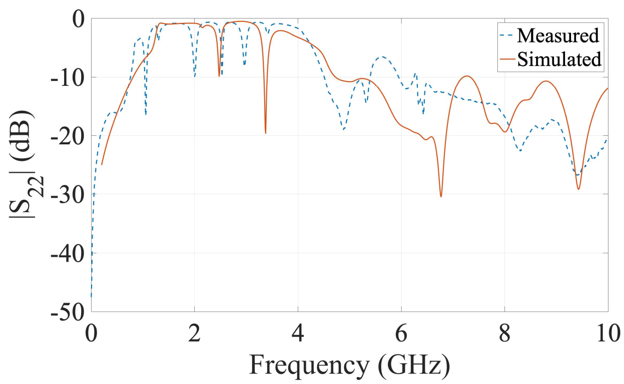

(b)

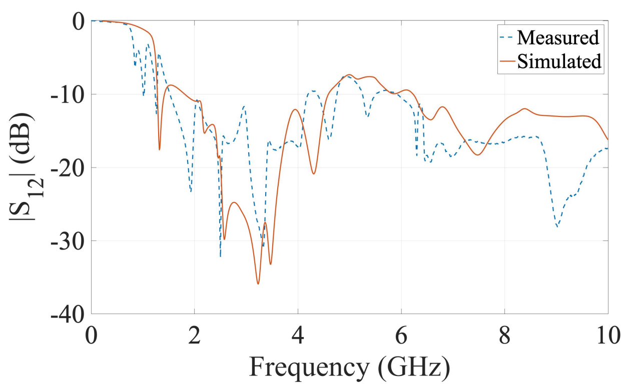

(c)

Figure 2.9. Reflection coefficient versus frequency at (a) UHF and (b) UWB antenna ports. (c) Transmission coefficient between the two ports. [26]. ©2024 IEEE

From these results, it can be noted that the fabricated prototype resonates at 2.47 GHz, in excellent agreement with the simulated 2.45 GHz. The measured UWB response demonstrates a −10 dB impedance bandwidth extending from 4.5 GHz to 10 GHz, confirming the broadband behavior of the antenna.

The simulated radiation characteristics are summarized in Figs. 2.10. The UHF antenna pattern, displayed in Fig. 2.10(a) for the φ = 0° azimuthal plane, shows a broadside main lobe with a maximum gain G_{UHF} = 4.76 dBi. The corresponding radiation patterns of the UWB antenna, reported in Fig. 2.10(b) for the φ = 90° plane, were evaluated at the second, third, and fourth harmonics, yielding maximum gains of $G_{UWB,II}$ = 6.24 dBi, $G_{UWB,III}$ = 4 dBi, and $G_{UWB,IV}$ = 8.62 dBi, respectively.

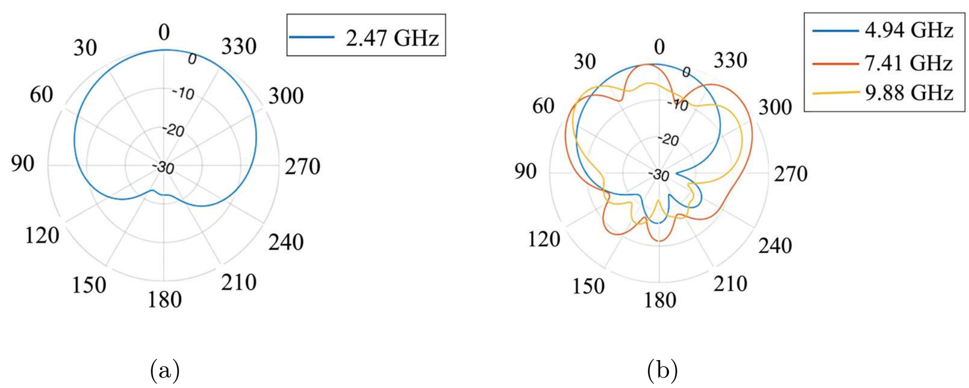

Figure 2.10. Normalized logarithmic polar plots in (a) ϕ = 0° plane at the UHF frequency and (b) ϕ = 90° plane in the UWB band at the II, III and IV harmonics of 2.47 GHz, namely 4.94, 7.41, and 9.88 GHz. [26]. ©2024 IEEE

The designed cross-polarization between the UHF and UWB ports is also confirmed by the simulation results. The polarization properties, including the vertical (E_Y) and horizontal (E_x) electric field components and the corresponding axial ratio (AR), are summarized in Table 2.2. Analysis of these data indicates that the antenna exhibits vertical polarization at the fundamental UHF frequency, while maintaining horizontal polarization across the UWB band, thereby validating the intended dual-polarized behavior.

TABLE 2.2

AR and E-FIELD COMPONENTS IN THE MAXIMUM DIRECTION OF RADIATION

Antenna Port	Freq. (GHz)	AR (dB)	E_Y (V/m)	E_X (V/m)
UHF	2.47	21.2	8.88	1.23
UWB	2.47	27.6	0.4	6.2
	4.94	39.1	0.11	10.2
	7.41	28.7	0.33	6.78
	9.88	9.6	4.63	7.03

2.3.3 UHF-UWB Tag Design: Nonlinear Design of a Simultaneous UHF-to-DC and UHF-to-UWB band

With the aim of developing a SWIPT tag based on a multi-sine excitation, a dual-port nonlinear rectifier has been designed and realized. This sub-system pursues a twofold objective: first, to harvest RF energy from a multi-sine input signal and convert it into DC power for supplying a low-power MCU and/or sensor; second, to modulate the passively generated quasi-UWB signal to be backscattered for localization purposes.

The multi-sine excitation was modeled following the approach proposed in [96], for efficient nonlinear simulations, where each tone is represented as a higher harmonic of a common fundamental frequency—here chosen as $f_0 = 1$ MHz. Eight tones centered around 2.47 GHz were adopted, leading to an excitation signal expressed as:

$$x(t) = \sum_{i=K_1}^{K_T} x_i \cos\left(2\pi i f_0 t + \varphi_i\right), \tag{2.3}$$

where, x_i and φ_i denote the amplitude and phase of the i^th tone, and $K_1 = 2467$, $K_T = 2474$ are the integer indices corresponding to the tones range. The selected tone spacing and number of tones were optimized based on the measured resonance and bandwidth of the antenna system.

The circuit-level simulations were carried out using Keysight ADS, leveraging an advanced formulation of the Harmonic Balance (HB) method capable of handling multi-tone excitations with a high number of frequency components. By representing each tone as a harmonic of the base frequency f_0, the multi-tone simulation is effectively reduced to a single-tone problem, allowing efficient optimization of amplitude, phase, and tone distribution. This formulation produces a dense harmonic spectrum (in the order of tens of thousands of harmonics) while ensuring faster and more accurate convergence compared to traditional IM analyses.

The center tone at 2.47 GHz, the frequency spacing, and the number of tones have been selected based on the measured antenna resonance and bandwidth.

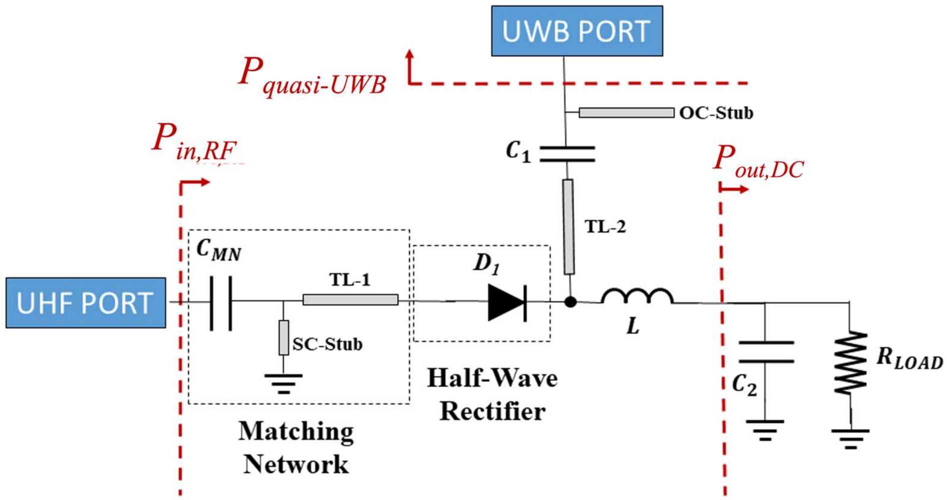

(a)

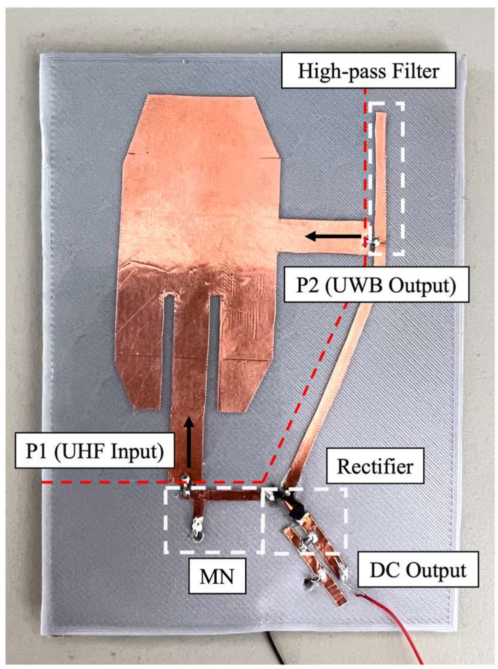

(b)

Figure 2.11. (a) Circuit schematic of the designed dual-mode rectifier. (b) Photograph of the system prototype (top view) with the two-port antenna connected to the rectifier. UHF and UWB ports are also highlighted. [26]. ©2024 IEEE

The schematic of the rectifier and the corresponding fabricated prototype, which integrates the dual-port antenna, are shown in Fig. 2.11(a) and Fig. 2.11(b). The circuit is based on a single Schottky diode (Skyworks SMS7630-079LF), chosen for its low threshold voltage and fast switching speed, and embedded within a carefully designed linear sub-network that ensures efficient impedance matching and harmonic management.

At the input stage, the single-stub matching network (MN in Fig. 2.11(b)) connected to the UHF port was optimized to maximize power transfer from the antenna to the diode. It consists of a short-circuited microstrip stub *SC-Stub* and a 50-Ω transmission line section *TL-1*, with dimensions of 4.42 mm and 11.6 mm in length, respectively, both 1.3-mm-wide, complemented by a 0.9 pF DC-blocking capacitor, C_{MN}. This configuration was selected to achieve the desired input impedance profile while maintaining compactness and manufacturability.

Downstream of the diode, the output network is structured to manage the dual functionality of the rectifier—namely, DC power extraction and harmonic routing. To this end, the output is divided into two complementary branches. The first is a low-pass path responsible for collecting the rectified DC component. It includes a high-Q inductor L = 1100 nH (506WLS by American Technical Ceramics (ATC)) and a capacitor C_2 = 560 pF, which together form a smoothing filter connected to the optimal resistive load R_{LOAD} = 790 Ω. The second branch performs a high-pass function, selectively guiding the higher-order harmonics generated by the diode toward the UWB antenna port. This path is implemented with a 50-Ω transmission line *TL-2* (44.3 mm long, 1.3 mm wide), followed by an open-circuited stub *OC-Stub* (20.8 mm long, 1.3 mm wide) and another capacitor C_1 = 0.9 pF DC-blocking. Through this dual-branch design, the circuit enables concurrent EH and data transmission within a single compact rectifier module.

All these circuit elements were used as optimization variables in a nonlinear multi-objective design framework combining EM and circuit-level simulations [86]. The optimization simultaneously targeted: (i) maximization of the RF-to-DC PCE, (ii) maximization of the power spectral lines near the multi-sine higher harmonics (II, III, and IV), and (iii) minimization of the return loss at the antenna ports and of the undesired near-carrier components falling in the multi-tone fundamental frequencies.

Two different phase distributions were analyzed for the multi-sine excitation — constant and parabolic — the latter defined as:

$$\phi_k = \left(\frac{k^2 - 1}{N}\right)\pi, \qquad k = 1, \ldots, N \tag{2.4}$$

where, $N = 8$ is the number of tones.

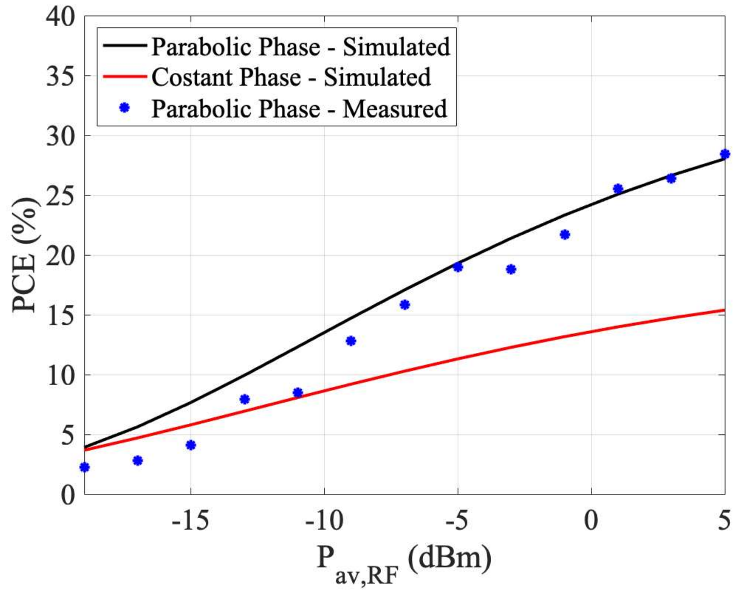

Figure 2.12. PCE as a function of the available RF power $P_{av,RF}$ equally distributed over the eight tones for two different phase distributions: with the tones sharing the same phase (simulated), and with a parabolic phase distribution (simulated and measured). [26]. ©2024 IEEE

Nonlinear simulations of the rectenna demonstrated superior efficiency for the parabolic phase configuration across the input power range of interest (see Fig. 2.12), which was therefore selected for the final implementation. The two excitations obviously share the same peak-to-average power ratio (PAPR).

The overall RF-to-DC PCE is evaluated as:

$$PCE(\%) = \frac{P_{out,DC}}{P_{av,RF}} \cdot 100 \tag{2.5}$$

where $P_{out,DC}$ is the rectified DC power and $P_{av,RF}$ is the available RF power at the rectifier input, which inherently accounts for the antenna efficiency [100].

By applying the EM/nonlinear co-design methodology, the Effective Isotropic Radiated Power (EIRP) of the generated quasi-UWB signal was evaluated. For a multi-sine input power of -15 dBm, the resulting EIRP remains below -41.3 dBm/MHz — in compliance with Federal Communication Commission (FCC) spectral limits — considering the UWB antenna gains of 6.24, 4, and 8.62 dBi at the second, third, and fourth harmonics, respectively.

The simulated spectral content at the UWB antenna port for $P_{av,RF} = -15$ dBm is shown in Figs. 2.13. As expected, the filter at the UWB output effectively suppresses the spectral components near the first harmonic (Fig. 2.13(a)), which are not part of the backscattered quasi-UWB signal, while maintaining strong harmonic components near the higher orders used for communication.

As shown by these plots, the amplitudes of the harmonic content in these frequency windows are sufficient for generating the desired quasi-UWB signal but negligible contributions to be recycled by the harvester. Conversely, the stronger harmonics located near the fundamental tones are reflected back from the UWB port to the rectifier through the high-pass network, allowing their reuse and contributing to an increased PCE.

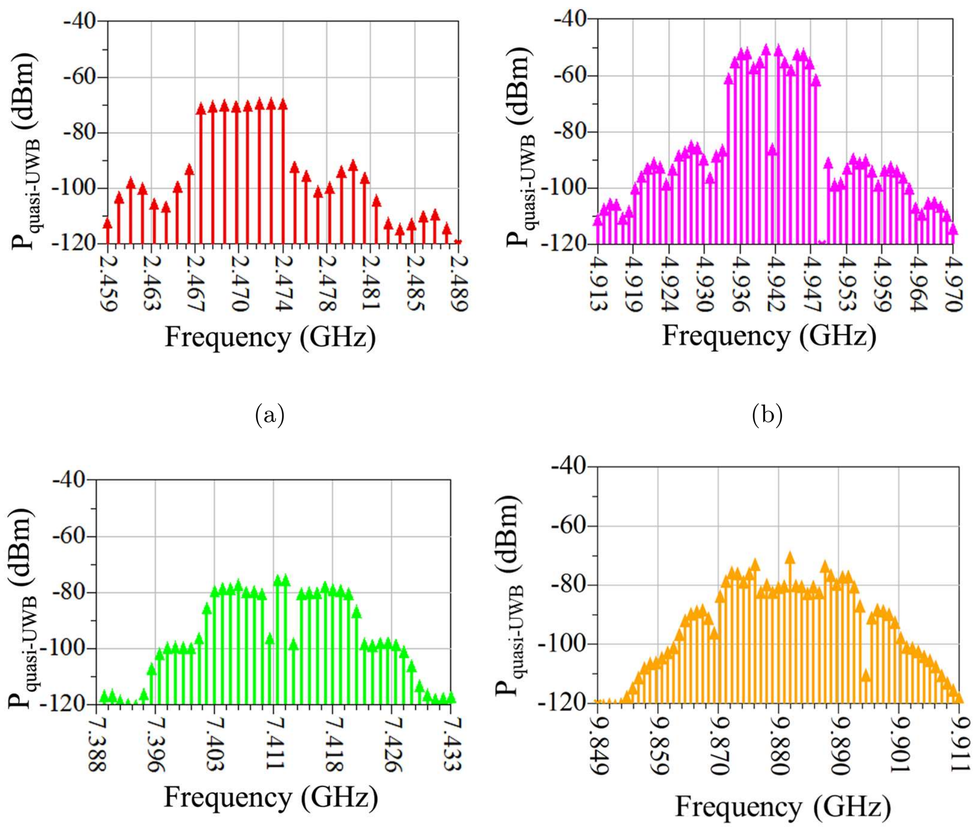

(a) (b)

(c) (d)

Figure 2.13. Predicted power spectral lines at the antenna UWB port near (a) first, (b) second, (c) third, and (d) fourth harmonics of the excitation signals, when the total available power is $P_{av,RF} = -15$ dBm. [26]. ©2024 IEEE

Figures 2.14(a) and (b) report the time-domain waveforms at the input UHF port and the output UWB port, with corresponding PAPRs of 8.36 dB and 8.19 dB, respectively. As expected, the output waveform exhibits a slightly altered shape compared to the input excitation, due to the rectifier's nonlinear response. This modified waveform constitutes the quasi-UWB signal, which is subsequently backscattered by the antenna to realize the communication function of the fully passive SWIPT tag.

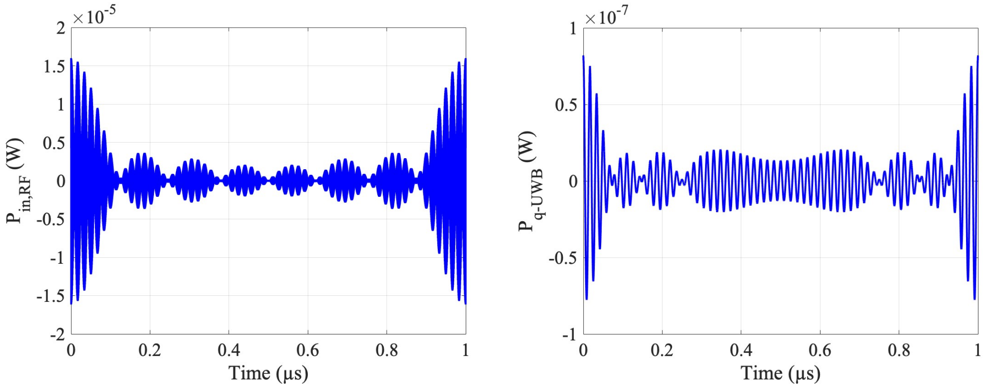

(a) (b)

Figure 2.14. Simulated power waveforms generated (a) at the UHF port ($P_{av,RF} = -15$ dBm) and (b) at the UWB port. [26]. ©2024 IEEE

2.4 UHF-UWB Tag Experimental Characterization

2.4.1 UHF-to-DC Energy Power Conversion

To experimentally validate the simulation results discussed in Paragraph 2.3, a measurement campaign was carried out focusing on the EH performance of the proposed system. The experimental setup, illustrated in

Fig. 2.15, reproduces the complete wireless link. On the TX side, a standalone UHF antenna is connected to a Tektronix AWG7122C arbitrary waveform generator, which provides the multi-sine excitation signal radiated toward the RX. On the RX side, the dual-port rectenna prototype is employed, and the resulting DC output power is measured to assess the overall rectification efficiency. The measured PCE, computed according to (2.5), is reported in Fig. 2.12 together with the simulated results, as a function of the input RF power $P_{av,RF}$, varying from -19 dBm to 5 dBm.

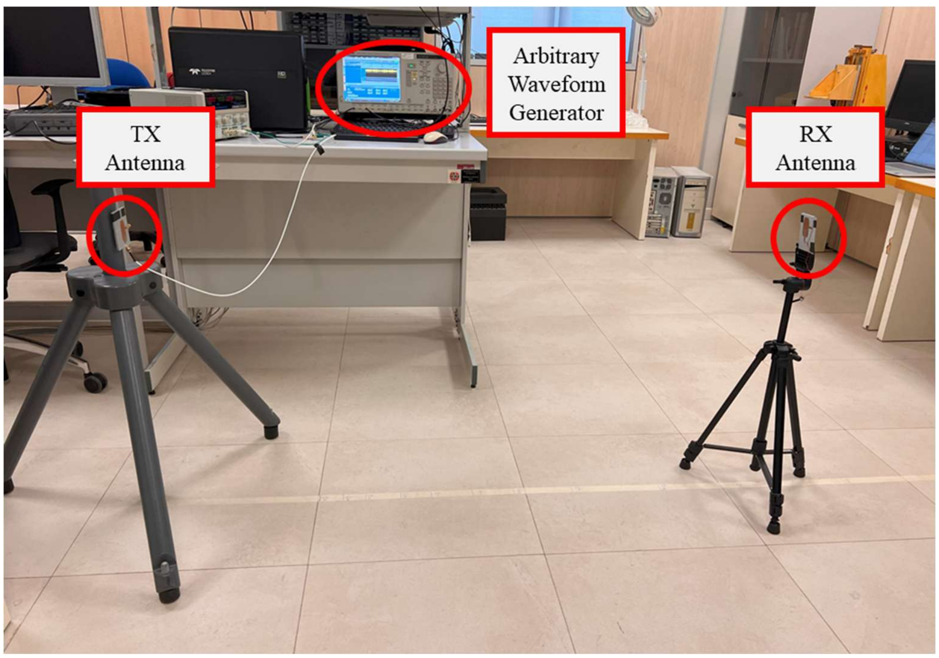

Figure 2.15. Measurement setup for EH validation measurements, showing the TX antenna connected to the arbitrary waveform generator, and the RX antenna. [26]. ©2024 IEEE

2.4.2 UHF-to-Quasi-UWB Signal Generation

A second measurement campaign was carried out to characterize the quasi-UWB signal generated by the nonlinear behavior of the rectifier and backscattered by the antenna. In this setup, the multi-tone generator transmitted a total power of 20.7 dBm, while the transmitting UHF antenna provided a gain of 4.76 dBi. Under these conditions, the available power at the rectenna's UHF port was $P_{av,RF} = -15\text{dBm}$, a value intentionally kept low to ensure that the backscattered signal remained compliant with the FCC UWB emission mask.

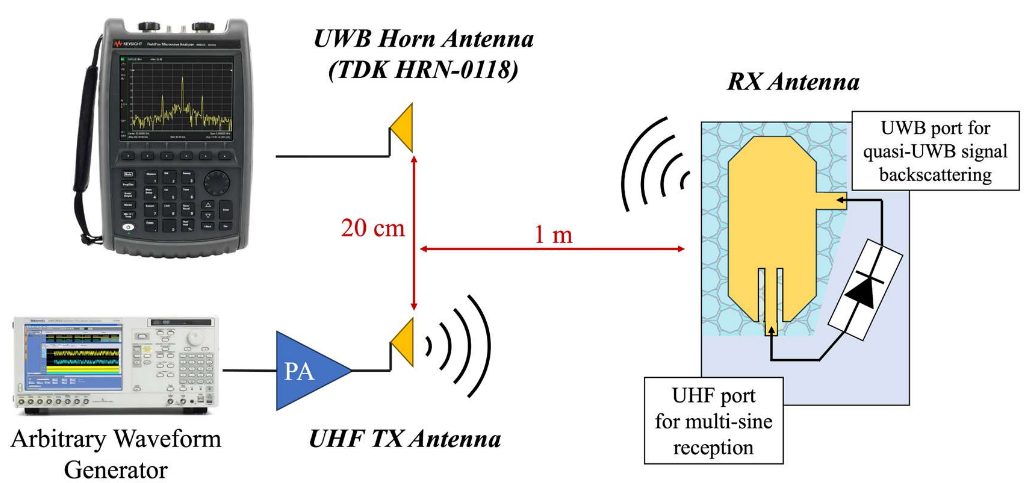

Figure 2.16. Schematic view of the setup for measuring the backscattered quasi-UWB signal. [26]. ©2024 IEEE

The experimental configuration, illustrated in Fig. 2.16, was adapted from the previous setup shown in Fig. 2.15. A horizontally polarized UWB horn antenna (TDK HRN-0118) was employed to detect the quasi-UWB signal re-radiated by the two-port rectenna, whose UWB emission was co-polarized with the horn. The horn was positioned 20 cm above the antenna transmitting the multi-sine excitation to effectively capture the backscattered components.

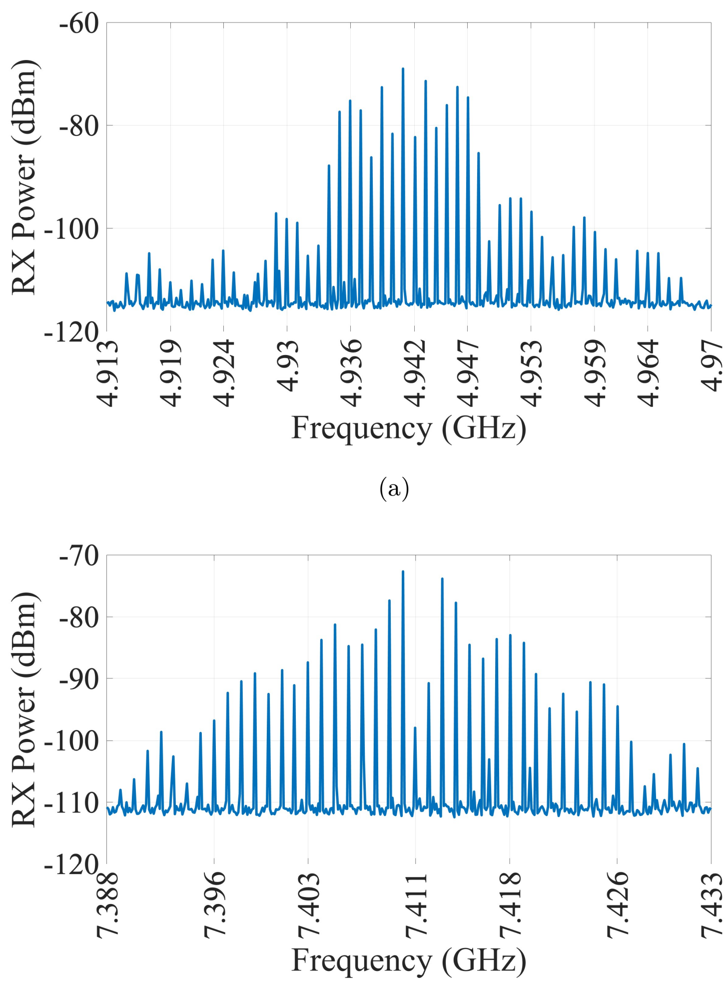

(b)

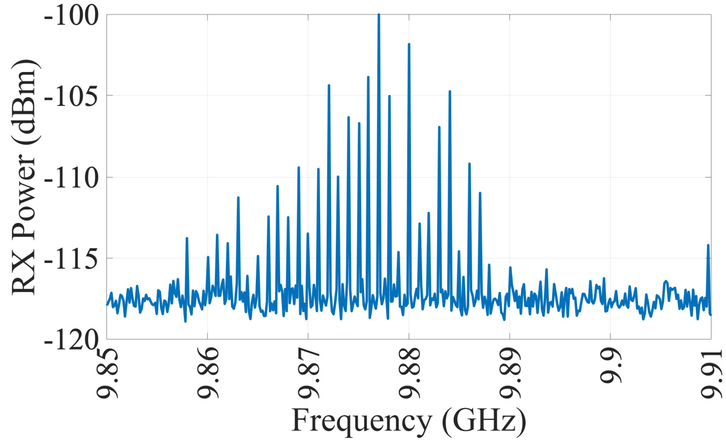

(c)

Figure 2.17. Measured power spectral lines backscattered by the rectenna and received by the horn associated to the quasi-UWB backscattered signal (total input power $P_{av,RF}$ of -15 dBm), around (a) second, (b) third, and (c) fourth harmonics. [26]. ©2024 IEEE

The measured spectra, reported in Figs. 2.17, show the power lines corresponding to the frequency windows around the second, third, and fourth harmonics of the transmitted multi-sine signal, as received by the horn antenna and recorded with a Keysight N9952A FieldFox analyzer (RBW = 3 kHz). The spectral components around the fourth harmonic were found to be below the minimum detectable level required to contribute meaningfully to the quasi-UWB signal. The results exhibit strong agreement with the predicted spectra in Fig. 2.13, both in terms of shape and relative power levels, confirming the reliability of the EM/nonlinear co-design methodology adopted in this work.

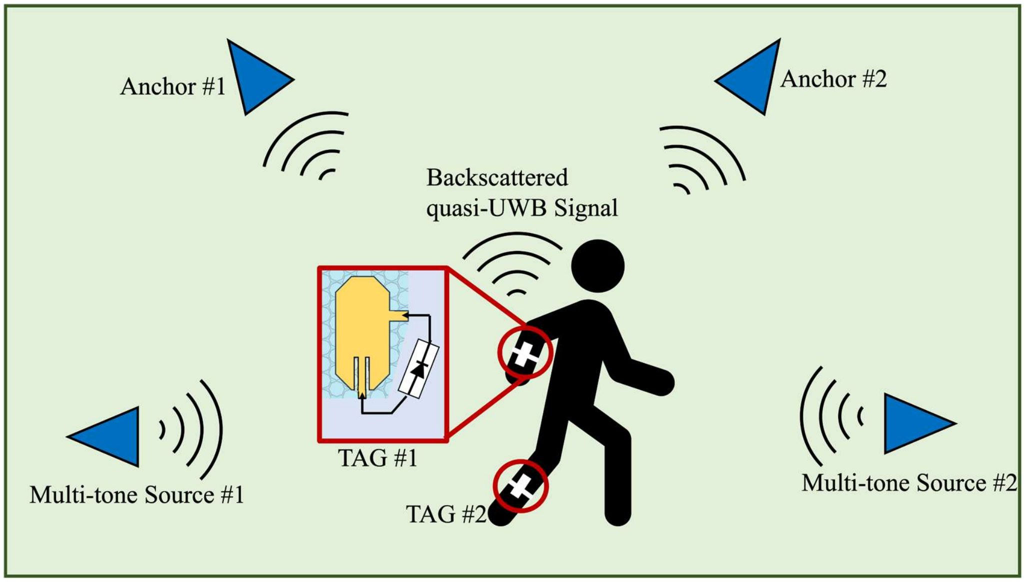

Figure 2.18. Envisioned scenario for a practical localization application with single/multiple multi-tone sources and anchor nodes that are placed around an indoor environment for the reception of the backscattered quasi-UWB signals. [26]. ©2024 IEEE

A possible application scenario of the proposed energy-autonomous localization system is schematically illustrated in Fig. 2.18. As detailed in [96], this architecture is particularly suitable for indoor localization, where a network of anchor nodes can determine the position of the tag by receiving its backscattered quasi-UWB signal. The harvested DC power is sufficient to enable modulation of the UWB signal and to supply a low-power inertial measurement unit (IMU) for monitoring user movement or activity.

For instance, with an available RF power of $P_{av,RF} = -15$dBm, the rectenna delivers a DC output of $P_{DC} = 12.5$ µW, which can sustain the dynamic switching and biasing operations of a UWB switch such as the Skyworks SKY59608-711LF, requiring a bias voltage $V_{BIAS} = 1.8$–3.3 V and supply current $I_S = 5$ µA. Moreover, these power levels are adequate to meet the energy demands of a low-power MCU, a LoRa transceiver, and a three-axis accelerometer operating at 400 samples/s [101]. In particular, considering the STM32L476RE MCU and the Semtech SX1280 LoRa transceiver, and assuming a power management unit efficiency of 50%, sufficient energy can be stored to perform periodic sensing and data transmission of acceleration measurements approximately every 160 seconds.

2.5 Conclusion

In this Chapter, a fully 3D-printed rectenna system fabricated on a low-cost engineered-PLA substrate has been presented, combining in a single compact platform the functionalities of RF EH and quasi-UWB backscattering. The work demonstrates how AM and EM co-design can be effectively merged to realize energy-autonomous wireless systems.

A thorough EM characterization of the 3D-printed PLA material was first performed, including the implementation of an engineered octagonal infill pattern to enhance its dielectric performance. The optimized structure, featuring a suitable fill ratio and cell geometry, led to improved effective permittivity and reduced losses, thereby enabling high-performance antenna operation, while also maintaining mechanical robustness.

Based on this engineered substrate, a dual-port patch antenna was designed with orthogonal UHF and UWB ports to achieve cross-polarized radiation and wideband response. Both simulations and measurements confirmed excellent agreement, with resonances around 2.47 GHz and a UWB bandwidth extending from 4.5 GHz to 10 GHz.

The antenna was integrated with a single-diode rectifier optimized under multi-sine excitation using a combined EM/nonlinear co-design strategy. This approach enabled the simultaneous optimization of impedance matching, harmonic generation, and RF-to-dc PCE, accounting for the dispersive behavior of the antenna. Measurements confirmed that for a -15 dBm available RF power, the rectenna achieves the predicted PCE values and generates a quasi-UWB signal compliant with FCC emission limits (EIRP < -41.3 dBm/MHz).

Finally, the experimental results demonstrated that the harvested power is sufficient to sustain low-power electronics such as MCUs, LoRa transceivers, and inertial sensors, paving the way for self-powered localization and sensing applications. Overall, the proposed PLA-based, 3D-printed rectenna represents a cost-effective, flexible, and scalable solution for next-generation wearable and implantable SWIPT systems.

Chapter 3. A Dual-Band Tri-Port Wearable Tag for Indoor SWIPT Enabled by Hybrid Near-/Far-Field Energy Harvesting

This Chapter is based on the following articles:

[36] G. Paolini, F. Benassi, G. Battistini, E. Augello, D. Masotti, and A. Costanzo, "A Tri-Port Wearable Tag for Indoor Communication with Power Delivery through Near-Field and Far-Field Energy Harvesting," in *Proceedings of the 2025 IEEE International Conference on RFID Technology and Applications – RFID-TA 2025*, Valence, France, Oct. 2025.

[35] G. Paolini, G. Battistini, D. Masotti, S. Scanzio, G. Cena, and A. Costanzo, "Design of a Dual-Band Tri-Port Tag for Near-Field Energy Harvesting and Far-Field SWIPT," in *Proceedings of the 7th URSI Asia-Pacific RadioScience Conference – AP-RASC 2025*, Gent, Belgium: URSI – International Union of Radio Science, 2025.

These works were partly funded by the European Union (EU) under the NextGenerationEU programme, the Italian Ministry of Enterprises and

Made in Italy (MIMIT), and the University of Bologna within the framework of the "AlmaValue for RR" project "WirelessLOC" (CUP: C38H23000710002), and partly by the EU (NextGenerationEU) under the Italian National Recovery and Resilience Plan (NRRP), Mission 4, Component 2, Investment 1.3 (CUP: J33C22002880001), partnership on "Telecommunications of the Future" (PE00000001 – program "RESTART").

3.1 Introduction

In the previous Chapter, a dual-port 3D-printed rectenna was designed and experimentally validated as a cost-effective, high-performance FF SWIPT wearable tag, enabling fully passive, self-powered localization and sensing. Building upon these results, the present Chapter extends this concept toward a more comprehensive framework for simultaneous wireless power and data transfer tailored to WBANs.

Simultaneous Wireless Information and Power Transfer (SWIPT) systems address the critical challenge of energy-constrained wireless devices by integrating WPT and WIT within a unified framework, transmitting energy and data concurrently through the same RF channel. This dual functionality not only reduces hardware complexity and device footprint but also enhances overall system integration, making SWIPT particularly appealing for WBANs, where wearable nodes must operate reliably under strict size, power, and mobility constraints.

However, most existing SWIPT implementations, such as that presented in Chapter 2, rely on a single power transfer mechanism, either NF or FF, limiting flexibility and efficiency in dynamic environments [32], [34].

To address these challenge, the work presented in this Chapter, based on [35], [36], introduces a novel hybrid NF/FF SWIPT architecture that seamlessly integrates both NF and FF WPT modalities within a unified, compact, and wearable RFID-based platform. The proposed system combines a 13.56 MHz inductive coil for efficient NF power harvesting with a 2.4 GHz cross-polarized antenna for FF energy acquisition and bidirectional data communication. By exploiting this hybrid configuration, the system dynamically adapts to varying RF conditions, ensuring uninterrupted functionality and improved robustness across diverse operational contexts, ranging from industrial and automotive monitoring to healthcare and smart environments.

3.2 Design of the Dual-Band Tri-Port Flexible Tag

3.2.1 Dual-Port UHF Antenna Design

The dual-port SWIPT patch antenna is designed as a dual-polarized radiating element capable of both wireless power reception and data communication. The communication functionality is intended to interface with the 50-Ω input/output port of a transceiver, while the EH functionality operates in the 2.4 GHz ISM band, sharing a common RF ground plane.

To ensure wearability and conformability to curved surfaces, the antenna is implemented on a flexible Rogers RO3003 substrate ($\varepsilon_r = 3$, $tan(\delta) = 0.001$, thickness 0.76 mm).

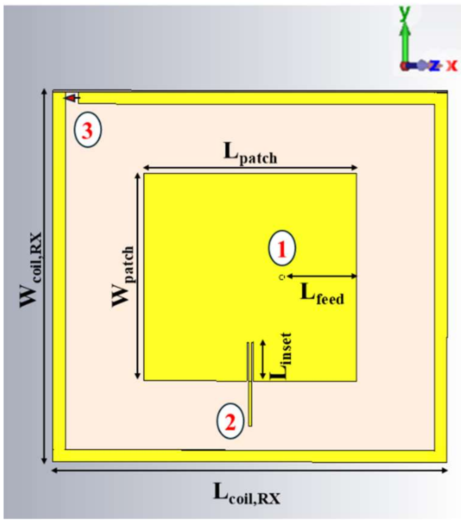

(a)

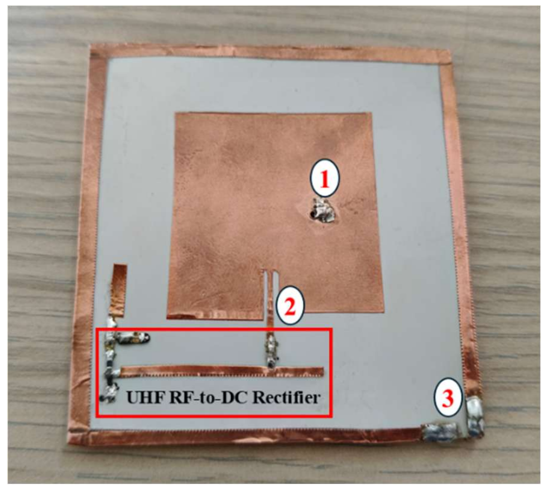

(b)

Figure 3.1. (a) Simulated configuration of the tri-port system, featuring a dual-fed antenna operating at 2.4 GHz —dedicated to data communication on port 1 and FF EH on port 2— and a receiving coil tuned to 13.56 MHz for NF WPT via port 3. (b) Photograph of the front layer of the measured SWIPT tag realized with adhesive copper, with the UHF RF-to-DC rectifier highlighted at the bottom of the tag. [36]. ©2025 IEEE

The overall layout, illustrated in Fig. 3.1(a), results in a compact receiving tag of dimensions 62 × 62 mm^2, which also integrates the NF receiving coil.

The layout foresees three distinct ports that enable simultaneous communication and EH functionalities. Port 1 serves as the communication interface and is implemented through a 50 Ω coaxial feed, ensuring compatibility with standard transceivers (such as the Texas Instruments

CC2530). This port operates with a linearly polarized field oriented along the x-axis (see Fig. 3.1(a)). Port 2, on the other hand, is dedicated to FF EH and employs a microstrip feed connected to a single diode rectifier composed of both lumped and distributed components. The radiated field in this case is linearly polarized along the y-axis (see Fig. 3.1(a)). The third port, Port 3 in Figs. 3.1, corresponds to the NF receiving coil, which will be discussed in the following sub-Paragraph.

To ensure proper operation and isolation between the two radiating ports, the antenna geometry and feeding lines were carefully optimized. In particular, the microstrip line at Port 2 features a width of 0.5 mm, and a length of the feeding insets $L_{inset} = 6.5\,\text{mm}$ corresponding to a characteristic impedance of approximately 109 Ω, which favors impedance matching with the rectifier while limiting mutual coupling with Port 1. Conversely, a standard 50-Ω-impedance with $L_{feed} = 5\,\text{mm}$ was maintained at Port 1 to match the transceiver interface. The slight difference between the patch dimensions $L_{patch} = 33.5\,\text{mm}$ and $W_{patch} = 34.8\,\text{mm}$ further contributes to the electrical isolation and optimal performance of both feeding networks.

To enhance the NF WPT efficiency, the ground plane of the planar antenna was reduced to an area of 50 × 50 mm^2. A further reduction of the ground plane was deliberately avoided to preserve the required antenna gain for both polarization states. This configuration represents a carefully optimized trade-off, ensuring an effective balance between FF radiation performance and inductive NF coupling efficiency.

3.2.2 Antenna and FF UHF Harvesting Measurements

The measured scattering parameters (S-matrix) of the two-port antenna prototype, pictured in Fig. 3.1(b), obtained using 50-Ω terminations, are shown in Fig. 3.2. The reflection coefficient ($|S_{11}|$) of the coaxial-fed communication port exhibits a minimum at 2.40 GHz ($|S_{11}| = –10$ dB), while the EH port reaches its minimum reflection ($|S_{22}| = –15.6$ dB, normalized on the 50 Ω VNA port impedance) at 2.49 GHz.

This slight frequency offset contributes to effective port isolation: the transmission coefficient ($|S_{21}|$) between the two ports remains below –12 dB across the entire 2.4 GHz band, with $|S_{21}| = –15.3$ dB and –12.6 dB at 2.40 GHz and 2.49 GHz, respectively.

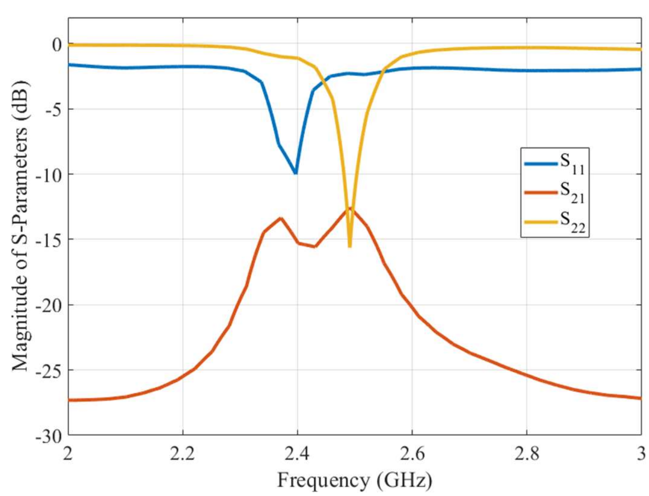

Figure 3.2. Measured magnitude of the scattering parameters for the dual-port 2.4 GHz antenna (Ports 1 and 2 of the RX tag), normalized to 50 Ohm. [36]. ©2025 IEEE

In order to enable RF-to-DC power conversion at both 13.56 MHz and 2.45 GHz, a double-input single-output rectifier has been designed, whose circuit schematic is illustrated and highlighted on the bottom side of Fig. 3.1(b) and detailed in the light blue rectangle of Fig. 3.3. The two rectifiers are connected in parallel, thus sharing the same load (R_{LOAD}) whose optimum value has been derived to emulate the operations of the MPPT of a commercial PMU. The circuit optimizations have been performed simulating one circuit at a time, alternatively adopting an open circuit condition for the circuit not active at the time.

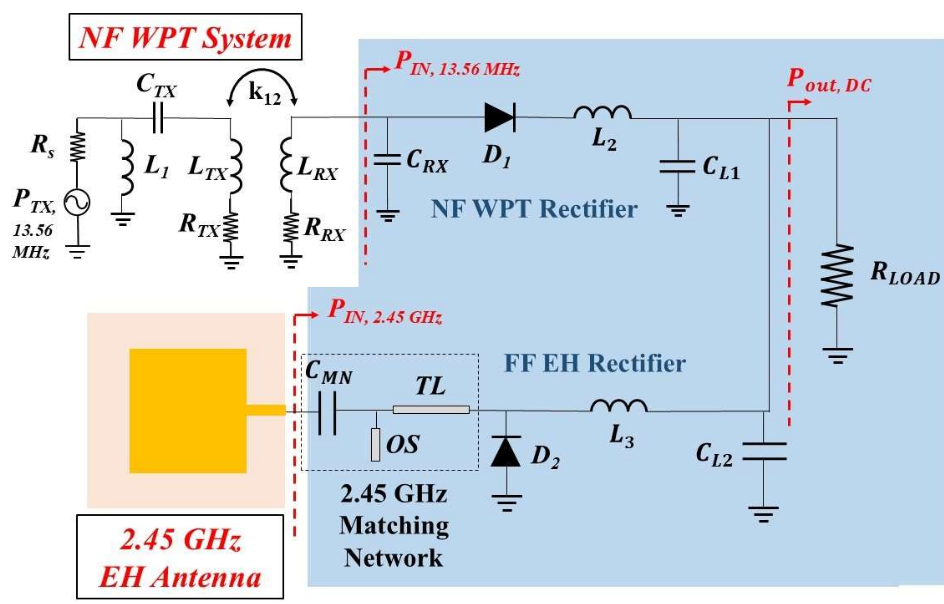

Figure 3.3. Schematic diagram of the overall NF WPT system (TX and RX); the RF-to-DC conversion section of the receiving tag is highlighted in light blue. [35].

Regarding the FF EH section, the RF-to-DC rectifier operating at 2.45 GHz was fabricated on the same Rogers RO3003 substrate as the antenna. The circuit includes a matching network (C_{MN} = 0.26 pF, an 11 mm parallel open stub, and a 22.3 mm series transmission line), a shunt Schottky diode D_2 (Skyworks SMS7630-079LF), and a low-pass filter composed of L_3= 31 µH and C_{L2} = 1 nF. All distributed elements employ 1.4 mm-wide microstrip lines.

Experimental results of the UHF rectifier demonstrated a notable RF-to-DC PCE $\eta_{RF\text{-}to\text{-}DC,2.45\ GHz}$, defined as

$$\eta_{RF-to-DC,2.45GHz} = \left(\frac{P_{out2,DC}}{P_{IN,2.45GHz}}\right) \cdot 100 \qquad (3.1)$$

where $P_{out2,DC}$ represents the DC output power rectified from the RF power received by Port 2 over the optimum output load (849 Ω), and $P_{IN,2.45GHz}$ the UHF power at the input of the RF-to-DC rectifier.

As illustrated in Fig. 3.4, the circuit delivers approximately 40 µW and 5 µW of DC power for RF input levels of –10 dBm and –16 dBm, respectively, confirming the robustness and practical viability of the proposed EH design.

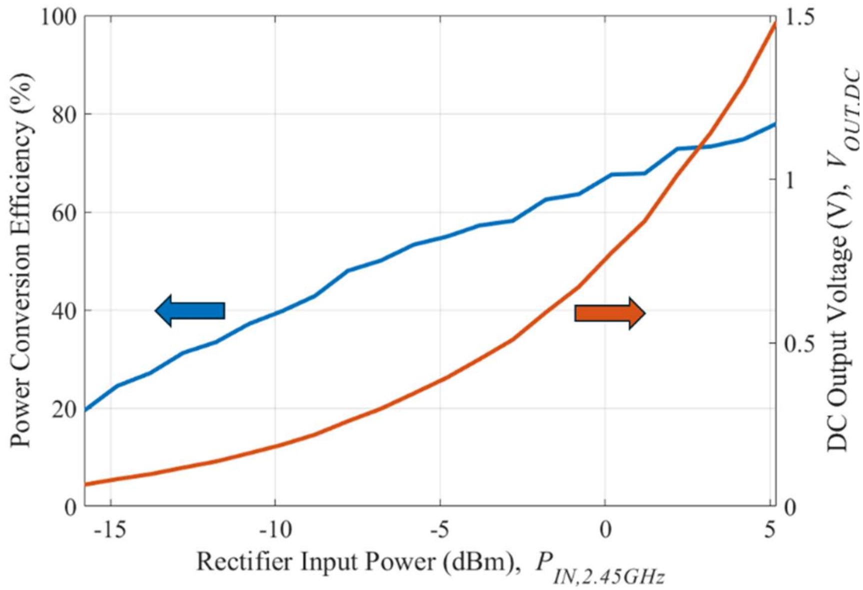

Figure 3.4. Measured PCE ($\eta_{RF\text{-}to\text{-}DC,2.45GHz}$) and output voltage ($V_{OUT,DC}$) for the 2.45 GHz UHF harvester. [36]. ©2025 IEEE

3.3 Design and Validation of the Near-Field WPT System at 13.56 MHz

In the same plane of the dual-polarized antenna, a receiving coil has been embedded in the wearable tag (see Figs. 3.1). The RX equivalent circuit on the tag side consists of a resonating system composed of a 1-turn RX square coil of dimensions $L_{coil} = W_{coil} = 62$ mm, width of 2 mm, and copper thickness of 35 µm (coil equivalent inductance $L_{RX} = 127.2$ nH and resistance

$R_{RX} = 0.05\ \Omega$ at 13.56 MHz) and a parallel capacitor $C_{RX} = 1.12$ nF, loaded by the HF rectifier, which is made up of a series diode D_1 (Skyworks Schottky diode SMS3922-079LF), followed by a low-pass section with $L_2 = 2.2$ µH, and $C_{L1} = 10$ nF.

Two different TX coils were used in the experimental setup to assess the NF WPT performance. The first, referred to as TX-1, consisted of a compact, curved single-turn coil (5.2 × 10.0 cm²) made of 0.70 mm-diameter Litz wire, following the same configuration described in [102]. The second, TX-2, was a larger planar single-turn coil fabricated on an Isola DE104 substrate ($\varepsilon_r = 4.46$, $tan(\delta) = 0.020$, thickness = 1 mm) with overall dimensions of 20 × 13 cm² and a trace width of 3 mm. To ensure proper resonance, TX-1 was tuned with a parallel capacitor of 430 pF connected in series with a 140 nH inductor, while TX-2 operated under a parallel-resonant configuration using a 22 pF capacitor.

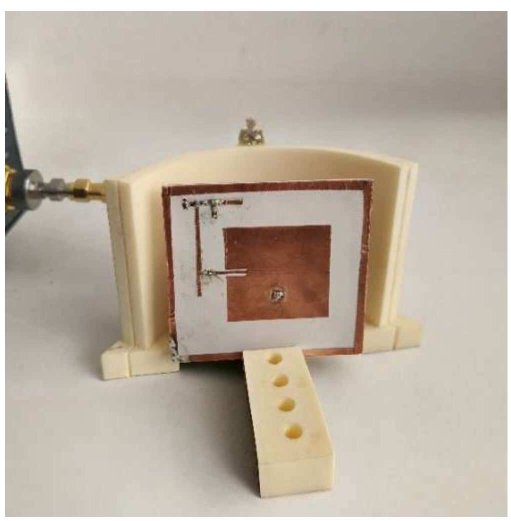

Figure 3.5. NF-powering measurement setup adopting TX-1 prototype (Litz wire incapsulated into a polymeric 3D-printed support) as TX coil in the HF band. [36]. ©2025 IEEE

Coupling measurements between the TX and RX coils were carried out under different experimental conditions. In the first configuration, the smaller curved TX-1 coil was employed as the transmitter, while the RX coil was placed at a fixed position 3 cm away from the TX center. Under this setup (see Fig. 3.5), the overall RF-to-DC efficiency at 13.56 MHz ($\eta_{RF,TX\text{-}to\text{-}DC,13.56MHz}$) reached 30.9%, computed as:

$$\eta_{RF,TX-to-DC,13.56MHz} = \left(\frac{P_{out3,DC}}{P_{TX,13.56MHZ}}\right) \cdot 100 \tag{3.2}$$

where $P_{out3,DC}$ is the DC output power, received by Port 3, calculated over the optimum output load (637 Ω), and $P_{TX,13.56MHz}$ the power transmitted (here, 20 dBm) by the RF generator (Keysight N5183B).

In a second configuration, the larger planar TX-2 coil was used as the transmitter. The RX coil was placed directly in contact with the Isola DE104 substrate, and measurements were performed at several positions across the coil surface (as shown in Fig. 3.6) to evaluate spatial variations in magnetic coupling.

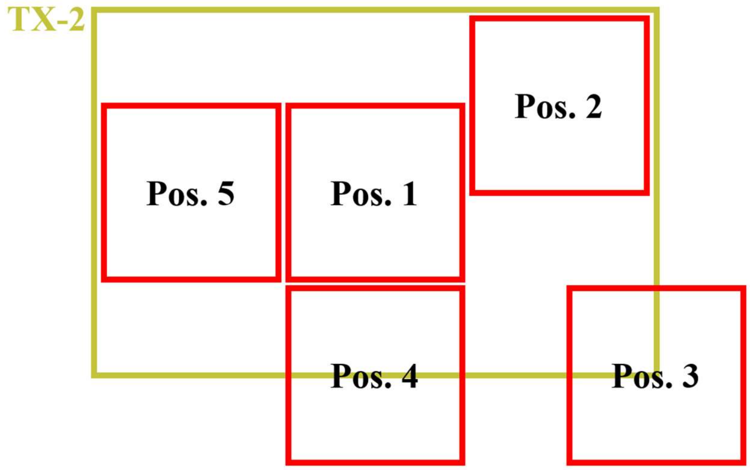

Figure 3.6. Different testing positions for coupling and PCE measurements between TX-2 (yellow) and RX (red). [36]. ©2025 IEEE

The resulting RF-to-DC efficiencies are summarized in Table 3.1 for the five tested positions. As in the previous case, the transmitted RF power was set to 20 dBm, while the output load was fixed at 490 Ω—optimized for the central position (Position 1) of the TX-2 coil.

TABLE 3.1

PERCENTAGE PCE FOR TX-2 FOR DIFFERENT RX POSITIONS

Position	1	2	3	4	5
$\eta_{RF,TX\text{-}to\text{-}DC,13.56MHz}$ (%)	2.17	21.42	0.002	0.08	11.76

As shown in Table 3.1, the overall efficiencies obtained with TX-2 are lower than those achieved using TX-1. This reduction mainly stems from the larger physical dimensions of the TX-2 coil relative to the RX coil. Experimental observations revealed that the magnetic coupling is notably stronger when the RX coil is positioned near the edges of the transmitting coil—particularly along the shorter sides (Position 5) or at the corners (Position 2)—rather than at its center (Position 1). This occurs because the magnetic flux lines tend to diverge outward near the edges, enhancing the effective magnetic linkage between the two coils. Conversely, at the coil center, where the magnetic field is more uniform and perpendicular to the plane, the smaller RX coil captures less total flux. Consequently, the fringe regions of the TX coil offer more favorable conditions for maximizing mutual inductance and improving power transfer efficiency. On the other hand, Positions 3 and 4 were deliberately chosen as representative limit/worst-case scenarios, since in these misaligned configurations the RX coil is positioned near the perimeter of the TX, with a portion of its area extending outside the transmitting region. In these conditions, the magnetic flux between the two coils is minimal and highly non-uniform, as the magnetic field lines from the TX intersect the RX at oblique angles and with reduced magnitude. Consequently, the effective mutual inductance between TX and RX decreases sharply, leading to a substantial drop in PTE.

3.4 Conclusion

This Chapter presents a hybrid SWIPT architecture that seamlessly combines NF and FF EH within a single, compact, and flexible receiving tag. The proposed system integrates a dual-mode harvesting structure, featuring a 13.56 MHz resonant inductive coil for NF power transfer and a cross-polarized antenna operating at 2.4 GHz for FF EH and bidirectional data communication.

The tag employs a dual-fed antenna configuration—combining coaxial and microstrip feeds—to optimize radiation performance across orthogonal polarizations, thereby ensuring reliable communication and efficient energy capture. The design has been validated through both EM simulations and experimental measurements, demonstrating strong performance in both regimes: the NF-WPT setup with comparable TX/RX coil dimensions achieved a 31% RF-to-DC conversion efficiency (at 100 mW source power), while the FF-WPT path reached a 40% efficiency (for a rectifier input power of 100 µW).

Tailored for low-power wireless applications such as IoT nodes, RFID systems, and body-centric sensor networks, this integrated platform provides a compact and efficient solution for simultaneous EH and data transmission. Overall, the results highlight the potential of the proposed dual-mode SWIPT system to enhance the adaptability, efficiency, and integration of next-generation wireless power and communication technologies.

Chapter 4. Antenna Topology and Design Considerations for Wearable RFID Tags on Lossy Dielectric Substrates

This Chapter is based on the following article:

[37] G. Battistini, G. Paolini, D. Masotti, and A. Costanzo, "Revisiting Antenna Topology for Wearable RFID Tags on Lossy Dielectric Substrates," in *2025 IEEE International Conference on RFID Technology and Applications – RFID-TA 2025*, Valence, France, Oct. 2025.

This work was partly funded by the EU (NextGenerationEU) under the Italian National Recovery and Resilience Plan (NRRP), Mission 4, Component 2, Investment 1.3 (CUP: J33C22002880001), partnership on "Telecommunications of the Future" (PE00000001 – program "RESTART"). This study was carried out also within the Spoke 13 of MOST (Sustainable Mobility National Research Center) and received funding from the European Union under the NextGenerationEU programme Italian National Recovery and Resilience Plan (NRRP), Mission 4, Component 2, Investment 1.4 – D.D. 1033 17/06/2022, CN00000023).

4.1 Introduction

In the framework of wearable antennas, which demand robustness, lightweight construction, low cost, and seamless integration into clothing or accessories, RFID technology has proven particularly effective for health and biological monitoring systems, since it meets the adaptability requirements of WBANs [103] and can operate without batteries by harvesting ambient RF energy. This capability enables continuous, non-invasive monitoring and localization, making RF EH an increasingly attractive solution for low-power, energy-autonomous wearable and implantable devices.

Several studies have demonstrated high-frequency wearable RFID tags that combine adaptability, cost-effectiveness, and reliability, even when integrated onto common flexible textile substrates such as felt [104], pile [105], and denim [106]. These designs aim to preserve user mobility by enabling non-invasive integration of the RX tag. However, the RF energy reaching the RX antenna is inherently limited and often unstable. External factors such as user movement, antenna bending, distance and orientation relative to the TX antenna or reader, multipath fading, and EM interference from nearby objects can all significantly degrade performance. Therefore, these factors must be carefully addressed in the rectenna design process from both EM and circuit perspectives to optimize PCE and the resulting rectified DC power [107], [80].

The choice of the antenna is particularly crucial in wearable RFID tags, which demand compactness, lightweight design, and affordability. Commonly used thin, flexible, and inexpensive substrates, while convenient, exhibit high dielectric losses that impair EM propagation and radiation. Within this framework, the antenna must satisfy two essential requirements. First, it should ensure safe and reliable operation in proximity to the human body—providing adequate shielding to mitigate detuning effects and minimize SAR. Second, it must maintain high radiation efficiency even when implemented on low-cost, lossy dielectric substrates, in order to maximize RF EH. Among the various configurations proposed in the literature, microstrip patch antennas are most commonly adopted because of their high radiation efficiency, low-profile geometry, straightforward integration with planar and flexible substrates, and intrinsic compatibility with wearable applications [106], [107], [108], [109]. However, despite these advantages, their performance deteriorates significantly when realized on highly lossy substrates—such as common textiles or 3D-printable polymers—as extensively discussed in Chapter 2.

Building on these observations, this Chapter critically reassesses the suitability of patch antennas when implemented on typical low-cost, lossy substrates, by reaching, to the author‘s knowledge, novel results useful in building RFID tags. The study highlights that their resonant behavior and radiation efficiency are strongly influenced not only by the substrate's relative permittivity (ε_r) and thickness (h), but also by its finite dielectric conductivity (σ). To substantiate these considerations, EM simulations and equivalent circuit models of receiving patch antennas are presented. Furthermore, to demonstrate the advantages of alternative topologies, two wearable rectennas fabricated on common denim textile are compared—one based on a patch antenna and the other on a shielded meandered dipole—highlighting the latter's superior robustness and efficiency for realistic wearable applications.

4.2 Microstrip Patch Antenna's EM Performance Analysis on Lossy Dielectrics

4.2.1 Substrate's Dielectric Properties Influence on EM Performance of the Receiving Patch Antenna

For optimal microstrip patch antenna performance, substrates with low relative dielectric constant (ε_r) and loss tangent ($tan(\delta)$), and greater thickness ($h << \lambda_0$) are usually preferred [110]. The loss tangent $tan(\delta)$, commonly used to quantify dielectric losses, is defined as:

$$tan(\delta) = \frac{\sigma}{\omega \varepsilon_0 \varepsilon_r} \tag{5.1}$$

where ω is the angular operation frequency, ε_0 is the free-space dielectric permittivity, and σ the dielectric conductivity.

However, the EM properties of thin, low-cost, common materials such as textiles or 3D-printable plastics, are often inadequate when used as dielectric substrates, as they typically fail to meet the requirements for achieving high antenna gain, one of the most critical factors in low-power EH applications. Their inherently high dielectric losses ($tan(\delta)$) [106], resulting from elevated dielectric conductivity (σ), when compared to specialized RF substrates, significantly degrade the antenna's radiation efficiency, which, for an antenna in TX mode, is defined as:

$$\eta_{rad} = \frac{P_{rad}}{P_{in}} \tag{5.2}$$

where P_{rad} is the radiated power, and P_{in} is the power supplied to the antenna by the generator. For an antenna in RX mode, the same quantity can be interpreted as the ability of the antenna to capture the impinging RF power. Thus, maximizing this quantity means maximizing the energy harvested by the RFID tag, which is key in EH for low-power applications.

To demonstrate the efficiency limitations of patch antennas in this context, consider a simple receiving patch antenna designed for low-power EH in the 2.4 GHz ISM band. The antenna was modeled using CST Microwave Studio and fabricated with a 35 µm-thick copper layer (σ = 5.8 × 10^7 S/m) on a denim textile substrate, characterized by a dielectric constant $\varepsilon_r = 1.7$ and a loss tangent $\tan(\delta) = 0.025$ [106], corresponding to a dielectric conductivity $\sigma = 5.8 \times 10^{-3}$ S/m at 2.45 GHz. The substrate thickness is $h = 0.78$ mm. The design consists of a square patch ($L = W = 46.5$ mm), matched to a standard 50 Ω microstrip feed line and resonating at 2.45 GHz. At resonance, the input impedance is $Z_A = R_A + jX_A$, with $R_A \approx 50$ Ω and a negligible reactive component. However, simulations reveal a radiation efficiency of only 25%, corresponding to a modest 2-dBi gain, primarily due to the pronounced dielectric losses of the textile substrate.

According to classical antenna theory, the antenna input resistance can be expressed as the sum of its radiation and loss components, $R_A = R_{rad} + R_{loss}$. In receiving mode, R_{rad} quantifies the antenna's ability to capture incident EM power (neglecting polarization or alignment mismatches), while R_{loss} accounts for Joule losses arising from the finite conductivity of the conductors and the dielectric. Considering this, it becomes particularly relevant to quantify the relative contributions of R_{rad} and R_{loss} in patch antennas fabricated on lossy dielectric mediums [100].

To separate these effects, the same antenna was simulated using ideal, lossless materials. In this case, the radiation efficiency rises dramatically to 94%, yielding an 8-dBi gain and an input impedance at resonance of $Z_A = 11 + j0$ Ω. This indicates $R_{rad} \approx 11$ Ω, while the remaining 39 Ω in the real lossy case can be attributed to R_{loss}. Consequently, approximately 75% of the incident RF energy is dissipated as heat rather than transferred to the load.

This analysis offers an initial understanding of how dielectric conductivity impacts the radiation performance of patch antennas. However, an even more critical phenomenon—one that, to the author knowledge, has not yet been explicitly discussed in the literature—emerges when considering substrate materials with higher dielectric conductivity.

To isolate the effect of conductivity-related losses from purely ohmic dissipation, we consider a substrate exhibiting a loss tangent comparable to that of denim, but with higher dielectric permittivity and conductivity. Maintaining a similar loss tangent implies selecting materials with an equivalent ratio between permittivity and conductivity. In this framework, FR-4 can be regarded as electromagnetically analogous to denim in terms of loss tangent, yet characterized by larger conductivity-driven losses. FR-4 is a widely used, low-cost, and lossy RF material, characterized by a relative permittivity $\varepsilon_r = 4.3$ and a loss tangent $\tan(\delta) = 0.025$, corresponding to a dielectric conductivity $\sigma = 0.014$ S/m at 2.45 GHz.

Thus, let us examine a square patch antenna designed to operate in the 2.4 GHz ISM band and fabricated on a 1 mm-thick FR-4 substrate.

As a starting point, the antenna is modeled using perfect electric conductor (PEC) metallization and an ideal, lossless version of FR-4. In this configuration, a patch size of $L = W = 29.5$ mm ensures resonance at 2.42 GHz. To maintain a simple geometry and prevent additional field distortions, no inset matching for 50 Ω feed-line adaptation is introduced.

Next, the same geometry is retained while substituting the ideal materials with realistic ones, a 35 μm-thick copper layer for the metallization and lossy FR-4 for the substrate. The resulting input impedance and corresponding radiation efficiency at 2.42 GHz are summarized in Table 4.1.

TABLE 4.1

EM COMPARISON OF PATCH ANTENNA ON FR-4 DIELECTRIC SUBSTRATE W/ AND W/O LOSSES

	Antenna's Input Impedance Z_A	**Radiation Efficiency η_{rad}**
Lossless Patch Antenna	$Z_A = 7.4 + j0\ \Omega$	95%
Lossy Patch Antenna	$Z_A = 24 + j18\ \Omega$	26%

The comparison highlights that the inclusion of conductor and dielectric losses not only adds a significant loss resistance component ($R_{loss} = 16.6\ \Omega$) to the radiation resistance ($R_{rad} = 7.4\ \Omega$), but also introduces a notable increase in the reactive impedance, with $\Delta X_A = 18\ \Omega$. This behavior underscores the detrimental impact of dielectric losses on both the resistive and reactive characteristics of patch antennas implemented on lossy substrates.

4.2.2 Equivalent Circuit Modelling of a Patch Antenna

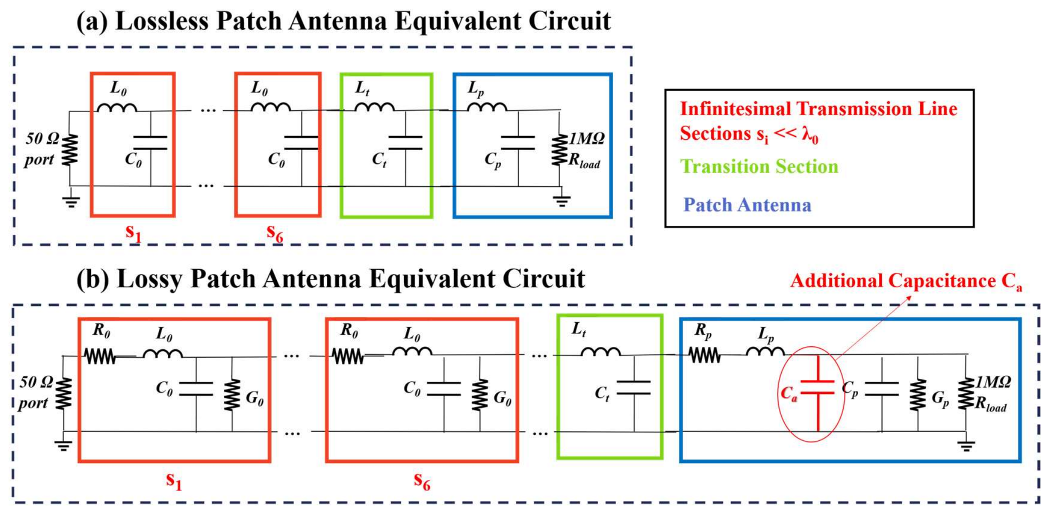

Figure 4.1. Lumped-element equivalent circuit model of a microstrip-fed patch antenna on FR-4 substrate: (a) ideal lossless materials, and (b) realistic ones. The feeding line is marked in red, the transition in green, and the patch antenna, in blue. [37]. ©2025 IEEE

To gain a deeper understanding of the increased reactive effects observed in the antenna impedance, simplified lumped-element equivalent circuit models were developed for the antenna implemented on both lossless and lossy FR-4 substrates, as illustrated in Figs. 4.1. The feeding microstrip line (length l_f = 15 mm, width w_f = 2 mm, corresponding to a 50 Ω characteristic impedance) was modeled as a cascade of six electrically short sections (s_i, $i = 1 \ldots 6$), each representing a $\lambda_0/8$-long segment [111]. The square patch ($L = W = 29.5$ mm) was modeled as a wider open-ended stub.

In the lossless case (Fig. 4.1(a)), each section s_i comprises a series inductance L_0, representing the magnetic field associated with the current along the line, and a shunt capacitance C_0, representing the electric field between conductors. The patch itself is described by a series inductance L_p and shunt capacitance C_p, terminated with a high resistance R_{load} = 1 MΩ to model the open-circuit boundary at the patch edge. A series inductance L_t and shunt capacitance C_t are added to represent the line-to-patch transition.

In the lossy configuration (Fig. 4.1(b)), each section s_i includes additional series resistance R_0 (accounting for conductor losses) and shunt conductance G_0 (modeling dielectric losses). Similarly, for the patch, R_p and G_p are introduced. To accurately reproduce the simulated input impedance, an additional parallel capacitance C_a is incorporated. This element models the excess reactive contribution observed in the impedance of the lossy patch (see Table 4.1), which originates from electric energy trapped within the substrate—energy that does not contribute to radiation and therefore degrades efficiency.

The lumped-element values of the equivalent circuit models in Figs. 4.1 are reported in Table 4.2, and were extracted through circuit optimization to match the frequency-dispersive complex impedance obtained from full-wave EM simulations over the 1.5–3 GHz range.

TABLE 4.2

EQUIVALENT CIRCUIT MODEL LUMPED ELEMENTS PARAMETERS

Lossless Patch Antenna		**Additional Lumped-Elements in Lossy Patch Antenna**	
Lumped-Element	***Value***	***Lumped-Element***	***Value***
L_0	0.9 nH	G_0	10000 S
C_0	0.34 pF	R_0	0.01 Ω
L_t	1.1 nH	R_p	0.9 Ω
C_t	4.4 pF	G_p	4000 S
L_p	3.6 nH	$\boldsymbol{C_a}$	**0.06 pF**
C_p	1.6 pF		

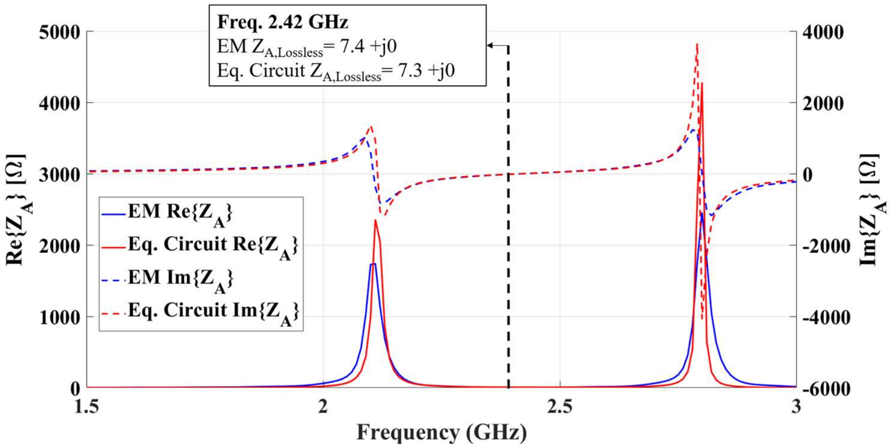

(a)

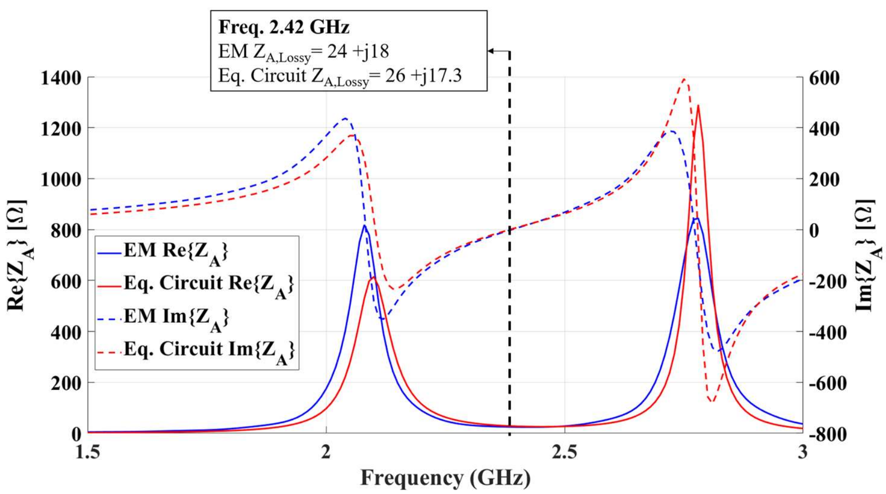

(b)

Figure 4.2. Real (continuous lines) and imaginary (dotted lines) parts of the patch antenna input impedance obtained from full-wave EM simulation (in blue) and from the lumped-element equivalent circuit model (in red): (a) ideal lossless case, (b) lossy case. [37]. ©2025 IEEE

The comparison between the simulated and equivalent-circuit input impedances, shown in Figs. 4.2, demonstrates an excellent agreement for both lossless and lossy configurations, validating the accuracy of the proposed models.

This leads to the conclusion that the resonant frequency, f_0, of a patch antenna on lossy dielectrics, depends not only on the substrate's permittivity ε_r and thickness h, but also on its conductivity σ. Since the dependency on f_0, ε_r and σ are summarized in the loss tangent $tan(\delta)$, defined in eq. (4.1), the radiation efficiency must be expressed as η_{rad} ($tan(\delta)$, h).

As widely established, when it comes to wearable RFID tags, the substrate thickness is selected as a trade-off between minimum weight and invasiveness, and good radiation performance [112]. Based on this, an analysis is carried out to evaluate patch radiation efficiency and size as functions of substrate permittivity and thickness, aiming to provide design guidelines for lossy substrates. It is shown that a proper combination of these parameters allows a balance between radiation efficiency and overall dimensions. To this end, a parametrized full-wave analysis of a square patch antenna operating at 2.4 GHz is carried out: the substrate's dielectric conductivity is $\sigma = 0.014$ S/m, while the substrate's dielectric permittivity and height are varied from 1 to 4.5 and from 1 to 4 mm, respectively. This means that, as we increase the relative permittivity keeping the same conductivity, the loss tangent inherently decreases.

The results of the EM simulations are presented in the 3D graph of Fig. 4.3, where the patch radiation efficiency is visualized as a surface over a 3D cartesian grid, whose curvature and colormap reflect the interplay between substrate's height, permittivity (and consequent patch dimension) and the radiation efficiency. Choosing a low permittivity slightly increases radiation efficiency but raises the loss tangent and enlarges the antenna. In contrast, increasing substrate thickness effectively improves efficiency by offsetting losses, though it further increases the antenna footprint. The dotted rectangles in Fig. 4.3 highlight two regions with comparable radiation efficiency but different substrate properties. The top region refers to the conventional choice of low permittivity and moderate thickness, resulting in larger patches. In contrast, the bottom region shows that similar efficiency can be achieved with higher permittivity and comparable thickness, allowing more compact designs. Therefore, as a second conclusion, when comparing two dielectrics with similar ohmic losses, a patch with both reduced size and good radiation efficiency can be achieved, selecting a material with higher dielectric permittivity and acceptable, limited thickness. This choice provides miniaturization and still good radiation efficiency. However, it should be noted that increasing the substrate permittivity typically results in higher electric energy storage within the substrate, leading to a higher quality factor ($Q=1/tan(\delta)$) and consequently a reduced impedance bandwidth ($BW=1/Q$). Hence, the adoption of high-ε_r materials inherently involves a trade-off between compactness, bandwidth, and robustness to detuning, which must be carefully considered in wearable and lossy environments.

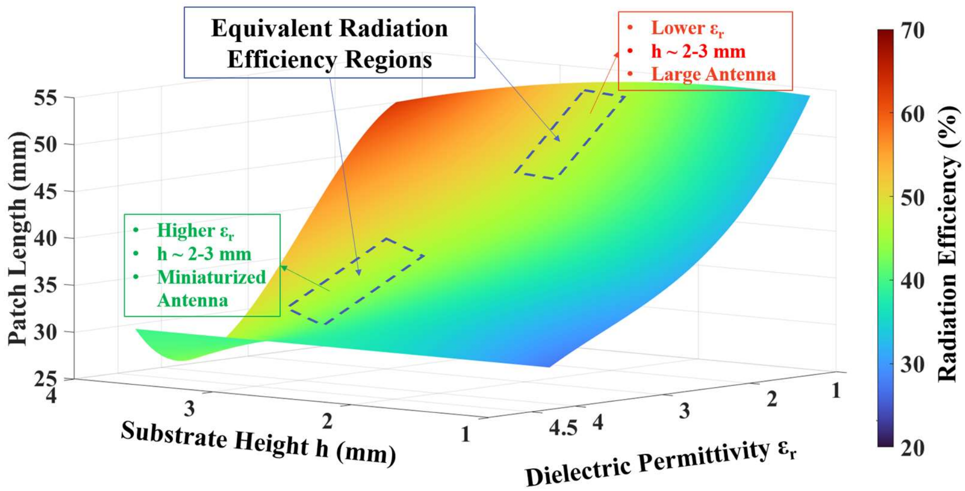

Figure 4.3. Influence of the combined effects of dielectric substrate's permittivity and thickness on the radiation efficiency and physical length of a squared patch antenna, operating in the 2.4 GHz band. The substrate's dielectric conductivity is fixed to $\sigma = 0.014$ S/m, while ε_r is varied from 1 to 4.5 and h among the values 1 to 4 mm. The surface curvature indicates the radiation efficiency and its color gradient maps the corresponding patch dimensions. The dotted rectangles indicate substrate configurations with comparable radiation efficiency. The lower region, with higher permittivity and miniaturized patch size, may represent a more efficient design trade-off than the upper one. [37]. ©2025 IEEE

4.3 Wearable Rectennas on Lossy Substrates Comparing Different Receiving Antenna Topologies

Two wearable rectennas (illustrated in Fig. 4.5), operating at 2.45 GHz, were designed and compared, both employing denim fabric as the substrate: one based on a microstrip patch antenna, and the other on a shielded meandered dipole. Meandered dipoles in planar technology are widely regarded as the gold standard for generic RFID tags, due to their isotropic radiation pattern, their relatively high gain (typically around 2 dBi), compact size, and ease of integration with electronic components and chips. In such configurations, the dielectric substrate simply acts as a mechanical support for the conductive traces responsible for radiation. However, when wearability is required, a metallic shielding layer becomes essential for isolating the dipole performance from the effects of the human body, and for generating a desirable front-to-back ratio.

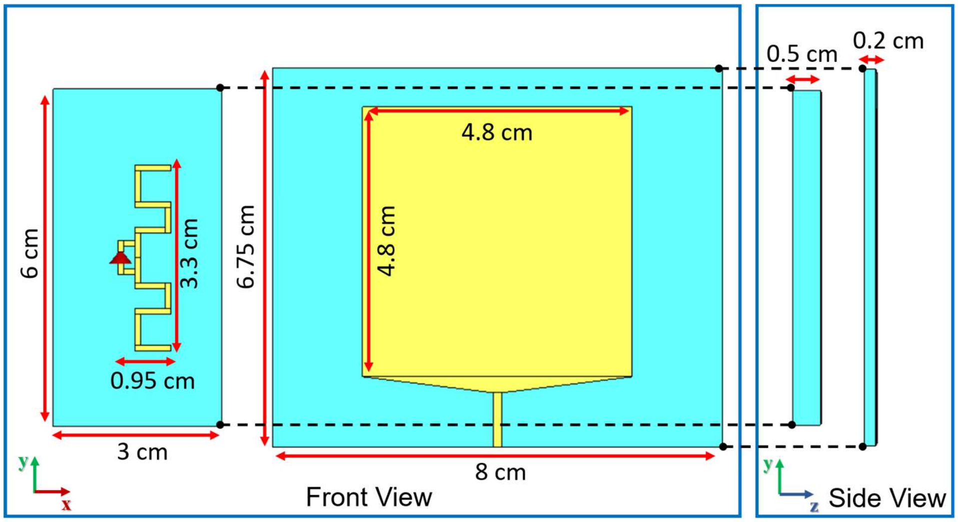

Figure 4.4. Geometry and dimensions of the two compared wearable RFID tag's RX antennas on denim textile as substrate: front and lateral view layouts of the shielded meandered dipole (3×6×0.5 cm^3), on the left, and those of the patch antenna (6.75×8×0.2 cm^3), on the right.

To meet the compactness requirements typical of wearable systems, the shield is placed on the opposite side of a thicker denim substrate of height h_{dipole} = 5 mm, with the dipole strip lines on the opposite surface. This substrate thickness results as a trade-off between maximizing radiation efficiency and minimizing space occupation and the dielectric's influence on the dipole's resonant behavior. As a result, the final antenna design is a meandered dipole whose dimensions are reported in Fig. 4.4, compared to the ones of a 2.45-GHz patch antenna designed on the same denim substrate with thickness h_{patch} = 2 mm.

This comparison also underscores a key design principle for RX antennas in RFID tags intended for low-power EH applications, where miniaturization of the final footprint is a central condition for integration.

The primary objective is not to achieve a fixed 50-Ω match, but rather to ensure that the antenna resonates effectively with the entire receiving front-end. Traditional narrowband MNs designed to transform the antenna impedance to 50 Ω introduce additional losses and size penalties, which are undesirable in compact, low-power RFID tags. Thus, since strict 50-Ω impedance matching is not required, the antenna is directly connected to a nonlinear rectifier, followed by a DC-to-DC converter acting as a PMU, which dynamically adjusts to track the rectifier's optimal load conditions.

Since the rectifier's input impedance is complex and strongly dependent on the incident RF power level due to its nonlinear behavior, the most effective strategy is to directly conjugate-match the antenna's input impedance to that of the rectifier over the expected range of received power levels in the target EH scenario.

Accordingly, in the following analysis, the antenna geometries have been specifically optimized for direct conjugate matching with the rectifier input, aiming to minimize the RFID tag footprint and eliminate unnecessary losses associated with intermediate MNs [28].

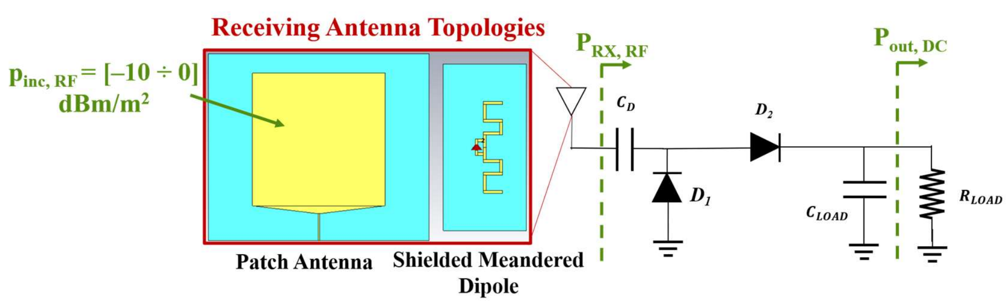

Figure 4.5. Wearable rectennas on denim textile as substrate, with emphasis on two distinct receiving antennas topologies, both designed to have an input impedance conjugately

matched to that of the rectifier at 2.45 GHz: on the right, the layout of the shielded meandered dipole; on the left, the layout of the patch antenna. [37]. ©2025 IEEE

The topology of the rectifier adopted for this analysis is a voltage doubler, consisting of a pair of Skyworks SMS7630-079LF Schottky diodes characterized at the operating frequency of 2.45 GHz, and two capacitors, C_D and C_{LOAD}, as illustrated in Fig. 4.5. The nonlinear simulation of the rectifier input impedance over an RF input power range from −20 to −10 dBm, at the frequency of 2.45 GHz, shows that it remains nearly constant at: $Z_{rec} = 5 - j70\ \Omega$. Careful tuning of the two RX antenna designs, namely the patch antenna and the shielded meandered dipole, resulted to achieve an input impedance Z_A closely matched to the complex conjugate of the rectifier impedance, Z_{rec}*. In particular, the resulting impedances are $Z_{A,Patch} = 9.4 + j64\ \Omega$, and , $Z_{A,Dipole} = 4.5 + j75\ \Omega$, for the patch and the dipole, respectively.

To evaluate the effective received power ($P_{RX,\ RF}$), for a RF incident power density ($p_{inc,RF}$), impinging respectively on the two antennas, the following expression has been adopted:

$$P_{RX,RF}[W] = p_{inc,RF}[W/m^2] \cdot A_{eff}[m^2] \qquad (4.3)$$

where the antenna effective aperture A_{eff} accounts for the wavelength λ_0, corresponding to the operating frequency, and the gain (G) of the antenna, in its linear form:

$$A_{eff} = \frac{\lambda_0^2 G}{4\pi}. \qquad (4.4)$$

In this study, to explore the performance boundaries of the proposed rectennas, an incident power density $p_{inc,RF}$ ranging from −10 to 0 dBm/m^2 is considered, assuming a controlled WPT scenario in which an intentional TX antenna is placed at a fixed distance from the rectennas under test, such that the actual impinging power on the receiving antennas falls within this interval. For the two antenna topologies, having gains $G_{Dipole} = 2.3$ dBi and $G_{Patch} = 4.3$ dBi, respectively, the resulting effective apertures are $A_{eff,Dipole} = 20.9$ cm^2 and $A_{eff,Patch} = 33.6$ cm^2, which correspond to received power levels P_{RX,RF_Dipole} and P_{RX,RF_Patch}, ranging from −36.9 to −26.9 dBm and from −34.9 and −24.9 dBm, for the shielded dipole and for the patch antenna, respectively. The two rectennas are optimized and simulated on Keysight ADS, and their respective performances are reported in Fig. 4.6(a), in terms of rectified DC power, $P_{out,DC}$, and RF-to-DC power conversion efficiency, $\eta_{RF\text{-}to\text{-}DC}$, which is computed as:

$$\eta_{RF-to-D} = \frac{P_{out,DC}}{P_{RX,RF}} \cdot 100. \tag{4.5}$$

The results are plotted versus the predicted dipole received power range to ensure a fair comparison. As shown in Fig. 4.6(a), although the shielded dipole has a smaller effective aperture than the patch antenna, the rectenna adopting the shielded dipole outperforms the patch-based rectenna in both RF-to-DC efficiency and rectified DC power. This behavior is attributed to the EM energy trapped within the patch structure—modeled by C_a (see Fig. 4.1(b))—which is absent in the dipole case. These results further reinforce our design rationale, confirming that the shielded meandered dipole represents a more suitable and robust solution for wearable rectenna applications involving low-cost, lossy substrates, where the patch antenna performance is inherently limited by substrate-dependent EM effects.

As a further figure of merit (FoM), the rectennas DC powers relative to their volume (in cm^3) are evaluated providing a normalized measure of performance versus size:

$$FoM\left[\frac{\mu W}{cm^3}\right] = \frac{P_{out,DC}\,[\mu W]}{Antenna\ Volume\ [cm^3]}, \tag{4.6}$$

where the antennas volumes, as reported in Fig. 4.4, are: 9 cm^3, for the shielded meandered dipole (3 x 6 x 0.5 cm^3) and 10.7 cm^3 for the patch antenna (6.7 x 8 x 0.2 cm^3), respectively.

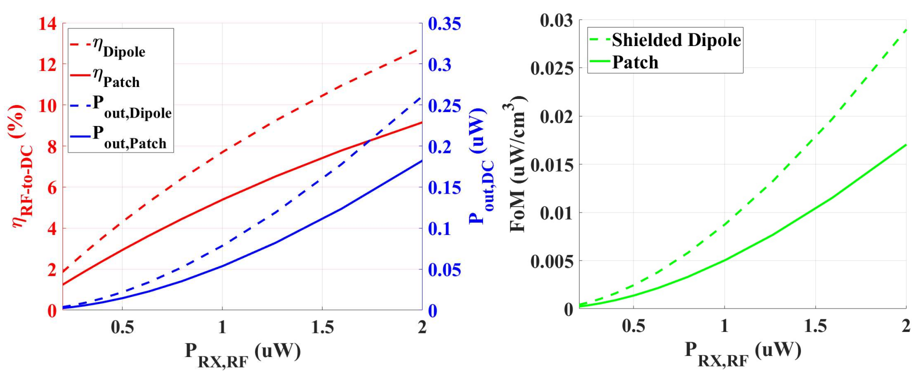

(a) (b)

Figure 4.6. (a) Simulated rectennas performance versus $P_{RX,RF}$, corresponding to $p_{inc,RF}$ spanning from −10 to 0 dBm/m^2; (b) Figure of merit comparing the two rectennas, providing normalized measure of performance versus size versus $P_{RX,\ RF}$. [37]. ©2025 IEEE

For both antenna topologies, the calculated volume includes the length and width of the bottom ground metallization, since the ground plane is a key element in wearable applications and critically affects the EM behavior of the patch. The FoM trends, shown in Fig. 4.6(b), clearly indicate that the rectenna based on the shielded dipole outperforms its patch-based counterpart. These results further consolidate the thesis of this work, demonstrating that in wearable, battery-free, and cost-effective RFID tags built on common low-cost substrates with high dielectric losses, the careful selection of the antenna topology is crucial to maximize harvested RF energy. This finding underscores the inherent limitations of microstrip patches, whose performance strongly depends on the substrate's EM properties and physical thickness. Conversely, alternative antenna architectures—when properly adapted for body-worn, non-invasive RFID tags—can achieve higher RF-to-DC conversion efficiency, even with lossy dielectrics, while simultaneously reducing the tag's overall footprint and invasiveness.

4.4 Conclusion

This Chapter demonstrates that the EM performance of microstrip patch antennas for wearable RFID tags is highly sensitive to the dielectric properties of the substrate, especially when employing thin, low-cost, and inherently lossy materials such as common textiles. The analysis shows that this sensitivity not only causes the expected degradation in radiation efficiency due to resistive losses but also alters the antenna's resonant behavior through an additional reactive component in its impedance, introduced by the substrate's high dielectric conductivity. Moreover, the study reveals that, contrary to conventional antenna theory, within substrates of comparable conductivity, the loss-induced performance degradation associated with higher dielectric permittivity can be mitigated by slightly increasing the substrate thickness—achieving a balance between good radiation efficiency and antenna miniaturization. To address the intrinsic limitations of the patch antenna, a shielded meandered dipole has been proposed and validated as an alternative receiving topology, offering enhanced wearability, comparable efficiency, robustness to substrate losses, and a reduced footprint. Overall, these findings provide practical design guidelines for the informed selection of dielectric substrates and antenna topologies in wearable, battery-free RFID systems, enabling reliable performance even on flexible, lossy materials.

Conclusion

This Thesis has presented a comprehensive investigation into the design, fabrication, and experimental validation of wireless, energy-autonomous platforms for wearable and implantable biomedical systems. By combining EM engineering, AM, and soft material integration, the work advances the understanding and practical realization of wireless power and data transfer technologies for body-centric applications. Across its chapters, the Thesis explores both NF and FF WPT approaches, hybrid energy-harvesting architectures, and conformal antenna design, aiming to overcome the key limitations of existing systems in terms of miniaturization, power autonomy, and material adaptability.

Chapter 1 introduced a fully wireless, battery-free optogenetic implant designed for the selective stimulation of hypoglossal motoneurons in small animal models. The system operates through a conformal 13.56 MHz inductive WPT link, optimized to deliver stable power regardless of animal movement or orientation. In-vivo validation demonstrated effective optical stimulation with minimal invasiveness, confirming the feasibility of lightweight, wireless optoelectronic implants for behavioral neuroscience studies.

Appendix A extended this work by optimizing the TX coil, highlighting how improved fabrication accuracy and resonance matching can significantly enhance the PTE. The study established the basis for efficient, flexible TX structures capable of deep-tissue energy delivery through several centimeters of biological tissue, thus paving the way toward wearable-powered implantable systems.

Chapter 2 presented a fully 3D-printed rectenna system fabricated on a low-cost engineered-PLA substrate, merging AM and EM co-design to enable dual functionality of RF EH and ultra-wideband (UWB) backscattering. Through careful material characterization and optimization of the substrate's dielectric properties, the work demonstrated that mechanical robustness and electromagnetic performance can be concurrently achieved. The dual-port antenna architecture and nonlinear rectifier co-design yielded efficient multi-band operation and compliance with FCC emission standards, supporting low-power communication and localization functionalities. This chapter demonstrated the viability of AM-enabled, low-cost, and flexible energy-autonomous wireless platforms.

Chapter 3 built upon these foundations by introducing a hybrid NF/FF SWIPT architecture. The proposed system combined inductive NF harvesting at 13.56 MHz with FF communication and EH at 2.4 GHz, within a single compact and flexible tag. Both numerical and experimental results confirmed high conversion efficiencies in both coupling regimes, validating the design for IoT, RFID, and body-centric networks. This dual-mode platform exemplifies an efficient and integrable solution for concurrent power and data transmission, addressing one of the central challenges in next-generation wireless systems.

Finally, Chapter 4 explored the EM behavior of wearable antennas implemented on flexible and lossy substrates such as textiles and printable polymers. The study revealed that substrate conductivity and permittivity strongly affect antenna impedance and radiation efficiency, especially in miniaturized microstrip configurations. A shielded meandered dipole topology was proposed as a robust alternative to patch antennas, offering improved efficiency, reduced sensitivity to substrate losses, and enhanced wearability. These findings provide practical guidelines for the design of reliable, conformal, and efficient antennas for flexible RFID and sensing applications.

Taken together, the outcomes of this Thesis highlight the synergistic potential of EM co-design, materials engineering, and additive manufacturing in the realization of integrated wireless platforms. The results confirm that performance optimization cannot rely solely on electromagnetic design but must also consider material selection, substrate morphology, and fabrication accuracy—factors that play a decisive role in determining device robustness, radiation efficiency, and power transfer capabilities.

The integration of near-field inductive and far-field radiative mechanisms—traditionally addressed as distinct paradigms—has been shown to provide complementary benefits. The hybrid SWIPT approach developed in this work enables simultaneous energy and data transmission across different coupling regimes, promoting scalability from implantable micro-systems to distributed wearable networks. Similarly, the investigation of 3D-printed substrates underscores how custom dielectric engineering can extend the design space for conformal RF devices, fostering rapid prototyping and functional integration with minimal cost and environmental impact.

In the biomedical domain, the demonstrated wireless optogenetic implant and miniaturized TX coil exemplify how wearable-powered systems can achieve safe and efficient energy delivery to deep tissue regions—offering a viable path toward fully autonomous implantable therapies. The insights gained into tissue interaction, alignment tolerance, and resonance stability will inform future generations of wireless medical implants.

Appendix A. Design and Optimization of Transmitting Coil for Deep Tissue Inductive Wireless Power Transfer

A.1 Introduction

This Appendix presents the preliminary results of an ongoing research activity that deepens the investigation into inductive WPT links for conformal, wireless and battery-free implantable devices, focusing on the design optimization of the transmitting coil for efficient power delivery through biological tissues. This work was carried out during a three-month research stay (May–July 2025) at the *Querrey Simpson Institute for Bioelectronics*, *Northwestern University* (Evanston, Chicago, USA), under the supervision of Prof. John A. Rogers and Dr. Jianlin Zhou.

The study fits within the broader framework of deep-tissue inductive WPT for implantable biomedical systems, with particular emphasis on a miniaturized, energy-autonomous implantable pacemaker, operating at 30

MHz, where cardiac pacing is mechanically driven by the movement of an aortic stent. In this context, efficient inductive coupling between the external TX coil, integrated into common garment fabrics, and the implantable RX coil, embedded on the surface of an aortic stent, is crucial to enable sufficient power delivery through deep tissue while minimizing both transmitted power and tissue heating.

In scientific literature, numerous studies focus on the design and miniaturization of implantable RX coils, aiming to maximize efficiency, biocompatibility, and mechanical stability of the implant [113]. However, the transmitting side is often overlooked. In many reported works [114], [115], [116], [117], [118], the description of the TX coil is minimal, often limited to a few parameters, or entirely omitted. When the transmitter is described, it is typically realized as a large, rigid coil or requires high transmitted power levels to compensate for the strong attenuation introduced by biological tissues, whose high conductivity significantly reduces magnetic field penetration and coupling efficiency [119].

Most of these studies primarily focus on improving the implantable RX unit to achieve high PCE, while the TX side is often simplified or insufficiently characterized. As a result, key parameters that significantly affect the RF-to-RF efficiency of the inductive link—such as the TX coil inductance, quality factor (Q), and coil dimensions—are not consistently reported. This lack of detailed TX characterization hinders reproducibility and limits the ability to optimize PTE for deep-tissue implants. For instance, while some works report high-efficiency links in vitro or in animal models, the absence of TX design specifications makes it difficult to generalize the results or scale the approach to different implantation depths and tissue types.

In this work, particular emphasis is placed on the design, optimization, and detailed characterization of the TX stage, since this aspect plays a crucial role in determining the overall performance of the link. Highlighting this part of the system is essential in any study aimed at maximizing the end-to-end RF-to-DC efficiency, as achieving high overall efficiency requires optimizing each stage of the power transmission chain: from the generator-to-TX efficiency, to RF-to-RF TX-to-RX coupling, RX-to-rectifier transfer, rectification efficiency, and finally DC-DC conversion performance.
The present work therefore addresses this gap by providing a comprehensive description of a flexible, miniaturized TX coil, including its inductance, Q factor, TX-to-RX coupling considerations, and simulated RF-to-RF PTE at realistic implantation depths.

A.2 EM Design and Optimization of a Three-Layer Miniaturized Transmitting Coil for Deep Tissue Magnetic Field Penetration and WPT

Specifically, this work focused on the design and optimization of a transmitting coil with specific characteristics and performance targets. The TX coil is required to be flexible and adaptable to curved surfaces (suitable for integration with common garment fabrics), maintain a small footprint (maximum $5 \times 5\,\mathrm{cm}^2$), and simultaneously achieve high inductance and quality factor. Additionally, it must ensure effective deep-tissue penetration, corresponding to a high RF-to-RF PTE through biological tissue. Beyond the coil itself, the study aims to optimize the PTE between the RF generator and the TX coil, thereby minimizing the required input power while ensuring compliance with safety limits such as SAR and emission constraints.

To this end, the link is tuned to resonance, and a compact matching network is employed at the TX side to achieve optimal impedance matching and enhance overall efficiency.

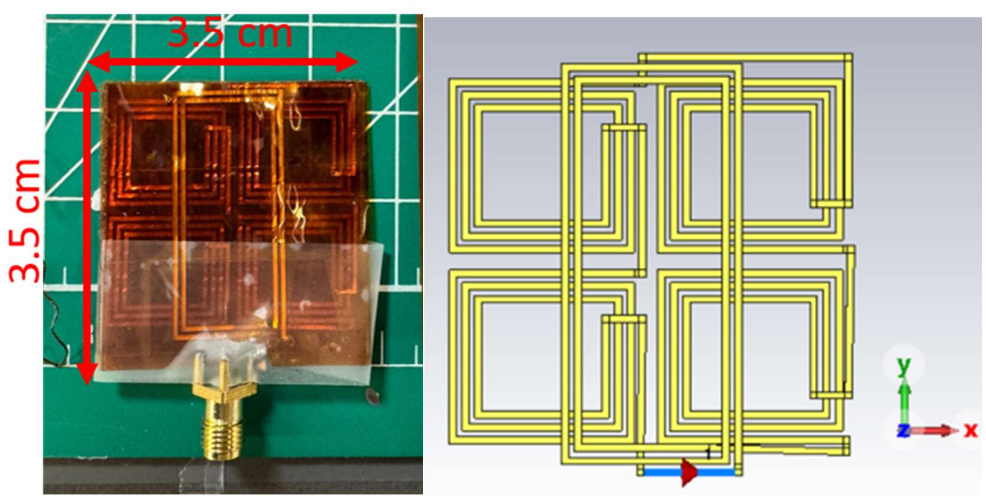

(a) (b)

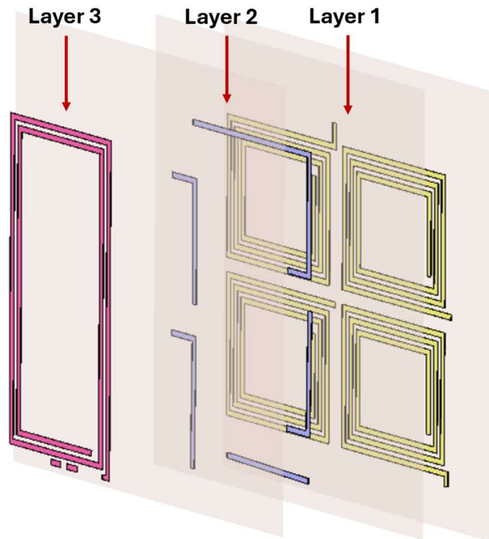

(c)

Figure A.1. Optimized TX coil (3.5 × 3.5 cm²), consisting of five series-connected coils, arranged on three planar Kapton layers: (a) Picture of the fabricated prototype with dimensions highlighted; (b) Coil geometry layout with hidden substrate; (c) exploded view of the TX series-connected coil layout arranged on three layers: layer 1 showing the 4 identical squared coils, layer 2 dedicated to the series connections and layer 3 for the fifth larger coil.

The coil was designed and optimized using full-wave EM simulations in CST to maximize the average magnetic field (H-field) at the location of the implanted receiver, embedded within an aortic stent, placed 7 cm from the TX coil, at the operating frequency of 30 MHz.

The optimized TX coil (3.5 × 3.5 cm²), illustrated in Figs.A.1, consists of five series-connected coils, arranged on three planar Kapton layers (Kapton thickness 50 µm, copper thickness 50 µm, copper width 0.6 mm). In the first layer, starting from the bottom, four identical square coils (3 turns each, 15 × 15 mm²) are arranged in pairs; the second layer provides the series connections between these four coils and the fifth one, which is located on the third layer, featuring 2 turns of copper, dimensions $34.6 \times 15.6\ \mathrm{mm}^2$, is centrally overlapped with the four coils of the first layer (see Fig. A.1(a)). The dispositions of the copper lines on the three layers—series connection lines and the fifth coil positions specifically—were optimized in order to minimize the parallel lines overlapping, and consequently, the capacitive coupling between the three layers, that may affect the overall TX coil inductance.

Following the EM simulations in CST, the coil was fabricated using rapid laser micromachining techniques available at Prof. Rogers' laboratory at Northwestern University. Each layer was realized starting from a single-sided copper-clad Kapton sheet, where the copper metallization was selectively patterned via laser ablation to retain only the coil traces. The multilayer structure was then assembled manually, and interlayer electrical connections were achieved through localized solder joints using a silver-filled solder paste diluted with tin. To ensure mechanical adhesion between the upper and lower layers, the central layer was laminated with a 25-µm-thick adhesive polyimide film, providing both structural bonding and electrical insulation between adjacent copper traces.

The EM characteristics of the fabricated prototype were experimentally measured. As summarized in Table A.1, simulated and measured results show excellent agreement, confirming that the fabricated coil meets the miniaturization requirements (footprint below $5 \times 5\ \mathrm{cm}^2$) while exhibiting high inductance and quality factor at 30 MHz ($Q_{TX,30\ MHz} \approx 54$, $L_{TX,30\ MHz} \approx 1.04\ \mu\mathrm{H}$).

TABLE A.1

SIMULATED AND MEASURED TX COIL INDUCTANCE AND Q FACTOR at 30 MHz

	$\mathbf{Q_{TX,30\ MHz}}$	$\mathbf{L_{TX,30\ MHz}}$
Simulated	57.4	1.17 μm
Measured	54.4	1.04 μm

In the simulated EM model, illustrated in Fig. A.2, the TX coil was positioned a few millimeters above the skin surface, mimicking placement on or integration with textile fabrics. The biological tissue between the TX and RX was represented by a 6 cm slab consisting of skin (1 mm), fat (10 mm), muscle (25 mm), and blood (25 mm), with realistic dielectric properties at 30 MHz: skin, $\varepsilon_r \approx 153$, $\sigma \approx 0.34$ S/m; fat, $\varepsilon_r \approx 17.2$, $\sigma \approx 0.06$ S/m; muscle, $\varepsilon_r \approx 91.8$, $\sigma \approx 0.65$ S/m; blood, $\varepsilon_r \approx 199$, $\sigma \approx 1.16$ S/m [61].

The RX coil (with measured quality factor $Q_{RX,30\ MHz} \approx 4$, and inductance $L_{RX,30\ MHz} \approx 116$ nH at 30 MHz) is realized as a rectangular copper wire of $4 \times 3\,\text{cm}^2$, with sides shaped in a wavy pattern to enable optimal integration with the reticulated tungsten structure of the aortic stent, as pictured on the right side of Fig. A.2, which shows the fabricated RX prototype, already connected to the mm-size rectifier. Each wave of the metal coil is aligned with a node of the stent lattice, allowing for mechanical stability and conformal embedding. The final configuration envisages covering the cylindrical stent with three RX coils of this type, each equipped with its own rectifier. The three rectifiers are then meant to be cascaded at the DC level.

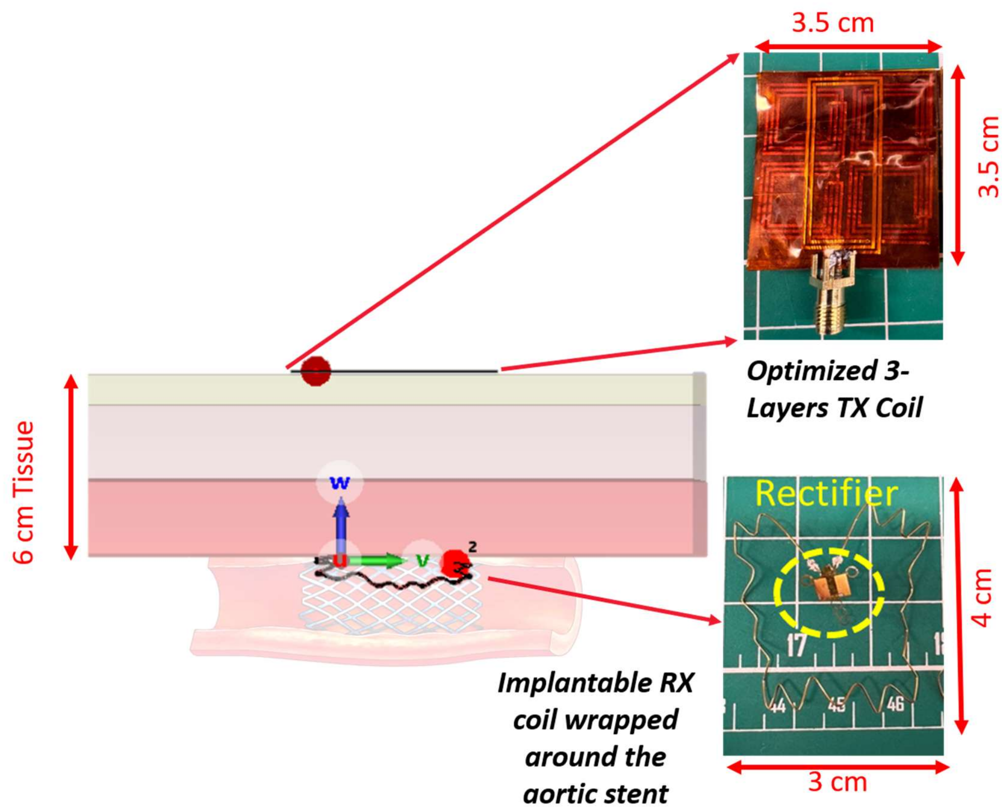

Figure A.2. Overview of the simulated inductive link consisting of: TX coil 2 mm above the skin surface, mimicking placement on textile fabrics, a 6-cm biological tissue slab between the TX and RX (1-mm-layer of skin, 10-mm-layer of fat, 25-mm-layer of muscle, and 25-mm-layer of blood), and the implanted RX coil wrapped around the stent. Highlighted are the pictures of the TX and RX fabricated prototypes, with RX connected to the rectifier, as meant to be realized for in-vivo testing.

In the EM simulations, TX and RX were separated by 6 cm of biological tissue, with the objective of maximizing the magnetic field at the RX location and, consequently, the deep-tissue penetration of the field reaching the RX center at 7 cm from the TX coil. Since the overall goal is to optimize the PTE of the inductive link, the power transfer from the RF source to the TX coil must also be maximized. To this end, two configurations were simulated in CST and compared: the first without impedance matching between the 50 Ω ports and the TX/RX coil impedances, and the second with matching conditions. In the matched case, the coils were brought to resonance using a lumped capacitor and the port impedance was set equal to the real part of the coil impedance, effectively simulating the inclusion of matching networks on both TX and RX sides to adapt their impedance to the 50 Ω characteristic ports of a VNA.

The comparison results, shown in Table A.2, demonstrate a significant improvement in deep-tissue magnetic field penetration when matching conditions are implemented: the average H-field at the RX position is 0.36 A/m with matching and resonance, versus 0.02 A/m without matching, highlighting the crucial role of proper resonance and impedance matching. Furthermore, the maximum simulated SAR is well below regulatory limits, with MAX SAR (10 g tissue) = 0.015 W/kg, compared to the IEEE and ICNIRP limits of 2 W/kg, respectively, ensuring safe operation of the system. These results correspond to an RF-to-RF PTE — computed as the squared magnitude of the S_{21} parameter from the EM-simulated S-matrix — of 0.11% under matched conditions. This value is consistent with those reported in the literature for similar implantation depths and frequencies, although further improvements are expected by fine-tuning the resonance capacitances to enhance impedance matching and coupling efficiency.

TABLE A.2

SIMULATED RF-TO-RF LINK COMPARISON WITH and WITHOUT MATCHING AT TX AND RX

Sim. Avg H field @RX No matching	**Sim. Avg H field @RX With matching**	**Sim. Max Avg H field (@TX location)**	**Sim. PTE % With matching at the ports**
0.02 A/m	0.36 A/m	95 A/m	0.11 %

A.3 Experimental Characterization of the Inductive Link in Air: Impact of TX Matching Conditions on RF-to-RF PTE

To experimentally validate the EM simulations and assess the effect of impedance matching on the overall RF-to-RF PTE, the TX and RX coils were measured in air using a VNA. The two coils were aligned face-to-face, and the RX coil was progressively moved away from the TX at distances of 1, 2, 3, 4, 5, 6, 8, and 10 cm. At each separation, the S-parameters were recorded. Measurements were repeated under two configurations, both featuring an RX coil tuned to resonance through a series capacitor and matched to the 50 Ω port of the VNA via a dedicated matching network

(MN). The TX coil, on the other hand, was either (i) left unmatched, or (ii) tuned to resonance and matched to 50 Ω.

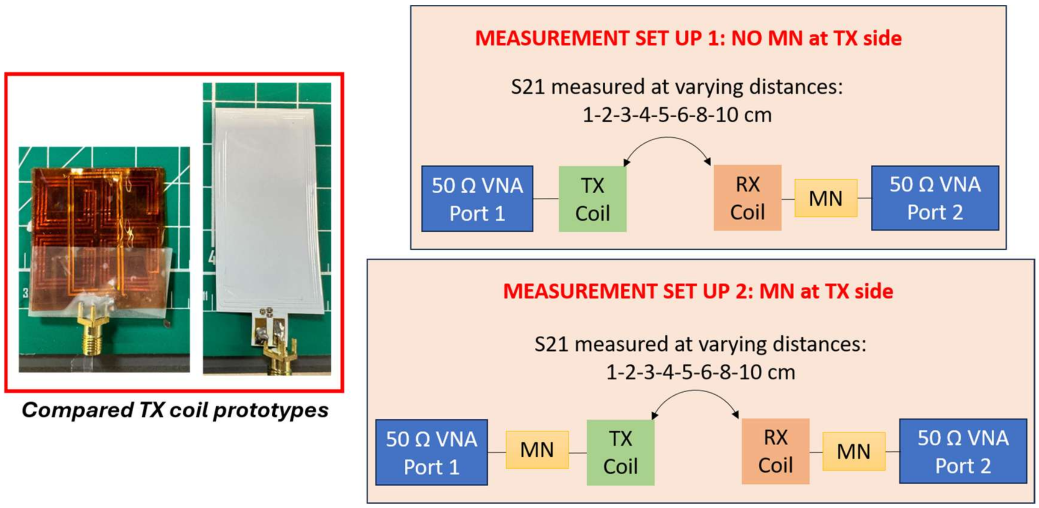

Figure A.3. Experimental setups to assess the effect of impedance matching on the overall RF-to-RF PTE. The S parameters of the inductive link in the two configurations (Setup 1 and Setup 2) were measured in air using a VNA. The same measurement procedure was repeated using the rectangular TX coil on the left side of the figure for comparative purposes.

The experimental setup is illustrated in Fig. A.3. Representative S-parameter results at TX–RX separations of 1 cm and 6 cm are shown in Figs. A.4(a) and (b), respectively. In both cases, the configuration including the TX matching network exhibits a markedly higher PTE, reaching 0.13% at 1 cm compared to only 0.004% without matching. The relatively low measured efficiencies are mainly attributed to the low Q factor of the RX coil, significantly lower than the simulated one, due to mechanical instability in the SMA connection between the coil and the matching network.

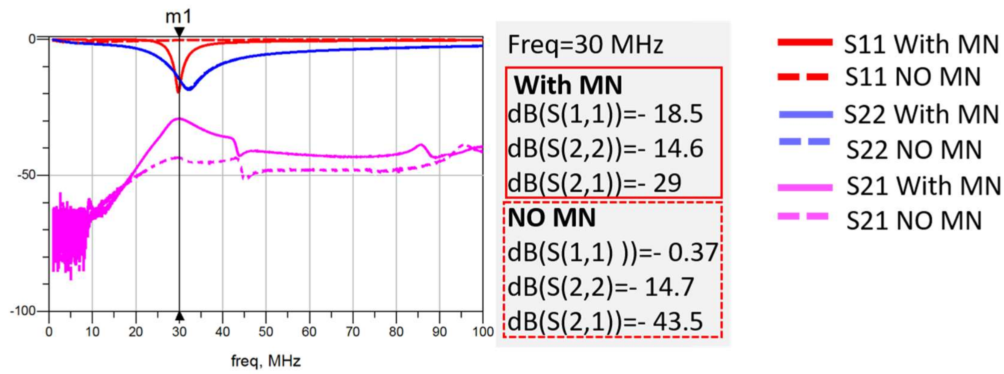
m1
0
-50
-100
0 10 20 30 40 50 60 70 80 90 100
freq, MHz
Freq=30 MHz
With MN
dB(S(1,1))=- 18.5
dB(S(2,2))=- 14.6
dB(S(2,1))=- 29
NO MN
dB(S(1,1)))=- 0.37
dB(S(2,2)=- 14.7
dB(S(2,1))=- 43.5
S11 With MN
S11 NO MN
S22 With MN
S22 NO MN
S21 With MN
S21 NO MN

(a)

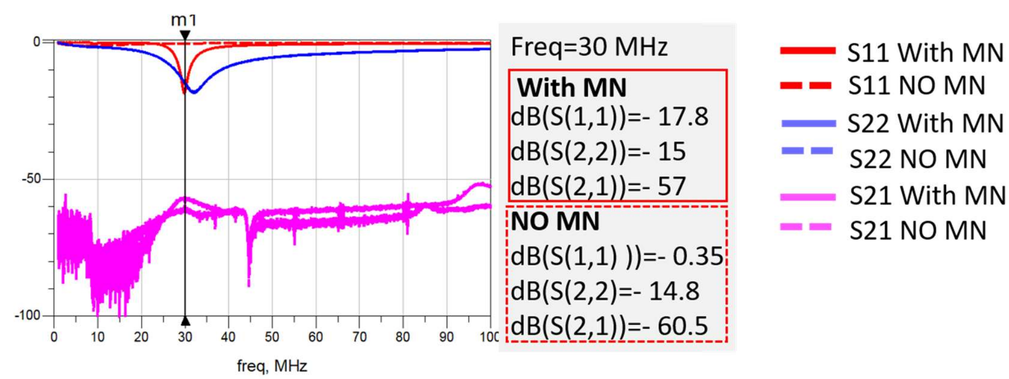
m1
0
-50
-100
0 10 20 30 40 50 60 70 80 90 100
freq, MHz
Freq=30 MHz
With MN
dB(S(1,1))=- 17.8
dB(S(2,2))=- 15
dB(S(2,1))=- 57
NO MN
dB(S(1,1)))=- 0.35
dB(S(2,2)=- 14.8
dB(S(2,1))=- 60.5
S11 With MN
S11 NO MN
S22 With MN
S22 NO MN
S21 With MN
S21 NO MN

(b)

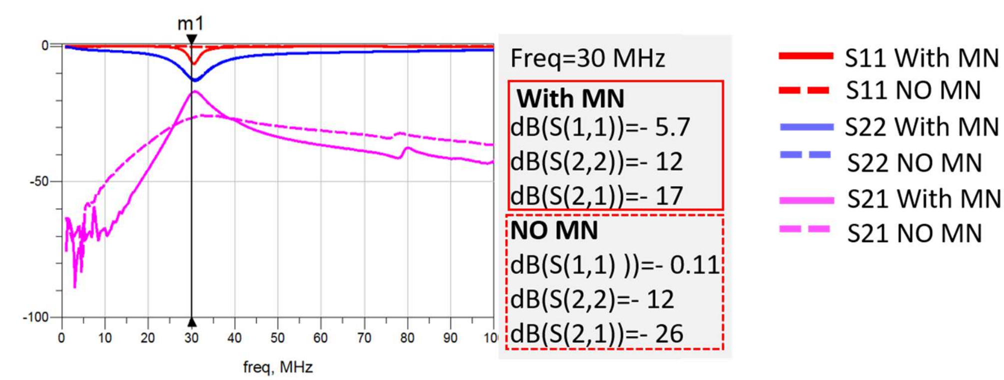
m1
0
-50
-100
0 10 20 30 40 50 60 70 80 90 10
freq, MHz
Freq=30 MHz
With MN
dB(S(1,1))=- 5.7
dB(S(2,2))=- 12
dB(S(2,1))=- 17
NO MN
dB(S(1,1)))=- 0.11
dB(S(2,2)=- 12
dB(S(2,1))=- 26
S11 With MN
S11 NO MN
S22 With MN
S22 NO MN
S21 With MN
S21 NO MN

(c)

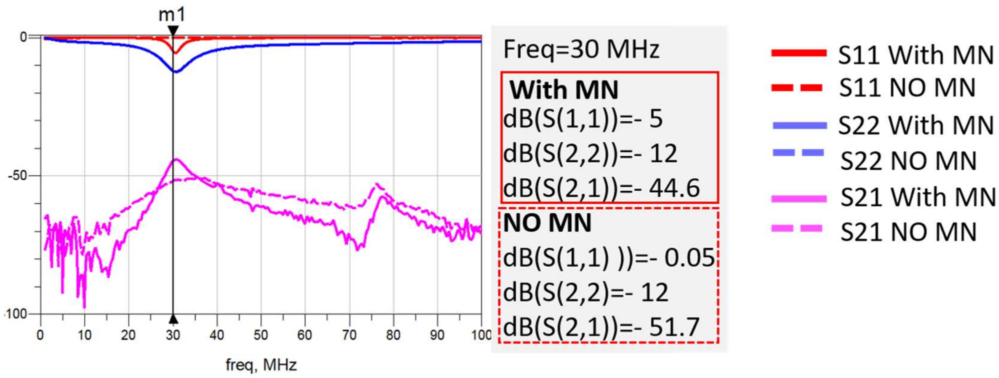

(d)

Figure A.4. Measured S-parameters for the two configurations (with and without TX matching) at representative distances of 1 cm and 6 cm for the 3-layers TX coil (a) and (b), and for the simple rectangular TX coil (c) and (d), respectively.

The same measurement procedure was repeated using a TX coil previously developed in Prof. Rogers' laboratory for comparative purposes. The coil is a simple rectangular three-turn structure (2.7×5.7 cm^2) fabricated on polyimide and encapsulated, as illustrated on the left side picture in Fig. A.3. Its measured quality factor and inductance at 30 MHz were $Q_{TX,30\ MHz} \approx 30$, $L_{TX,30\ MHz} \approx 3.57\,\mu$H, respectively. The measured S-parameters for the two configurations (with and without TX matching) at representative distances of 1 cm and 6 cm are reported in Fig. A.4(c) and (d), confirming once again the importance of impedance matching at the transmitter side. Specifically, the measured RF-to-RF PTE, computed as $|S_{21}|^2$, reaches 2% at 1 cm when the TX is matched, compared to only 0.03% without matching.

Finally, Figs. A.5 summarize the measured transmission coefficient S parameter (S_{21} (dB)) as a function of TX–RX distance for both TX coil types and the evaluation of the difference in S_{21} due to the introduction of the MN at the TX side, clearly illustrating the improvement achieved by this design choice. These results further support the hypothesis that optimizing TX matching is crucial to maximizing link efficiency and deep-field power transfer performance.

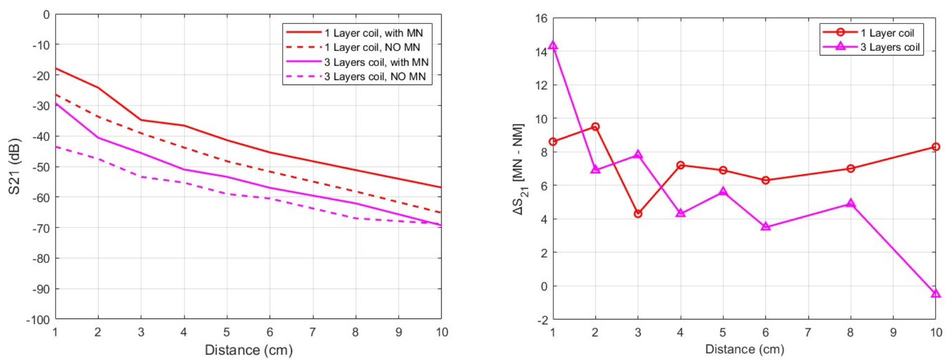

(a) (b)

Figure A.5. (a) Measured transmission coefficient (S_{21}) for the two configurations (with and without TX matching) as function of the distance, and (b) S21 difference in S_{21} due to the introduction of the MN at the TX side for the simple rectangular TX coil (pink line) and for the 3-layers TX coil (red line).

The measured PTE values are higher for the single rectangular TX coil, primarily due to its larger inductance (3.57 μH) compared to the three-layer miniaturized design. However, a more precise fabrication process for the multilayer coil is expected to significantly improve its performance, particularly by reducing connection losses and enhancing its quality factor. Moreover, given its compact and flexible architecture, the three-layer coil design is anticipated to achieve superior deep-tissue magnetic field penetration once fully optimized, making it more suitable for integration into wearable applications.

A.4 Conclusion and Future Work

This study presented the design, optimization, and preliminary validation of a miniaturized, flexible TX coil for efficient RF inductive power transfer through biological tissues. The proposed coil demonstrates the feasibility of compact, conformal TX structures capable of providing safe and efficient WPT across several centimeters of tissue while maintaining mechanical flexibility and adaptability for seamless integration into common garment fabrics. Simulation and measurement results confirm that careful impedance matching and resonance tuning are key to maximizing the RF-to-RF PTE and ensuring reliable operation under varying alignment conditions.

The optimized TX coil thus represents a promising step toward wearable-powered implantable biomedical systems, enabling reliable energy delivery across up to 6 cm of tissue. Its form factor and mechanical compliance allow for potential embedding in everyday clothing, paving the way for next-generation, unobtrusive, and energy-autonomous implantable devices.

Ongoing and future work will focus on several key directions:

- Refinement of TX coil matching networks: further optimization of the transmitter matching circuits to improve impedance matching and ensure stable, reproducible measurements.
- Evaluation of the stent's material impact: assessing how the tungsten mesh of the aortic stent affects the RX coil's electromagnetic characteristics and overall link efficiency.
- End-to-end RF-to-DC performance analysis: performing comprehensive measurements of the complete wireless power transfer link—including the RX rectifier and load—both in air and in water, to validate real-world energy delivery efficiency.

Collectively, these developments will support the realization of a fully functional wireless power transfer system capable of safe, efficient, and robust deep-tissue energy delivery for implantable biomedical applications.

Bibliography

[1] S.-Z. Liu, W.-T. Guo, X.-H. Zhao, X.-G. Tang, and Q.-J. Sun, "Self-powered sensing for health monitoring and robotics," *Soft Science*, vol. 5, no. 1, Feb. 2025, doi: 10.20517/ss.2024.65.

[2] P. P. Morita, K. S. Sahu, and A. Oetomo, "Health Monitoring Using Smart Home Technologies: Scoping Review," *JMIR Mhealth Uhealth*, vol. 11, p. e37347, Apr. 2023, doi: 10.2196/37347.

[3] S. Cheng *et al.*, "Recent Progress in Intelligent Wearable Sensors for Health Monitoring and Wound Healing Based on Biofluids," *Front Bioeng Biotechnol*, vol. 9, Nov. 2021, doi: 10.3389/fbioe.2021.765987.

[4] M. Wagih *et al.*, "Microwave-Enabled Wearables: Underpinning Technologies, Integration Platforms, and Next-Generation Roadmap," *IEEE Journal of Microwaves*, vol. 3, no. 1, pp. 193–226, Jan. 2023, doi: 10.1109/JMW.2022.3223254.

[5] R. K. Razack, N. M. Poovadichalil, and K. K. Sadasivuni, "Toward autonomous medicine: A comprehensive review of biomedical energy harvesting and wearable sensing systems," *Nano Energy*, vol. 145, p. 111422, Dec. 2025, doi: 10.1016/j.nanoen.2025.111422.

[6] J. Huang, Y. Zhou, Z. Ning, and H. Gharavi, "Wireless Power Transfer and Energy Harvesting: Current Status and Future Prospects," *IEEE Wirel Commun*, vol. 26, no. 4, pp. 163–169, Aug. 2019, doi: 10.1109/MWC.2019.1800378.

[7] A. Costanzo *et al.*, “Electromagnetic Energy Harvesting and Wireless Power Transmission: A Unified Approach,” *Proceedings of the IEEE*, vol. 102, no. 11, pp. 1692–1711, Nov. 2014, doi: 10.1109/JPROC.2014.2355261.

[8] J. Kim *et al.*, “Miniaturized Battery-Free Wireless Systems for Wearable Pulse Oximetry,” *Adv Funct Mater*, vol. 27, no. 1, Jan. 2017, doi: 10.1002/adfm.201604373.

[9] X. Huang *et al.*, “Epidermal radio frequency electronics for wireless power transfer,” *Microsyst Nanoeng*, vol. 2, no. 1, p. 16052, Oct. 2016, doi: 10.1038/micronano.2016.52.

[10] S. Il Park *et al.*, “Soft, stretchable, fully implantable miniaturized optoelectronic systems for wireless optogenetics,” *Nat Biotechnol*, vol. 33, no. 12, pp. 1280–1286, Dec. 2015, doi: 10.1038/nbt.3415.

[11] T. R. Ray *et al.*, “Bio-Integrated Wearable Systems: A Comprehensive Review,” *Chem Rev*, vol. 119, no. 8, pp. 5461–5533, Apr. 2019, doi: 10.1021/acs.chemrev.8b00573.

[12] H. B. Mamo, M. Adamiak, and A. Kunwar, “3D printed biomedical devices and their applications: A review on state-of-the-art technologies, existing challenges, and future perspectives,” *J Mech Behav Biomed Mater*, vol. 143, p. 105930, Jul. 2023, doi: 10.1016/j.jmbbm.2023.105930.

[13] E. Augello, G. Battistini, G. Paolini, S. Bastianini, G. Zoccoli, and A. Costanzo, “A Conformal Wireless Power System for Battery-Free Implantable Optogenetic Treatment of Obstructive Sleep Apnea,” in

2023 IEEE MTT-S International Microwave Biomedical Conference (IMBioC), 2023, pp. 166–168. doi: 10.1109/IMBioC56839.2023.10305122.

[14] G. Battistini *et al.*, "Soft, Implantable, Battery-Free, and Wirelessly Controlled Optoelectronic System for Obstructive Sleep Apnea Treatment," in *2024 IEEE MTT-S International Microwave Biomedical Conference (IMBioC)*, 2024, pp. 87–89. doi: 10.1109/IMBioC60287.2024.10590109.

[15] G. Battistini, E. Augello, G. Paolini, D. Masotti, and A. Costanzo, "Advancing Obstructive Sleep Apnea Therapy: a Miniaturized Wireless Implant for Battery-Free Optogenetic Neurostimulation in Mice," in *2025 IEEE Wireless Power Technology Conference and Expo (WPTCE)*, 2025, pp. 1–4. doi: 10.1109/WPTCE62521.2025.11062271.

[16] K. W. Cho *et al.*, "Soft Bioelectronics Based on Nanomaterials," *Chem Rev*, vol. 122, no. 5, pp. 5068–5143, Mar. 2022, doi: 10.1021/acs.chemrev.1c00531.

[17] D.-H. Kim, N. Lu, Y. Huang, and J. A. Rogers, "Materials for stretchable electronics in bioinspired and biointegrated devices," *MRS Bull*, vol. 37, no. 3, pp. 226–235, Mar. 2012, doi: 10.1557/mrs.2012.36.

[18] Y.-S. Kim, A. Basir, R. Herbert, J. Kim, H. Yoo, and W.-H. Yeo, "Soft Materials, Stretchable Mechanics, and Optimized Designs for Body-Wearable Compliant Antennas," *ACS Appl Mater Interfaces*, vol. 12, no. 2, pp. 3059–3067, Jan. 2020, doi: 10.1021/acsami.9b20233.

[19] S. Nappi, C. J. Su, H. Luan, J. A. Rogers, and G. Marrocco, "Stretchable Wireless Sensor Skin for the Surface Monitoring of Soft Objects," in *2020 IEEE International Conference on Flexible and Printable Sensors and Systems (FLEPS)*, IEEE, Aug. 2020, pp. 1–4. doi: 10.1109/FLEPS49123.2020.9239524.

[20] A. M. Hussain, F. A. Ghaffar, S. I. Park, J. A. Rogers, A. Shamim, and M. M. Hussain, "Metal/Polymer Based Stretchable Antenna for Constant Frequency Far-Field Communication in Wearable Electronics," *Adv Funct Mater*, vol. 25, no. 42, pp. 6565–6575, Nov. 2015, doi: 10.1002/adfm.201503277.

[21] S. Il Park *et al.*, "Stretchable multichannel antennas in soft wireless optoelectronic implants for optogenetics," *Proceedings of the National Academy of Sciences*, vol. 113, no. 50, Dec. 2016, doi: 10.1073/pnas.1611769113.

[22] T. Chang *et al.*, "A General Strategy for Stretchable Microwave Antenna Systems using Serpentine Mesh Layouts," *Adv Funct Mater*, vol. 27, no. 46, Dec. 2017, doi: 10.1002/adfm.201703059.

[23] A. Costanzo, E. Augello, G. Battistini, F. Benassi, D. Masotti, and G. Paolini, "Microwave Devices for Wearable Sensors and IoT," *Sensors*, vol. 23, no. 9, 2023, doi: 10.3390/s23094356.

[24] Y. Kim and S. Lim, "Low Loss Substrate-Integrated Waveguide Using 3D-Printed Non-Uniform Honeycomb-Shaped Material," *IEEE Access*, vol. 8, pp. 191090–191099, 2020, doi: 10.1109/ACCESS.2020.3032132.

[25] H. Ijaz, W. Saleem, M. Zain-ul-Abdein, T. Mabrouki, S. Rubaiee, and A. Salmeen Bin Mahfouz, "Finite Element Analysis of Bend Test of Sandwich Structures Using Strain Energy Based Homogenization Method," *Advances in Materials Science and Engineering*, vol. 2017, pp. 1–10, 2017, doi: 10.1155/2017/8670207.

[26] G. Battistini, G. Paolini, A. Costanzo, and D. Masotti, "A Novel 3-D Printed Dual-Port Rectenna for Simultaneous Energy Harvesting and Backscattering of a Passively Generated UWB Pulse," *IEEE Trans Microw Theory Tech*, vol. 72, no. 1, pp. 812–821, 2024, doi: 10.1109/TMTT.2023.3322744.

[27] G. Battistini, G. Paolini, A. Costanzo, and D. Masotti, "3D-Printable Rectenna for Passive Tag Localization Exploiting Multi-Sine Intermodulation," in *2023 IEEE/MTT-S International Microwave Symposium - IMS 2023*, 2023, pp. 1077–1080. doi: 10.1109/IMS37964.2023.10188103.

[28] G. Battistini, G. Paolini, D. Masotti, and A. Costanzo, "Wearable Coplanar-Fed 2.45 GHz-Rectenna on a Flexible 3D-Printable Low-Cost Substrate," in *2022 52nd European Microwave Conference (EuMC)*, 2022, pp. 72–75. doi: 10.23919/EuMC54642.2022.9924432.

[29] G. Battistini, G. Paolini, D. Masotti, and A. Costanzo, "Innovative 3-D Printing Processing Techniques for Flexible and Wearable Planar Rectennas," in *2022 Wireless Power Week (WPW)*, 2022, pp. 294–297. doi: 10.1109/WPW54272.2022.9853929.

[30] G. Battistini, G. Paolini, D. Masotti, and A. Costanzo, “3-D Etching Techniques for Low-Cost Wearable Microwave Devices in Grounded Coplanar Waveguide,” in *2022 IEEE MTT-S International Microwave Biomedical Conference (IMBioC)*, 2022, pp. 63–65. doi: 10.1109/IMBioC52515.2022.9790168.

[31] A. Costanzo, D. Masotti, G. Paolini, and D. Schreurs, “Evolution of SWIPT for the IoT World: Near- and Far-Field Solutions for Simultaneous Wireless Information and Power Transfer,” *IEEE Microw Mag*, vol. 22, no. 12, pp. 48–59, Dec. 2021, doi: 10.1109/MMM.2021.3109554.

[32] Z. Liu, J. Wang, E. G. Lim, Z. Wang, R. Pei, and W. Zhang, “A Review on Simultaneous Wireless Information and Power Transmission: Approaches and Designs,” in *2024 IEEE International Symposium on Radio-Frequency Integration Technology (RFIT)*, IEEE, Aug. 2024, pp. 1–3. doi: 10.1109/RFIT60557.2024.10812459.

[33] G. Paolini, M. Feliciani, D. Masotti, and A. Costanzo, “Toward an Energy-Autonomous Wearable System for Human Breath Detection,” in *2020 IEEE MTT-S International Microwave Biomedical Conference (IMBioC)*, IEEE, Dec. 2020, pp. 1–3. doi: 10.1109/IMBIoC47321.2020.9385027.

[34] G. Paolini, A. Quddious, D. Chatzichristodoulou, D. Masotti, S. Nikolaou, and A. Costanzo, “An Energy-Autonomous SWIPT RFID Tag for Communication in the 2.4 GHz ISM Band,” in *2022 3rd URSI*

Atlantic and Asia Pacific Radio Science Meeting (AT-AP-RASC), 2022, pp. 1–4. doi: 10.23919/AT-AP-RASC54737.2022.9814385.

[35] G. Paolini, G. Battistini, D. Masotti, S. Scanzio, G. Cena, and A. Costanzo, "Design of a Dual-Band Tri-Port Tag for Near-Field Energy Harvesting and Far-Field SWIPT," in *Proceedings of the 7th URSI Asia-Pacific RadioScience Conference – AP-RASC 2025*, Gent, Belgium: URSI – International Union of Radio Science, 2025. doi: 10.46620/URSIAPRASC25/RLBM4690.

[36] G. Paolini, F. Benassi, G. Battistini, E. Augello, D. Masotti, and A. Costanzo, "A Tri-Port Wearable Tag for Indoor Communication with Power Delivery through Near-Field and Far-Field Energy Harvesting," in *IEEE International Conference on RFID Technology and Applications*, Valence, France, Oct. 2025.

[37] G. Battistini, G. Paolini, D. Masotti, and A. Costanzo, "Revisiting Antenna Topology for Wearable RFID Tags on Lossy Dielectric Substrates," in *2025 IEEE International Conference on RFID Technology and Applications – RFID-TA 2025*, Valence, France, Oct. 2025.

[38] G. Paolini *et al.*, "Wireless power transfer-enabled optogenetic stimulation of hypoglossal motoneurons in mice for functional studies in obstructive sleep apnea," in *IEEE Journal of Microwaves*, 2025.

[39] L. Spicuzza, D. Caruso, and G. Di Maria, "Obstructive sleep apnoea syndrome and its management," *Ther Adv Chronic Dis*, vol. 6, no. 5, pp. 273–285, 2015, doi: 10.1177/2040622315590318.

[40] B. M. Doyle *et al.*, “Gene delivery to the hypoglossal motor system: preclinical studies and translational potential,” *Gene Ther*, vol. 28, no. 7, pp. 402–412, 2021, doi: 10.1038/s41434-021-00225-1.

[41] T. D. Bradley and J. S. Floras, “Obstructive sleep apnoea and its cardiovascular consequences,” *The Lancet*, vol. 373, no. 9657, pp. 82–93, 2009, doi: https://doi.org/10.1016/S0140-6736(08)61622-0.

[42] J. S. Virk and B. Kotecha, “When continuous positive airway pressure (CPAP) fails,” *J Thorac Dis*, vol. 8, no. 10, pp. E1112–E1121, Oct. 2016, doi: 10.21037/jtd.2016.09.67.

[43] “Mayo Clinic, ‘Obstructive sleep apnea,’ Mayo Clinic Website. [Online]. Available: https://www.mayoclinic.org.”

[44] M. Jaradat and A. Rahhal, “Obstructive Sleep Apnea, Prevalence, Etiology & Role of Dentist & Oral Appliances in Treatment: Review Article,” *Open J Stomatol*, vol. 05, no. 07, pp. 187–201, 2015, doi: 10.4236/ojst.2015.57024.

[45] M. A. Arachchige and J. Steier, “Beyond Usual Care: A Multidisciplinary Approach Towards the Treatment of Obstructive Sleep Apnoea,” *Front Cardiovasc Med*, vol. 8, Jan. 2022, doi: 10.3389/fcvm.2021.747495.

[46] M. D. Olson and M. R. Junna, “Hypoglossal Nerve Stimulation Therapy for the Treatment of Obstructive Sleep Apnea,” *Neurotherapeutics*, vol. 18, no. 1, pp. 91–99, Jan. 2021, doi: 10.1007/s13311-021-01012-x.

[47] A. Costantino *et al.*, "Hypoglossal nerve stimulation long-term clinical outcomes: a systematic review and meta-analysis," *Sleep and Breathing*, vol. 24, no. 2, pp. 399–411, Jun. 2020, doi: 10.1007/s11325-019-01923-2.

[48] P. R. Eastwood *et al.*, "Bilateral hypoglossal nerve stimulation for treatment of adult obstructive sleep apnoea," *European Respiratory Journal*, vol. 55, no. 1, p. 1901320, Jan. 2020, doi: 10.1183/13993003.01320-2019.

[49] S. Jiang, X. Wu, N. J. Rommelfanger, Z. Ou, and G. Hong, "Shedding light on neurons: optical approaches for neuromodulation," *Natl Sci Rev*, vol. 9, no. 10, Sep. 2022, doi: 10.1093/nsr/nwac007.

[50] G. Spagnuolo, F. Genovese, L. Fortunato, M. Simeone, C. Rengo, and M. Tatullo, "The Impact of Optogenetics on Regenerative Medicine," *Applied Sciences*, vol. 10, no. 1, p. 173, Dec. 2019, doi: 10.3390/app10010173.

[51] P. Mahmoudi, H. Veladi, and F. Pakdel, "Optogenetics, Tools and Applications in Neurobiology," *J Med Signals Sens*, vol. 7, no. 2, p. 71, 2017, doi: 10.4103/2228-7477.205506.

[52] S. Alvente, G. Matteoli, E. Miglioranza, G. Zoccoli, and S. Bastianini, "How to study sleep apneas in mouse models of human pathology," *J Neurosci Methods*, vol. 395, p. 109923, Jul. 2023, doi: 10.1016/j.jneumeth.2023.109923.

[53] A. M. Aravanis *et al.*, "An optical neural interface: *in vivo* control of rodent motor cortex with integrated fiberoptic and optogenetic

technology," *J Neural Eng*, vol. 4, no. 3, pp. S143–S156, Sep. 2007, doi: 10.1088/1741-2560/4/3/S02.

[54] P. Silva and L. Jacinto, "Wireless Devices for Optical Brain Stimulation: A Review of Current Developments for Optogenetic Applications in Freely Moving Mice," *Cell Mol Bioeng*, vol. 18, no. 1, pp. 1–13, Feb. 2025, doi: 10.1007/s12195-024-00832-z.

[55] M. A. Rossi, V. Go, T. Murphy, Q. Fu, J. Morizio, and H. H. Yin, "A wirelessly controlled implantable LED system for deep brain optogenetic stimulation," *Front Integr Neurosci*, vol. Volume 9-2015, 2015, doi: 10.3389/fnint.2015.00008.

[56] C. Y. Kim *et al.*, "Soft subdermal implant capable of wireless battery charging and programmable controls for applications in optogenetics," *Nat Commun*, vol. 12, no. 1, p. 535, 2021, doi: 10.1038/s41467-020-20803-y.

[57] Y. Yang *et al.*, "Wireless multilateral devices for optogenetic studies of individual and social behaviors," *Nat Neurosci*, vol. 24, no. 7, pp. 1035–1045, 2021, doi: 10.1038/s41593-021-00849-x.

[58] G. Shin *et al.*, "Flexible Near-Field Wireless Optoelectronics as Subdermal Implants for Broad Applications in Optogenetics," *Neuron*, vol. 93, no. 3, pp. 509-521.e3, Feb. 2017, doi: 10.1016/j.neuron.2016.12.031.

[59] J. Ausra *et al.*, "Wireless, battery-free, subdermally implantable platforms for transcranial and long-range optogenetics in freely moving

animals," *Proceedings of the National Academy of Sciences*, vol. 118, no. 30, Jul. 2021, doi: 10.1073/pnas.2025775118.

[60] R. B. Berry *et al.*, "Rules for Scoring Respiratory Events in Sleep: Update of the 2007 AASM Manual for the Scoring of Sleep and Associated Events," *Journal of Clinical Sleep Medicine*, vol. 08, no. 05, pp. 597–619, Oct. 2012, doi: 10.5664/jcsm.2172.

[61] C. Baumgartner *et al.*, "IT'IS Database for Thermal and Electromagnetic Parameters of Biological Tissues, Version 5.0." Accessed: Oct. 03, 2025. [Online]. Available: https://itis.swiss/virtual-population/tissue-properties/database/dielectric-properties . doi: 10.13099/VIP21000-05-0.

[62] A. Pacini, F. Mastri, R. Trevisan, A. Costanzo, and D. Masotti, "Theoretical and experimental characterization of moving wireless power transfer systems," in *2016 10th European Conference on Antennas and Propagation (EuCAP)*, 2016, pp. 1–4. doi: 10.1109/EuCAP.2016.7481913.

[63] A. P. Sample, D. T. Meyer, and J. R. Smith, "Analysis, Experimental Results, and Range Adaptation of Magnetically Coupled Resonators for Wireless Power Transfer," *IEEE Transactions on Industrial Electronics*, vol. 58, no. 2, pp. 544–554, 2011, doi: 10.1109/TIE.2010.2046002.

[64] D. Ahn and S. Hong, "Effect of Coupling Between Multiple Transmitters or Multiple Receivers on Wireless Power Transfer," *IEEE*

Transactions on Industrial Electronics, vol. 60, no. 7, pp. 2602–2613, 2013, doi: 10.1109/TIE.2012.2196902.

[65] R. de Sousa Costa, N. Ventura, T. de Andrade Lourenção Freddi, L. C. H. da Cruz, and D. G. Corrêa, "The Hypoglossal Nerve," *Seminars in Ultrasound, CT and MRI*, vol. 44, no. 2, pp. 104–114, Apr. 2023, doi: 10.1053/j.sult.2022.11.002.

[66] George. Paxinos and K. B. J. . Franklin, *Paxinos and Franklin's The mouse brain in stereotaxic coordinates*. Academic Press, an imprint of Elsevier, 2019.

[67] O. Dergacheva, T. Fleury-Curado, V. Y. Polotsky, M. Kay, V. Jain, and D. Mendelowitz, "GABA and glycine neurons from the ventral medullary region inhibit hypoglossal motoneurons," *Sleep*, vol. 43, no. 6, Jun. 2020, doi: 10.1093/sleep/zsz301.

[68] J. A. Aggarwal, W.-Y. Liu, G. Montandon, H. Liu, S. W. Hughes, and R. L. Horner, "Measurement and State-Dependent Modulation of Hypoglossal Motor Excitability and Responsivity In-Vivo," *Sci Rep*, vol. 10, no. 1, p. 550, Jan. 2020, doi: 10.1038/s41598-019-57328-4.

[69] T. Whittaker, S. Zhang, A. Powell, C. J. Stevens, J. Y. C. Vardaxoglou, and W. Whittow, "3D Printing Materials and Techniques for Antennas and Metamaterials: A survey of the latest advances," *IEEE Antennas Propag Mag*, vol. 65, no. 3, pp. 10–20, 2023, doi: 10.1109/MAP.2022.3229298.

[70] K. J. Herrick, T. A. Schwarz, and L. P. B. Katehi, "Si-micromachined coplanar waveguides for use in high-frequency circuits," *IEEE Trans*

Microw Theory Tech, vol. 46, no. 6, pp. 762–768, 1998, doi: 10.1109/22.681198.

[71] M. Palandoken, C. Murat, A. Kaya, and B. Zhang, "A Novel 3-D Printed Microwave Probe for ISM Band Ablation Systems of Breast Cancer Treatment Applications," *IEEE Trans Microw Theory Tech*, vol. 70, no. 3, pp. 1943–1953, 2022, doi: 10.1109/TMTT.2021.3138734.

[72] D. Masotti, A. Costanzo, M. Del Prete, and V. Rizzoli, "Genetic-based design of a tetra-band high-efficiency radio-frequency energy harvesting system," *IET Microwaves, Antennas & Propagation*, vol. 7, no. 15, pp. 1254–1263, Dec. 2013, doi: 10.1049/iet-map.2013.0056.

[73] V. S. Shilimkar and A. Weisshaar, "Modeling of Metal-Fill Parasitic Capacitance and Application to On-Chip Slow-Wave Structures," *IEEE Trans Microw Theory Tech*, vol. 65, no. 5, pp. 1456–1464, May 2017, doi: 10.1109/TMTT.2016.2647242.

[74] A. Goulas *et al.*, "The Impact of 3D Printing Process Parameters on the Dielectric Properties of High Permittivity Composites," *Designs (Basel)*, vol. 3, no. 4, 2019, doi: 10.3390/designs3040050.

[75] V. Rizzoli, "Resonance Measurement of Single- and Coupled-Microstrip Propagation Constants," *IEEE Trans Microw Theory Tech*, vol. 25, no. 2, pp. 113–120, 1977, doi: 10.1109/TMTT.1977.1129050.

[76] A. Costanzo, F. Donzelli, D. Masotti, and V. Rizzoli, "Rigorous design of RF multi-resonator power harvesters," *Proceedings of the Fourth European Conference on Antennas and Propagation*, pp. 1–4, 2010,

[Online]. Available: https://api.semanticscholar.org/CorpusID:21363119

[77] K.-P. Latti, M. Kettunen, J.-P. Strom, and P. Silventoinen, “A Review of Microstrip T-Resonator Method in Determining the Dielectric Properties of Printed Circuit Board Materials,” *IEEE Trans Instrum Meas*, vol. 56, no. 5, pp. 1845–1850, Oct. 2007, doi: 10.1109/TIM.2007.903587.

[78] G. Boussatour, P.-Y. Cresson, B. Genestie, N. Joly, and T. Lasri, “Dielectric Characterization of Polylactic Acid Substrate in the Frequency Band 0.5–67 GHz,” *IEEE Microwave and Wireless Components Letters*, vol. 28, no. 5, pp. 374–376, May 2018, doi: 10.1109/LMWC.2018.2812642.

[79] S. Zhang, C. C. Njoku, W. G. Whittow, and J. C. Vardaxoglou, “Novel 3D printed synthetic dielectric substrates,” *Microw Opt Technol Lett*, vol. 57, no. 10, pp. 2344–2346, 2015, doi: https://doi.org/10.1002/mop.29324.

[80] A. Costanzo and D. Masotti, “Smart Solutions in Smart Spaces: Getting the Most from Far-Field Wireless Power Transfer,” *IEEE Microw Mag*, vol. 17, no. 5, pp. 30–45, 2016, doi: 10.1109/MMM.2016.2525119.

[81] H. Heidari, O. Onireti, R. Das, and M. Imran, “Energy Harvesting and Power Management for IoT Devices in the 5G Era,” *IEEE Communications Magazine*, vol. 59, no. 9, pp. 91–97, 2021, doi: 10.1109/MCOM.101.2100487.

[82] Y. Wei *et al.*, “A Multiband, Polarization-Controlled Metasurface Absorber for Electromagnetic Energy Harvesting and Wireless Power Transfer,” *IEEE Trans Microw Theory Tech*, vol. 70, no. 5, pp. 2861–2871, 2022, doi: 10.1109/TMTT.2022.3155718.

[83] F. Zafari, A. Gkelias, and K. K. Leung, “A Survey of Indoor Localization Systems and Technologies,” *IEEE Communications Surveys & Tutorials*, vol. 21, no. 3, pp. 2568–2599, 2019, doi: 10.1109/COMST.2019.2911558.

[84] D. Dardari, R. D’Errico, C. Roblin, A. Sibille, and M. Z. Win, “Ultrawide Bandwidth RFID: The Next Generation?,” *Proceedings of the IEEE*, vol. 98, no. 9, pp. 1570–1582, 2010, doi: 10.1109/JPROC.2010.2053015.

[85] J. Aliasgari, P. Fathi, M. Forouzandeh, and N. Karmakar, “IR-UWB Chipless RFID Reader Based on Frequency Translation Technique for Decoding Frequency-Coded Tags,” *IEEE Trans Instrum Meas*, vol. 70, pp. 1–11, 2021, doi: 10.1109/TIM.2021.3094239.

[86] A. Costanzo, D. Masotti, M. Fantuzzi, and M. Del Prete, “Co-Design Strategies for Energy-Efficient UWB and UHF Wireless Systems,” *IEEE Trans Microw Theory Tech*, vol. 65, no. 5, pp. 1852–1863, 2017, doi: 10.1109/TMTT.2017.2675882.

[87] Q. Zhang *et al.*, “Bioinspired engineering of honeycomb structure – Using nature to inspire human innovation,” *Prog Mater Sci*, vol. 74, pp. 332–400, 2015, doi: https://doi.org/10.1016/j.pmatsci.2015.05.001.

[88] M. Zou, S. Xu, C. Wei, H. Wang, and Z. Liu, “A bionic method for the crashworthiness design of thin-walled structures inspired by bamboo,” *Thin-Walled Structures*, vol. 101, pp. 222–230, 2016, doi: https://doi.org/10.1016/j.tws.2015.12.023.

[89] L. Li, C. Guo, Y. Chen, and Y. Chen, “Optimization design of lightweight structure inspired by glass sponges (Porifera, Hexacinellida) and its mechanical properties,” *Bioinspir Biomim*, vol. 15, no. 3, p. 036006, Mar. 2020, doi: 10.1088/1748-3190/ab6ca9.

[90] F. E. Sezgin, M. Tanoğlu, O. Ö. Eğilmez, and C. Dönmez, “Mechanical Behavior of Polypropylene-based Honeycomb-Core Composite Sandwich Structures,” *Journal of Reinforced Plastics and Composites*, vol. 29, no. 10, pp. 1569–1579, May 2010, doi: 10.1177/0731684409341674.

[91] P. Lu, C. Song, and K. M. Huang, “A Two-Port Multipolarization Rectenna With Orthogonal Hybrid Coupler for Simultaneous Wireless Information and Power Transfer (SWIPT),” *IEEE Trans Antennas Propag*, vol. 68, no. 10, pp. 6893–6905, 2020, doi: 10.1109/TAP.2020.2993096.

[92] S. Shen, C.-Y. Chiu, and R. D. Murch, “A Dual-Port Triple-Band L-Probe Microstrip Patch Rectenna for Ambient RF Energy Harvesting,” *IEEE Antennas Wirel Propag Lett*, vol. 16, pp. 3071–3074, 2017, doi: 10.1109/LAWP.2017.2761397.

[93] M. Wagih, G. S. Hilton, A. S. Weddell, and S. Beeby, “Dual-Band Dual-Mode Textile Antenna/Rectenna for Simultaneous Wireless

Information and Power Transfer (SWIPT)," *IEEE Trans Antennas Propag*, vol. 69, no. 10, pp. 6322–6332, 2021, doi: 10.1109/TAP.2021.3070230.

[94] M. Fantuzzi, D. Masotti, and A. Costanzo, "A Novel Integrated UWB–UHF One-Port Antenna for Localization and Energy Harvesting," *IEEE Trans Antennas Propag*, vol. 63, no. 9, pp. 3839–3848, Sep. 2015, doi: 10.1109/TAP.2015.2452969.

[95] A. Boaventura, D. Belo, R. Fernandes, A. Collado, A. Georgiadis, and N. B. Carvalho, "Boosting the Efficiency: Unconventional Waveform Design for Efficient Wireless Power Transfer," *IEEE Microw Mag*, vol. 16, no. 3, pp. 87–96, Apr. 2015, doi: 10.1109/MMM.2014.2388332.

[96] N. Decarli, M. Del Prete, D. Masotti, D. Dardari, and A. Costanzo, "High-Accuracy Localization of Passive Tags With Multisine Excitations," *IEEE Trans Microw Theory Tech*, vol. 66, no. 12, pp. 5894–5908, 2018, doi: 10.1109/TMTT.2018.2879806.

[97] C.-K. Lee *et al.*, "Evaluation of Microwave Characterization Methods for Additively Manufactured Materials," *Designs (Basel)*, vol. 3, no. 4, 2019, doi: 10.3390/designs3040047.

[98] A. Sihvola, "Mixing Rules with Complex Dielectric Coefficients," *Subsurface Sensing Technologies and Applications*, vol. 1, no. 4, pp. 393–415, Oct. 2000, doi: 10.1023/A:1026511515005.

[99] L. A. Yimdjo Poffelie, P. J. Soh, S. Yan, and G. A. E. Vandenbosch, "A High-Fidelity All-Textile UWB Antenna With Low Back Radiation

for Off-Body WBAN Applications," *IEEE Trans Antennas Propag*, vol. 64, no. 2, pp. 757–760, Feb. 2016, doi: 10.1109/TAP.2015.2510035.

[100] F. Benassi, G. Paolini, D. Masotti, and A. Costanzo, "A Wearable Flexible Energy-Autonomous Filtenna for Ethanol Detection at 2.45 GHz," *IEEE Trans Microw Theory Tech*, vol. 69, no. 9, pp. 4093–4106, 2021, doi: 10.1109/TMTT.2021.3074155.

[101] G. Paolini *et al.*, "RF-Powered Low-Energy Sensor Nodes for Predictive Maintenance in Electromagnetically Harsh Industrial Environments," *Sensors*, vol. 21, no. 2, p. 386, Jan. 2021, doi: 10.3390/s21020386.

[102] A. Pacini, F. Benassi, D. Masotti, and A. Costanzo, "Design of a RF-to-dc Link for in-body IR-WPT with a Capsule-shaped Rotation-insensitive Receiver," Oct. 2018, pp. 1289–1292. doi: 10.1109/MWSYM.2018.8439499.

[103] L. Yang, L. J. Martin, D. Staiculescu, C. P. Wong, and M. M. Tentzeris, "Conformal Magnetic Composite RFID for Wearable RF and Bio-Monitoring Applications," *IEEE Trans Microw Theory Tech*, vol. 56, no. 12, pp. 3223–3230, Dec. 2008, doi: 10.1109/TMTT.2008.2006810.

[104] M. Mantash, A.-C. Tarot, S. Collardey, and K. Mahdjoubi, "Investigation of Flexible Textile Antennas and AMC Reflectors," *Int J Antennas Propag*, vol. 2012, pp. 1–10, 2012, doi: 10.1155/2012/236505.

[105] G. Monti, L. Corchia, and L. Tarricone, “UHF Wearable Rectenna on Textile Materials,” *IEEE Trans Antennas Propag*, vol. 61, no. 7, pp. 3869–3873, Jul. 2013, doi: 10.1109/TAP.2013.2254693.

[106] G. Paolini, D. Masotti, and A. Costanzo, “Wearable RFID Tag on Denim Substrate for Indoor Localization Applications,” *2019 49th European Microwave Conference (EuMC)*, pp. 504–507, 2019, [Online]. Available: https://api.semanticscholar.org/CorpusID:208281015

[107] K. Niotaki *et al.*, “RF Energy Harvesting and Wireless Power Transfer for Energy Autonomous Wireless Devices and RFIDs,” *IEEE Journal of Microwaves*, vol. 3, no. 2, pp. 763–782, Apr. 2023, doi: 10.1109/JMW.2023.3255581.

[108] K. Koski, L. Sydanheimo, Y. Rahmat-Samii, and L. Ukkonen, “Fundamental Characteristics of Electro-Textiles in Wearable UHF RFID Patch Antennas for Body-Centric Sensing Systems,” *IEEE Trans Antennas Propag*, vol. 62, no. 12, pp. 6454–6462, Dec. 2014, doi: 10.1109/TAP.2014.2364071.

[109] D. Le, S. Ahmed, L. Ukkonen, and T. Bjorninen, “A Small All-Corners-Truncated Circularly Polarized Microstrip Patch Antenna on Textile Substrate for Wearable Passive UHF RFID Tags,” *IEEE Journal of Radio Frequency Identification*, vol. 5, no. 2, pp. 106–112, Jun. 2021, doi: 10.1109/JRFID.2021.3073457.

[110] C. A. . Balanis, *Antenna theory : analysis and design.* John Wiley, 2016.

[111] D. M. . Pozar, *Microwave engineering.* John Wiley & Sons Incorporated, 2013.

[112] B. A. P. Nel, A. K. Skrivervik, and M. Gustafsson, "Radiation Efficiency and Gain Bounds for Microstrip Patch Antennas," *IEEE Trans Antennas Propag*, vol. 73, no. 2, pp. 873–883, Feb. 2025, doi: 10.1109/TAP.2024.3514318.

[113] Y. Zeng, D. Qiu, X. Meng, B. Zhang, and S. C. Tang, "Optimized Design of Coils for Wireless Power Transfer in Implanted Medical Devices," *IEEE J Electromagn RF Microw Med Biol*, vol. 2, no. 4, pp. 277–285, Dec. 2018, doi: 10.1109/JERM.2018.2863955.

[114] I. Habibagahi, J. Jang, and A. Babakhani, "Miniaturized Wirelessly Powered and Controlled Implants for Multisite Stimulation," *IEEE Trans Microw Theory Tech*, vol. 71, no. 5, pp. 1911–1922, May 2023, doi: 10.1109/TMTT.2022.3233368.

[115] H. Lyu *et al.*, "Synchronized Biventricular Heart Pacing in a Closed-chest Porcine Model based on Wirelessly Powered Leadless Pacemakers," *Sci Rep*, vol. 10, no. 1, p. 2067, Feb. 2020, doi: 10.1038/s41598-020-59017-z.

[116] A. Hazrati Marangalou, M. Gonzalez, N. Reppucci, and U. Guler, "A Design Review for Biomedical Wireless Power Transfer Systems with a Three-Coil Inductive Link through a Case Study for NICU Applications," *Electronics (Basel)*, vol. 13, no. 19, p. 3947, Oct. 2024, doi: 10.3390/electronics13193947.

[117] A. Ibrahim and M. Kiani, "Inductive power transmission to millimeter-sized biomedical implants using printed spiral coils," in *2016 38th Annual International Conference of the IEEE Engineering in Medicine*

and Biology Society (EMBC), IEEE, Aug. 2016, pp. 4800–4803. doi: 10.1109/EMBC.2016.7591801.

[118] M. Zargham and P. G. Gulak, "Fully Integrated On-Chip Coil in 0.13 µm CMOS for Wireless Power Transfer Through Biological Media," *IEEE Trans Biomed Circuits Syst*, vol. 9, no. 2, pp. 259–271, Apr. 2015, doi: 10.1109/TBCAS.2014.2328318.

[119] E. Andersen, C. Casados, B. D. Truong, and S. Roundy, "Optimal Transmit Coil Design for Wirelessly Powered Biomedical Implants Considering Magnetic Field Safety Constraints," *IEEE Trans Electromagn Compat*, vol. 63, no. 5, pp. 1735–1747, Oct. 2021, doi: 10.1109/TEMC.2021.3104787.

[120] G. Paolini *et al.*, "On-demand beamforming and wide dynamic power range for WPT and EH applications," *Int J Microw Wirel Technol*, vol. 16, no. 6, pp. 903–918, Jul. 2024, doi: 10.1017/S1759078724001065.